Direct Numerical Simulations of Turbulent Autoigniting Hydrogen Jets

A THESIS
SUBMITTED TO THE FACULTY OF THE GRADUATE SCHOOL
OF THE UNIVERSITY OF MINNESOTA
BY

Rajapandiyan Asaithambi

IN PARTIAL FULFILLMENT OF THE REQUIREMENTS
FOR THE DEGREE OF
DOCTOR OF PHILOSOPHY

Krishnan Mahesh, Adviser

November, 2015

Acknowledgements

I am greatly indebted to my adviser Dr. Krishnan Mahesh for the constant support, encouragement, guidance and the patience he offered me through my doctoral program. I would also like to thank him and my teachers, Professors Ellen Longmire, Graham Candler and late Daniel Joseph for having passionately taught me fluid mechanics, something I will cherish for the rest of my life.

I owe my gratitude to my parents, Nirmala & Asaithambi, brother Naveen and my wife Janani for patiently being at my side and making this achievement possible. I thank my extended family for their encouragement through my endeavours.

I would like to thank all my friends and colleagues for making my stay at the University of Minnesota an enjoyable experience. I would also like to thank Sriram, Guru, Aswin, Prahladh and Savio for the memorable discussions.

This work was primarily carried out using hardware and software provided by the University of Minnesota Supercomputing Institute (MSI). Computer time for this work was also granted by (a) the Extreme Science and Engineering Discovery Environment (XSEDE), which is supported by National Science Foundation grant number ACI-1053575, and (b) the Innovative and Novel Computational Impact on Theory and Experiment (INCITE) program, using resources of the Argonne Leadership Computing Facility, which is a DOE Office of Science User Facility supported under Contract DE-AC02-06CH11357.

Dedication

To my family

Abstract

Autoignition is an important phenomenon and a tool in the design of combustion engines. To study autoignition in a canonical form a direct numerical simulation of a turbulent autoigniting hydrogen jet in vitiated coflow conditions at a jet Reynolds number of $10,000$ is performed. A detailed chemical mechanism for hydrogen-air combustion and non-unity Lewis numbers for species transport is used. Realistic inlet conditions are prescribed by obtaining the velocity field from a fully developed turbulent pipe flow simulation.

To perform this simulation a scalable modular density based method for direct numerical simulation (DNS) and large eddy simulation (LES) of compressible reacting flows is developed. The algorithm performs explicit time advancement of transport variables on structured grids. An iterative semi-implicit time advancement is developed for the chemical source terms to alleviate the chemical stiffness of detailed mechanisms. The algorithm is also extended from a Cartesian grid to a cylindrical coordinate system which introduces a singularity at the pole $r = 0$ where terms with a factor $1/r$ can be ill-defined. There are several approaches to eliminate this pole singularity and finite volume methods can bypass this issue by not storing or computing data at the pole. All methods however face a very restrictive time step when using a explicit time advancement scheme in the azimuthal direction (θ) where the cell sizes are of the order $\Delta r \Delta \theta$. We use a conservative finite volume based approach to remove the severe time step restriction imposed by the CFL condition by merging cells in the azimuthal direction. In addition, fluxes in the radial direction are computed with an implicit scheme to allow cells to be clustered along the jet's shear layer. This method is validated and used to perform the large scale turbulent reacting simulation.

The resulting flame structure is found to be similar to a turbulent diffusion flame but stabilized by autoignition at the flame base. Mass-fraction of the hydroperoxyl radical, HO_2, peaks in magnitude upstream of the flame's stabilization

point indicating autoignition. A flame structure similar to a triple–flame, with a lean premixed flame and a rich premixed flame flanking a thick diffusion flame is identified by the flame index. Radicals formed in the shear layer ahead of ignition and oxygen from the coflow do not get fully consumed by the flame and are transported along the edges of the flame brush into the core of the jet. Ignition delays from a well-stirred reactor model and an autoigniting diffusion flame model are able predict the lift-off height of the turbulent flame. The local entrainment rate was observed to increase with axial distance until the flame stabilization point and then decrease downstream. Data from probes placed along the flame reveals a highly turbulent flow field with variable composition at a given location. In general however, it is observed that the turbulent kinetic energy (TKE) is very high in cold fuel rich mixtures and is lowest in hot fuel lean mixtures. Autoignition occurs at the most-reactive hot and lean mixture fractions where the TKE is the lowest.

Contents

List of Tables

List of Figures

Chapter 1

Introduction

1.1 Autoignition

Understanding **autoignition** of fuels is critical to the design of the next generation of internal combustion engines using Homogeneous Charge Compression Ignition (HCCI) as they can achieve higher thermal efficiencies with lower NO_x emissions. Autoignition is also important in the design of scramjet combustors where the fuel mixes with air, ignites, and stable combustion is maintained at supersonic speeds. On the other hand, in Lean-Premixed Prevaporized gas turbines, the challenge is to prevent autoignition of the premixed gases before they reach the flame holders. Autoignition is highly sensitive to the fuel chemistry, temperature, pressure and mixing which is the reason behind the difficulty in studying this phenomenon.

Autoignition can be defined as spontaneous ignition of a fuel-oxidizer mixture which leads to fully burning state or combustion. In a homogeneous mixture autoignition can result from an increase in temperature or pressure and is easily predicted. Autoignition is difficult to predict for inhomogeneous mixtures, however, because it also depends on variation in fuel-oxidizer concentration and

temperature gradients. In addition, autoignition also depends on the dynamics of turbulent mixing. Due to safety and practical considerations, real-world applications operate under non-premixed conditions and need sophisticated tools to understand the mechanism that leads to autoignition.

The mechanism of autoignition under inhomogeneous conditions and laminar flow can be explained using the heat release rate and residence time (inertial time scale). The fuel-oxidizer mixture under certain temperature and turbulence conditions can start reacting and producing heat. If the heat release from combustion at a given location is matched by the heat transport away from this spot, the local temperature remains constant and ignition is prevented. If the heat release exceeds the heat transport for a sufficient period of time, the temperature increases which then leads to increased heat release and this vicious cycle leads to combustion. We call this phenomenon autoignition. If the residence time is cut short before the temperature reaches a high enough value, the autoignition process is cut short and we have no ignition. The ratio of heat release rate to residence time is called the Damköhler number.

The S-Curve in figure 1.1 illustrates the balance between temperature and the Damköhler number for a laminar counterflow diffusion flame with a cold fuel and hot oxidizer. At low temperatures, autoignition does not occur until Da_{ign}. Past this point, autoignition always occurs and reaches the higher temperature branch of the S-curve. A flame at high temperature is stable and stays in the higher temperature branch even at Damköhler numbers lower than Da_{ign}. The flame however is quenched at the lower Damköhler number Da_{quench} and always extinguishes below this point. The dashed line in figure 1.1 represents unstable but steady solutions to the 1D flamelet equations. Above this curve solutions are

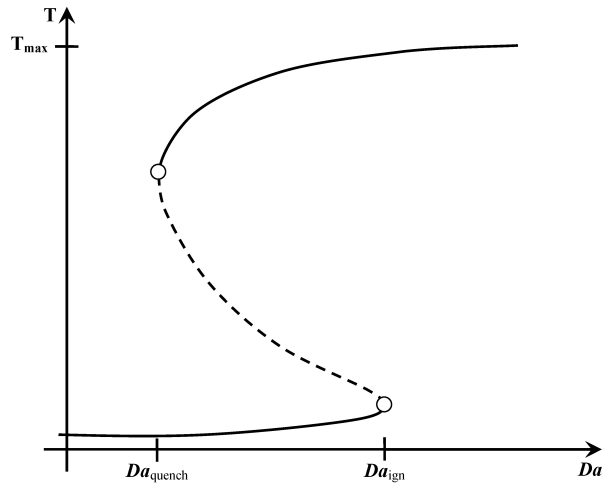

Figure 1.1: S-Curve for a laminar diffusion flame, Illustration by Markides [29]

attracted to the fully burning branch, while below this curve, solutions return to the extinguished branch.

1.1.1 Vitiated coflow burners

To better understand the physics of autoignition in turbulent flows, canonical flames have been designed and studied as a proxy for real-world applications. These laboratory scale flames simplify the geometry of the flame and focus upon the mixing of the fuel-oxidizer streams leading to autoignition spots or an autoignition stabilized lifted flame as opposed to stabilization due to edge flames.

We study a category of flames that has been the focus of extensive experimental and numerical study. The flames designed by Cabra *et al.*[6], Mastorakos *et al.*[32], Dally *et al.*[8], and Oldenhof *et al.*[37] autoignite, where no external heat source is necessary to initiate combustion. The location of autoignition, and hence the lifted flame height, are highly dependent on factors like temperature and turbulent mixing. These experiments were inspired by compression engines, where there is

a need to understand the ignition of fuel jets when injected into a hot oxidizer. These flames pose a challenge to current modelling techniques [30] and a direct numerical simulation of such flames could help better understand the turbulence-chemistry interaction and aid the development and validation of models.

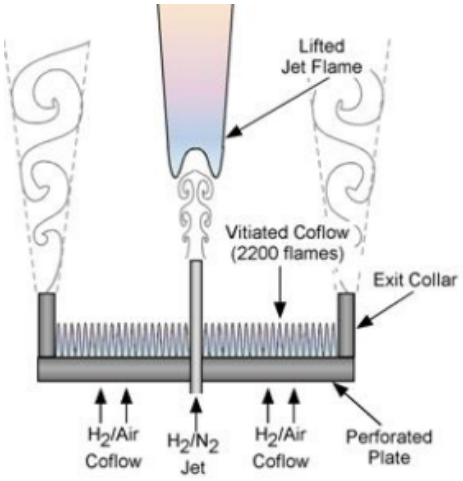

Figure 1.2: Schematic of the vitiated coflow burner by Cabra *et al.*[6]

Cabra *et al.*[6] designed the vitiated coflow burner based on engines that employ exhaust gas recirculation (EGR). In these engines, hot combustion products are circulated back to the combustion chamber where they aid the stabilization of the flame and help reduce NO_x by diluting the mixture. The schematic of the burner is shown in figure 1.2 where a cold fuel jet is injected into a hot coflow, produced by burning a lean hydrogen-air mixture. A lifted flame is obtained and measurements of the different scalars were presented. The authors only speculate about the possibility of autoignition as a stabilization mechanism in this paper. Yoo *et al.*[57] would later show that under similar conditions, a direct numerical simulation of a slot-jet shows that the flame is stabilized primarily by autoignition.

Dally *et al.*[8] and Oldenhof *et al.*[37] also use the exhaust gas recirculation

engines as a reference to design their jet in hot coflow (JHC) burners. These burners however operate under much hotter and leaner conditions with very little oxygen. The terms used to describe these conditions are moderate or intense low-oxygen-dilution (MILD) combustion or flameless combustion. These burners also show autoignition kernels leading to a flame stabilization.

Mastorakos *et al.*[32] designed a different kind of burner which attempts to study the conditions in lean-premixed prevaporized gas turbines and HCCI engines. The burner is operated with a much higher coflow velocity injected with a high level of turbulence. This experiment showed a regime with random autoignition spots that do not lead to stable lifted flames. Lower coflow temperatures or higher coflow velocities produces no ignition while the opposite conditions led to autoignition followed by flashback. A lifted flame regime was also shown later by Markides & Mastorakos [28].

1.1.2 Most-reactive mixture fraction

In autoigniting flames, the mixture fraction that ignites earliest can be different from the stoichiometric mixture fraction. This was shown by Mastorakos *et al.*[31] using direct numerical simulations (DNS). A canonical autoigniting flame has cold fuel mix with hot oxidizer and this temperature stratification causes the hot lean mixtures to ignite quicker than the stoichiometric mixture. Mastorakos calls this the most-reactive mixture fraction ξ_{MR}, "the value of ξ where the reaction rate becomes a maximum" [30]. Further, Mastorakos notes that the simulations showed the most-reactive mixture fraction to be insensitive to the turbulence time scale, length scale and mixing layer thickness.

Mastorakos [30] suggests *a priori* estimation of ξ_{MR} from homogeneous reactor

simulations of mixture fractions corresponding to initial conditions obtained from the mixing line of cold fuel and hot oxidizer. A laminar diffusion flame may also be simulated including the effects of differential diffusion and strain rate. Both simulations provide the ignition time as a function of mixture fraction which can be used as a guide to predicting autoignition time delays in a jet flame.

The effect of scalar dissipation, $\chi = 2D(\partial\xi/\partial x_j)^2$, on autoignition is another factor emphasized by Mastorakos [30]. Autoignition is understood to occur faster in regions of low scalar dissipation, and very high values could preclude the formation of autoignition kernels completely. Combining the two factors that influence autoignition, Mastorakos suggests that the history of the conditional variable $\chi|\xi_{MR}$ plays an important part in determining the evolution of autoignition kernels and those that form are likely to have experienced low $\chi|\xi_{MR}$.

1.2 Numerical simulations of autoigniting flames

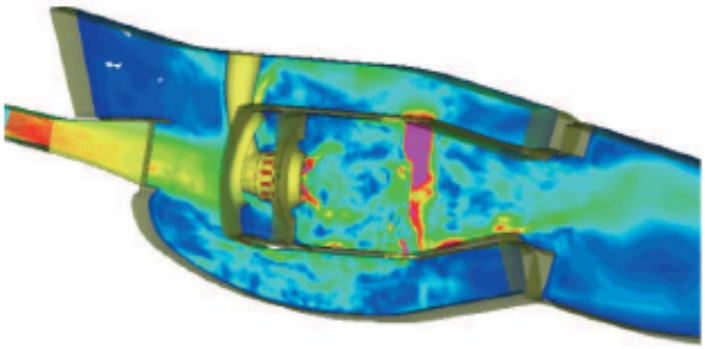

Figure 1.3: Velocity contours from an LES of a Pratt and Whitney combustor by Mahesh *et al.*[26]

The timing of auto-ignition is critical to the operation of HCCI or Scramjet engines and therefore the transient nature of the autoignition needs to be captured in a numerical simulation. The tools to study these phenomena are typically Reynolds averaged Navier Stokes (RANS) based models which can be quite inaccurate [53] due to the lack of representation of finite rate chemical reactions and their unsteady coupling with the turbulent flow field. Large eddy simulations (LES) using unsteady flamelet progress-variable models [42] have been successfully applied to complex combustor geometries [26] as shown in figure 1.3. However, autoignition involves a fundamentally different pathway to flame creation and these models are inadequate for autoignition stabilized flames. Modeling this phenomenon needs to take into consideration of the unsteady nature of autoignition and the influence of turbulence on ignition [30].

Pioneering direct numerical simulations (DNS) of autoigniting turbulent slot-jet flames [18, 57] have been performed and the stabilization mechanisms in such flames shown to be assisted by autoignition. High fidelity DNS simulations are therefore highly valuable to verify these results and provide unique physical insight into the fundamental physics, which can be be used to develop improved models.

1.3 A numerical algorithm for DNS/LES of reacting flows

High fidelity DNS and LES of practical flows with combustion require highly parallel and scalable algorithms. Compared to a non-reacting simulation, the high computational cost of these turbulent reacting flow simulations comes from (i) the additional number of species equations that need to be solved, (ii) Arrhenius

reaction rate terms from detailed chemical mechanisms and (iii) the wide range of time and length scales, which increases the temporal and spatial resolution requirements. This results in a larger grid and causes stiffness, imposed by chemical reactions, which also results in thin flame fronts. A stiff solver can help address (ii) and (iii). The number of species transport equations is harder to address numerically. Detailed mechanisms are often reduced to smaller set of species and reactions through various assumptions resulting in smaller reduced mechanisms.

Doom *et al.*[10] linearized the species source term and implemented a semi-implicit time integration scheme that allowed the stiffness from acoustic and chemical time scales to be manageable. The algorithm was then applied to auto-ignition of hydrogen vortex rings in Doom & Mahesh [11]. The solver was an implicit projection based method and implicit algorithms are harder to scale on parallel machines as well as explicit algorithms. This is due to the additional cost of implicit techniques having to converge the solution spatially, which increases the communication cost substantially. An unstructured explicit solver that is derived from Park & Mahesh [39] has been used in very large complex geometries, includes a robust modified least squares flux reconstruction, a shock-capturing scheme and subgrid-scale modelling.

A hybrid density based approach where we retain the explicit solver for advection and diffusion and integrate the chemical source term using the semi-implicit method is therefore appropriate for a scalable reacting flow solver operating under compressible conditions. As the source terms do not rely on spatial gradients, the implicit iterations do not require communication which leads to a highly scalable solver.

1.4 Contributions

The key contributions of this dissertation are:

- An MPI/Fortran 90 based scalable parallel compressible structured solver was built to perform direct numerical simulation on high performance clusters.
- A DNS/LES algorithm for compressible reacting jets was developed. The algorithm is explicit in time for transport terms and implicit for the stiff chemical source terms.
- The chemical source terms implemented as a corrector step and the iterations are decoupled from neighboring cells thus enhancing scalability of the code and reducing total computational cost.
- Automated parsing of Chemkin reaction mechanisms and thermodynamic input files is implemented allowing a black-box like ability to use any fuel and oxidizer for a simulation. Automated linearization of chemical source terms is also done in conjunction with the mechanism parsing which enables the use of large time steps for stiff mechanisms.
- A cell-merging algorithm to eliminate the strict time-step restriction in the azimuthal direction was developed and validated for cylindrical grids. Implicit radial terms are coupled with cell-merging algorithm.
- Simulation of laminar jet flames with multiple fuels, hydrogen, methane and ethylene were performed successfully and differences in flame structure noted.

- Simulation of a round turbulent lifted hydrogen flame at $Re = 10,000$ was performed under vitiated coflow conditions. A fully developed pipe velocity field was interpolated onto the fuel jet's inlet plane to provide realistic boundary condition.

- The hydroperoxyl radical, HO_2, was detected upstream of the flame base and the scalar dissipation was found to be low supporting the idea of an autoignition based stabilization for the lifted flame. Estimation of lifted height from homogeneous reactor model and autoigniting diffusion flame model confirm the stabilization mechanism as autoignition.

- Both aligned and opposed mode of flame indices were observed post-ignition with a triple-flame like structure but stabilized by autoignition instead of a turbulent edge flame. Oxygen from the vitiated coflow and HO_2 radical were measured in the fuel jet's core downstream of the flame base which aid in sustaining a rich premixed flame on the inner edge of the flame.

- The entrainment field of the autoigniting flame was found to be similar to that of a diffusion flame, with increasing local entrainment rates up to the ignition point and decreasing thereafter.

1.5 Dissertation organization

This dissertation is organized as follows: In chapter 2, the governing equations are listed and a density based explicit method to solve compressible reacting flows is described. Chapter 3 describes the algorithm that extends the method to cylindrical grids and the cell merging method to address time-step limitations associated

with thin cells near the pole. Validation of the method for a well-stirred reactor for different fuel chemistries is presented followed by two-dimensional jet simulations to obtain the grid and time step requirements for autoigniting jet flames in multiple fuels. Chapter 5 presents results from a round turbulent autoigniting hydrogen jet flame simulation. The physics behind flame stabilization and lifted height estimation for the turbulent flame is discussed. Finally, a conclusion is drawn in chapter 6.

In appendix A, a novel tabulation based combustion model is described and applicability to simple one-dimensional problems is shown.

Chapter 2

Numerical Algorithm

2.1 Governing Equations

The governing equations employed are the compressible reacting Navier-Stokes equations. In Cartesian coordinates, the equations in dimensional form for density (ρ^d), species mass-fractions (Y_k), momentum ($\rho^d u_i^d$) and total chemical energy (E_t^d) are written as follows:

$$\frac{\partial \rho^d}{\partial t^d} + \frac{\partial \rho u_j^d}{\partial x_j^d} = 0 \tag{2.1}$$

$$\frac{\partial \rho^d Y_k}{\partial t^d} + \frac{\partial \rho^d Y_k u_j^d}{\partial x_j^d} = \frac{\partial}{\partial x_j^d}\left(\rho^d D_k^d \frac{\partial Y_k}{\partial x_j^d}\right) + \dot{\omega}_k^d \tag{2.2}$$

$$\frac{\partial \rho^d u_i^d}{\partial t^d} + \frac{\partial \rho^d u_i^d u_j^d}{\partial x_j^d} = -\frac{\partial p^d}{\partial x_j^d} + \frac{\partial \tau_{ij}^d}{\partial x_j^d} \tag{2.3}$$

$$\frac{\partial \rho^d E_t^d}{\partial t^d} + \frac{\partial}{\partial x_j^d}\left(\rho^d E_t^d + p^d\right) u_j^d = \frac{\partial \tau_{ij}^d u_i^d}{\partial x_j^d} + \frac{\partial}{\partial x_j^d}\left(k^d \frac{\partial T^d}{\partial x_j^d}\right) \tag{2.4}$$

where the viscous stress tensor τ_{ij}^d is:

$$\tau_{ij}^d = \mu^d \left(\frac{\partial u_i^d}{\partial x_j^d} + \frac{\partial u_j^d}{\partial x_i^d} - \frac{2}{3} \frac{\partial u_k^d}{\partial x_k^d} \delta_{ij} \right) \tag{2.5}$$

The total chemical energy E_t^d can be written in terms on enthalpy h_t^d which is itself the sum of sensible enthalpy and chemical enthalpy. The sensible enthalpy is derived by integrating the variable specific heat capacity of the mixture, c_p^d, over temperature, T^d. The heat of formation of species $\triangle {h_{f,k}^o}^d$ determines the chemical enthalpy. The energy equation therefore does not have a separate source term for chemical heat release since the heat of formation is included in the total chemical energy.

$$E_t^d = e_t^d + \frac{u_i^d u_i^d}{2} = h_t^d - p^d/\rho^d + \frac{u_i^d u_i^d}{2} \tag{2.6}$$

$$h_t^d = \int_{T_o^d}^{T^d} c_p^d(Y_k, T'^d) dT'^d + \sum_{k=1}^{n} \triangle {h_{f,k}^o}^d Y_k \tag{2.7}$$

The superscript 'd' denotes dimensional quantities. We can non-dimensionalize these equations with reference quantities denoted with the subscript 'r'. Non-dimensional time, length and velocity are obtained from a specified length scale L_r and a velocity scale u_r. The time scale used is the inertial time scale (L_r/u_r). Pressure is non-dimensionalized using the compressible scaling $p = p^d/\rho_r u_r^2$. A reference mixture defined by species mass-fractions at a given temperature T_r and pressure p_r can be used to determine non-dimensional density ρ, temperature T, gas constant R, molecular weight W, specific heat capacity c_p, enthalpy h and mixture viscosity μ. Reference molecular viscosity is currently defined by setting

the Reynolds number for the simulation.

$$t = \frac{t^d}{L_r/u_r}, x = \frac{x^d}{L_r}, \rho = \frac{\rho^d}{\rho_r}, u_i = \frac{u_i^d}{u_r}, p = \frac{p^d}{\rho_r u_r^2}, T = \frac{T^d}{T_r} \tag{2.8}$$

$$R = \frac{R^d}{R_r}, W = \frac{W^d}{W_r}, R_r = \frac{R_{univ}}{W_r}, c_p = \frac{c_p^d}{R_r}, h = \frac{h^d}{R_r T_r}, \mu = \frac{\mu^d}{\mu_r} \tag{2.9}$$

The reference quantities that need to be chosen for a given simulation are a length scale, a velocity scale and the thermodynamic properties: pressure, temperature, molecular weight and viscosity based on a reference mixture. From the specified reference quantities, we derive the non-dimensional constants listed below: Mach number M_r, Reynolds number Re, Schmidt number Sc_k and the Prandtl number Pr. In the simulation performed, the Reynolds number and Mach number are chosen based on the experimental regimes we intend to study. The Prandtly is assumed to be a constant of value 0.7. The Schmidt numbers are either set to 1 or set to constant values, different for each species, based on their Lewis numbers. The Lewis number is defined as $Le = Sc/Pr$ and is obtained from external published data.

$$M_r = \frac{u_r}{c_r}, Re = \frac{\rho_r u_r L_r}{\mu_r}, Sc_k = \frac{\mu^d}{\rho^d D_k^d}, Pr = \frac{\mu^d c_p^d}{k^d} \tag{2.10}$$

Here, c_r is the speed of sound of the reference mixture and is obtained from the relation $c_r^2 = \gamma_r R_r T_r$, where γ_r is the heat capacity ratio. The quantities, D_k^d and k^d represent the molecular diffusivity and thermal conductivity of the mixture. Note that the diffusivities are that of each species with respect to the mixture and is a vector of length k corresponding to the number of species.

The governing equations can now be written down in the non-dimensional form as follows:

$$\frac{\partial \rho}{\partial t} + \frac{\partial \rho u_j}{\partial x_j} = 0 \tag{2.11}$$

$$\frac{\partial \rho Y_k}{\partial t} + \frac{\partial \rho Y_k u_j}{\partial x_j} = \frac{1}{ReSc_k}\frac{\partial}{\partial x_j}\left(\mu \frac{\partial Y_k}{\partial x_j}\right) + \dot{\omega}_k \tag{2.12}$$

$$\frac{\partial \rho u_i}{\partial t} + \frac{\partial \rho u_i u_j}{\partial x_j} = -\frac{\partial p}{\partial x_j} + \frac{1}{Re}\frac{\partial \tau_{ij}}{\partial x_j} \tag{2.13}$$

$$\frac{\partial \rho E_t}{\partial t} + \frac{\partial}{\partial x_j}\left(\rho E_t + p\right) u_j = \frac{1}{Re}\frac{\partial \tau_{ij} u_i}{\partial x_j} + \frac{1}{\gamma_r M_r^2 RePr}\frac{\partial}{\partial x_j}\left(\mu c_p \frac{\partial T}{\partial x_j}\right) \tag{2.14}$$

The equation of state is that of a thermally perfect ideal gas, $p_r = \rho_r R_r T_r$, which in non-dimensional form is written as:

$$\rho T = \gamma_r M_r^2 p W \tag{2.15}$$

2.1.1 Governing Equations for Non-Reacting Medium

The governing equations can be reduced to the following for a non-reacting compressible medium. In the absence of species, we have density, momentum and total energy equations which still retain the exact same form as above. Note that the total chemical energy however has been replaced with total energy.

$$\frac{\partial \rho}{\partial t} + \frac{\partial \rho u_j}{\partial x_j} = 0 \tag{2.16}$$

$$\frac{\partial \rho u_i}{\partial t} + \frac{\partial \rho u_i u_j}{\partial x_j} = -\frac{\partial p}{\partial x_j} + \frac{1}{Re}\frac{\partial \tau_{ij}}{\partial x_j} \tag{2.17}$$

$$\frac{\partial \rho E_t}{\partial t} + \frac{\partial}{\partial x_j}\left(\rho E_t + p\right) u_j = \frac{1}{Re}\frac{\partial \tau_{ij} u_i}{\partial x_j} + \frac{1}{\gamma_r M_r^2 Re Pr}\frac{\partial}{\partial x_j}\left(\mu c_p \frac{\partial T}{\partial x_j}\right) \tag{2.18}$$

The total energy E_t can be written in terms on sensible energy e_t and kinetic energy. The sensible energy can be approximated to $c_v T$ for fluid flow problems with no temperature gradients. Without reactions, the formation enthalpies need not be accounted for and hence the change from total chemical energy to total energy.

$$E_t = e_t + \frac{u_i u_i}{2} = c_v T + \frac{u_i u_i}{2} \tag{2.19}$$

The non-dimensional equation of state is still $\rho T = \gamma_r M_r^2 p W$ where the pressure is non-dimensionalized using the compressible scaling $p = p^d/\rho_r u_r^2$. The medium is now assumed to be a thermally and calorically perfect ideal gas with constant heat capacity.

2.2 Numerical Method

The governing equations are discretized using a finite volume algorithm second order accurate in space and time. The variables are colocated and stored at the cell centers. Note that we solve in Cartesian coordinates and therefore compute the Cartesian velocies u, v and w.

The density, mass-fractions, momentum and total chemical energy equations

are explicitly solved in the **predictor** step using the following finite volume discretization:

$$\frac{\partial \rho}{\partial t} = -\frac{1}{V_f} \sum_{faces} \rho_f v_n A_f \tag{2.20}$$

$$\frac{\partial \rho Y_k}{\partial t} = -\frac{1}{V_f} \sum_{faces} \left[\rho_f Y_{k,f} v_n + J_{k,f} n_k \right] A_f \tag{2.21}$$

$$\frac{\partial \rho u_i}{\partial t} = -\frac{1}{V_f} \sum_{faces} \left[\rho u_{i,f} v_n + p_f n_i - \frac{1}{Re} \tau_{ik,f} n_k \right] A_f \tag{2.22}$$

$$\frac{\partial \rho E_t}{\partial t} = -\frac{1}{V_f} \sum_{faces} \left[\left(\rho E_t + p \right) v_n - \frac{1}{Re} \tau_{ik,f} u_{i,f} n_k - Q_{k,f} n_k \right] A_f \tag{2.23}$$

Symmetric average flux reconstruction of cell centered variables is used to obtain the values at faces in the structured solver, as described by Park & Mahesh [39]. The predictor step equations, consisting of advection and diffusion terms on the right hand side, are advanced in time using the fully explicit second order Adams-Bashforth time discretization written as:

$$q^{n+1} = q^n + \frac{\Delta t}{2} \left[3 * rhs^n(q) - rhs^{n-1}(q) \right] \tag{2.24}$$

The time integration is performed differently for reacting and non-reacting equations due to way the energy equation is posed. For a reacting system, we obtain the density ρ, mass fractions $\hat{Y}_k$, momentum ρu_i and total chemical energy ρE_t for all the cells at time $(t+1)$. The species equation 2.21 is solved without the source term $\dot{\omega}$ and thus the first step gives us $\rho \hat{Y}_k$. This predicted species density has to be **corrected** to include the effect of chemical reactions from the

source term. The stiff chemical source terms are linearized and iteratively solved. The source terms employ a second-order semi-implicit discretization as described in Doom & Mahesh [10]. Since the source term only affects the species equations, mass, momentum and energy are not affected and this allows us to decouple the source term. The source term is a function of species concentrations and temperature only and so is the chemical energy e_t. Since the quantities ρ^{t+1}, ρu_i^{t+1} and E_t^{t+1} are already known, e_t^{t+1} can be derived. The change in species concentrations due to the chemical source terms therefore is an ordinary differential equation with a constraint e_t^{t+1} that the mass fractions Y_k^{t+1} and T^{t+1} have to obey. The correction for source terms is solved as follows:

$$\frac{(\rho Y_k)^{t+1,p} - (\rho \hat{Y_k})^{t+1})}{\Delta t} = \dot{\omega}_k((\rho Y_k)^t, (\rho Y_k)^{t+1,p}, (T)^t, (T)^{t+1,p}) \tag{2.25}$$

$$T^{t+1,p} = f^{-1}({e_t}^{t+1}, {Y_k}^{t+1,p}) \tag{2.26}$$

This step yields the final species mass fractions and temperature at the new time step. While the predicted species densities add up to the total density predicted by equation 2.20, the corrected species densities will not satisfy this identity due to linearization errors. To ensure that mass is conserved, the corrected species densities are normalized to ensure $\sum_k Y_k = 1$ is satisfied. The normalization step can be written as:

$$Y_k^{t+1} = \frac{Y_k^{t+1,p}}{\sum_k Y_k^{t+1,p}} \tag{2.27}$$

The enthalpy necessary to calculate e_t is obtained directly from thermodynamic property tables as a function of temperature and species concentrations.

Since e_t and h_t are both purely functions of temperature and species composition and we are trying to estimate the temperature from eq. 2.26, this step involves a multivariate root finding method for which we use Halley's method, which has a faster rate of convergence than the Newton-Raphson method. In the solver, the maximum number of iterations is set to 50 and a well resolved simulation typically requires less than 5 iterations to converge to a solution within a normalized tolerance of 10^{-8}.

For the non-reacting system, the species equation and the associated semi-implicit method need not be solved. In addition, the total energy that is being solved for directly gives us the temperature since the specific heat capacity is assumed constant and the root finding method is unnecessary. The root finding step would still be needed if the heat capacity was a function of temperature.

2.3 Boundary conditions

While Neumann boundary conditions with a far-field pressure are sufficient for most outflow boundaries, with reacting flows it is important to specify boundary conditions that can allow flames to exit the domain without numerical instabilities or pressure disturbances. Simulations performed with Neumann boundary conditions produced strong pressure waves and reversed flow conditions and a better boundary condition was necessary. Absorbing boundary conditions, also known as sponges, were useful in suppressing reversed flow at the outflow but did not eliminate large wavelength pressure fluctuations. A more robust boundary condition was necessary to stabilize the pressure field in the domain and ensure

stable outflow. Another challenge with sponges are the need to prescribe a reference background condition which can be challenging in a transient turbulent flame simulation. The thickness of the absorbing layer also determines the wavelength of the pressure fluctuations that get absorbed and long wavelength oscillations on the order of the domain size will not be easily dissipated. Non-reflecting boundary conditions are better suited for this problem and help minimize reflections from the boundaries. Note that non-reflecting boundary conditions are not perfect and can still reflect waves that are oblique to the boundary.

The Navier Stokes Characteristic Boundary Conditions (NSCBC) [45] along with the modifications suggested by Sutherland & Kennedy [50] were implemented in this solver to ensure proper non-reflecting outflow for a reacting jet. These boundary conditions also have the advantage of smaller computational domain without the need for sponge layers.

2.4 Homogeneous Reactor

The homogeneous or well-stirred reactor has no spatial variations and hence this is a zero-dimensional problem with evolution in time only. The governing equations reduce to a set of ordinary differential equations and this problem serves as a validation for the chemical source terms. The results are compared with Chemkin for two different fuels, hydrogen and methane.

A hydrogen-air mixture at $1500K$ and a methane-air mixture at $2500K$, both at stoichiometric ratios and atmospheric pressure, were solved. In figures 2.1(a) and 2.1(b) the results obtained from the simulation are shown as straight lines which are compared with Chemkin , shown as dots. We are able to get excellent

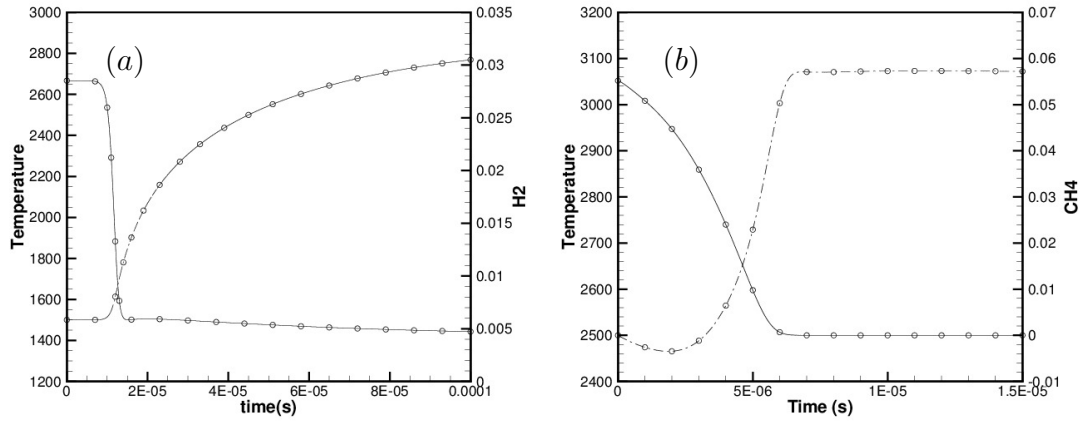

Figure 2.1: (a) $H_2 - Air$ Mueller Mechanism, and (b) $CH_4 - Air$ GRI-Mech 3.0 Mechanism

agreement with both fuels, hydrogen, which uses a 9 species, 19 reaction Mueller *et al.*[35] mechanism and methane, which uses the full GRI-Mech 3.0 [49] mechanism with 53 species and 325 reactions. This demonstrates the black-box like ability of the chemistry module to solve a wide range of chemical mechanisms. In the jet flame simulations described later we use this flexibility to study three different fuels in the same configuration.

2.5 One-dimensional unsteady unstrained diffusion flame

An unsteady unstrained one-dimensional diffusion flame with cold fuel (H_2/N_2 at $T = 1$) and hot oxidizer (Air at $T = 4$) is simulated in this section. The hot oxidizer allows autoignition of fuel at the interface, no 'numerical spark' is needed to start the combustion. Autoignition quickly stabilizes into a diffusion flame and

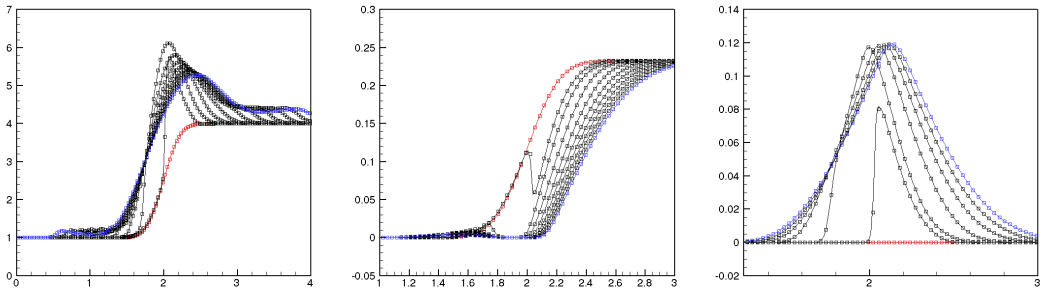

(a) Temperature (b) Y_{O_2} (c) Y_{H_2O}

Figure 2.2: Comparison of $1D$ unstrained diffusion flame results from the current structured solver (□) and the unstructured (–) solver, MPCUGLES [27]

slowly evolves over time.

Fuel	T_{fuel}	T_{air}	Y_{fuel}	Y_{O_2}	Re
H_2/N_2	1	4	0.029	0.233	1000

Table 2.1: Initial conditions for the unsteady one-dimensional flame

Initial conditions for the simulation are specified in table 2.1 with temperature in non-dimensional units. The reference temperature is $298K$. In figure 2.2 the red lines are the initial profiles and blue lines the final profile after $0.1s$. The mass fractions are 0.029 for hydrogen on the cold fuel end (left half) and 0.233 for oxygen of the hot oxidizer end (right half) and the rest filled up with nitrogen. The mass fraction of H_2O peaks at 0.12 for the diffusion flame at $t = 0.1s$. After the autoignition phase, the production of H_2O is expected to be limited by diffusion of fuel and oxidizer into the flame, thus slowly losing heat while expanding in thickness. This problem demonstrates the ability of the code to handle the sudden and large heat release due to autoignition and do so consistently across two solvers

as shown the comparison in figure 2.2. This problem verifies the current solver's implementation against a validated solver, MPCUGLES by [27].

2.6 Scaling on High Performance Computers

Performing direct numerical simulations for experimental conditions like that of Cabra *et al.*[6] requires enormous computational resources due to the scale of the problem. The spacing of grid elements needed for a DNS needs to be fine enough to capture flame surfaces in the jet's shear layer. We estimate that at a Reynolds number of $23,600$, a polar grid with 3.2 billion elements would be necessary to simulate a domain of size $30D \times 2\pi \times 10D$. The grid would have 6144 points in the streamwise direction, 1024 in the azimuthal direction and 512 in the radial direction. With an estimated time step of 5×10^{-4} simulated for 10 flow-through times, based on a speeds obtained on Mira at ALCF, this simulation would require roughly 100 million processor hours of compute time. This would correspond to about 768 hours or 32 days on $131,072$ processors.

Massively parallel simulations such as this require the solver to be highly scalable and the algorithm was designed with scalability in mind. The predictor-corrector algorithm for separating the implicit source term from the explicit transport terms was largely responsible for the excellent scalability of this solver. This section presents the results from the scaling tests on various supercomputers.

2.6.1 Parallel performance

Scaling studies have been performed on the following supercomputers: Cetus and Mira (Argonne Leadership Computational Facility, ANL), Kraken (National Institute for Computational Sciences, ORNL), and Itasca (Minnesota Supercomputing Institute, Univ. of Minnesota). The results indicate good scaling on these various architectures.

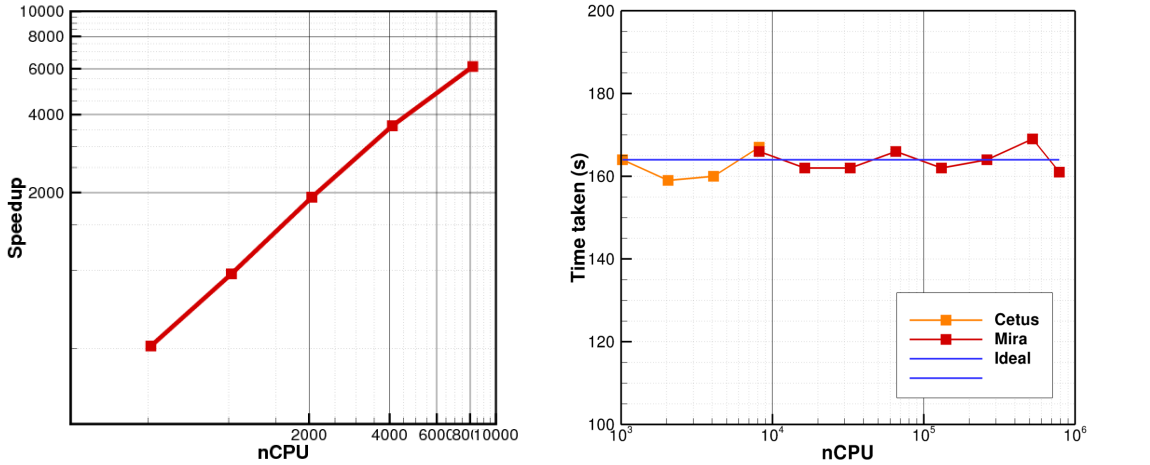

Figure 2.3: (a) Strong scaling study on Cetus on a grid with $103M$ elements. (b) Weak scaling study on Cetus and Mira with $100k$ elements per processor. Up to $786,432$ processors have been used.

On the IBM BG/Q architecture of Cetus and Mira, we notice very good strong scaling and almost perfect weak scaling as shown in figure 2.3. The strong scaling results shown in figure 2.3(a) shows good scaling up to 4000 processors which suggests that more than $25k$ elements per processor is desirable for production runs on Mira with the limit being the total memory available. While using 8000 processors still results in faster execution, the efficiency has dropped to 50% which

is not ideal for optimal use of resources. The weak scaling results on the other hand, shown in figure 2.3(b), indicates that the solver can scale up to a million processors while using $100k$ elements per processor. Additionally, using hardware threads (modes c32 and c64) sped up the results by a factor of 1.6 for two tasks/cpu and 2.1 for four tasks/processor over a single task per processor.

Kraken and Itasca represent Intel's x86 architecture. Figure 2.4 shows the strong and weak scaling results on Kraken and Itasca. On Kraken, a strong scaling study with three workloads were performed: a two-dimensional grid with $458k$ grid elements and two three-dimensional grids with $205M$ and $1.64B$ elements. On Itasca, a strong scaling study was performed with a three-dimensional grid with $150M$ elements. The weak scaling study was performed using a three-dimensional grid at three different workloads: $67k$, $134k$ and $268k$ elements per processor with the largest grid containing 13.2 billion elements and run on $49,152$ processors. The study suggests $150k$ elements per processor would scale well up to a hundred thousand processors.

Memory and Disk requirements

The solver typically requires 5 kbytes per control volume with the hydrogen-air chemistry mechanism, with 9 species and 19 reactions. Complex mechanisms with larger number of species will increase the memory footprint of the code. This limits us to roughly 0.2 million elements per Gbyte of memory or less with LES models enabled. As for data requirements, each snapshot roughly occupies 500 bytes per control volume. A $3.2B$ mesh would generate a $2TB$ data file for a single snapshot. Typical usage of multiple checkpoints, statistical data collection would require the usage of $50TB$ disk-space for this problem.

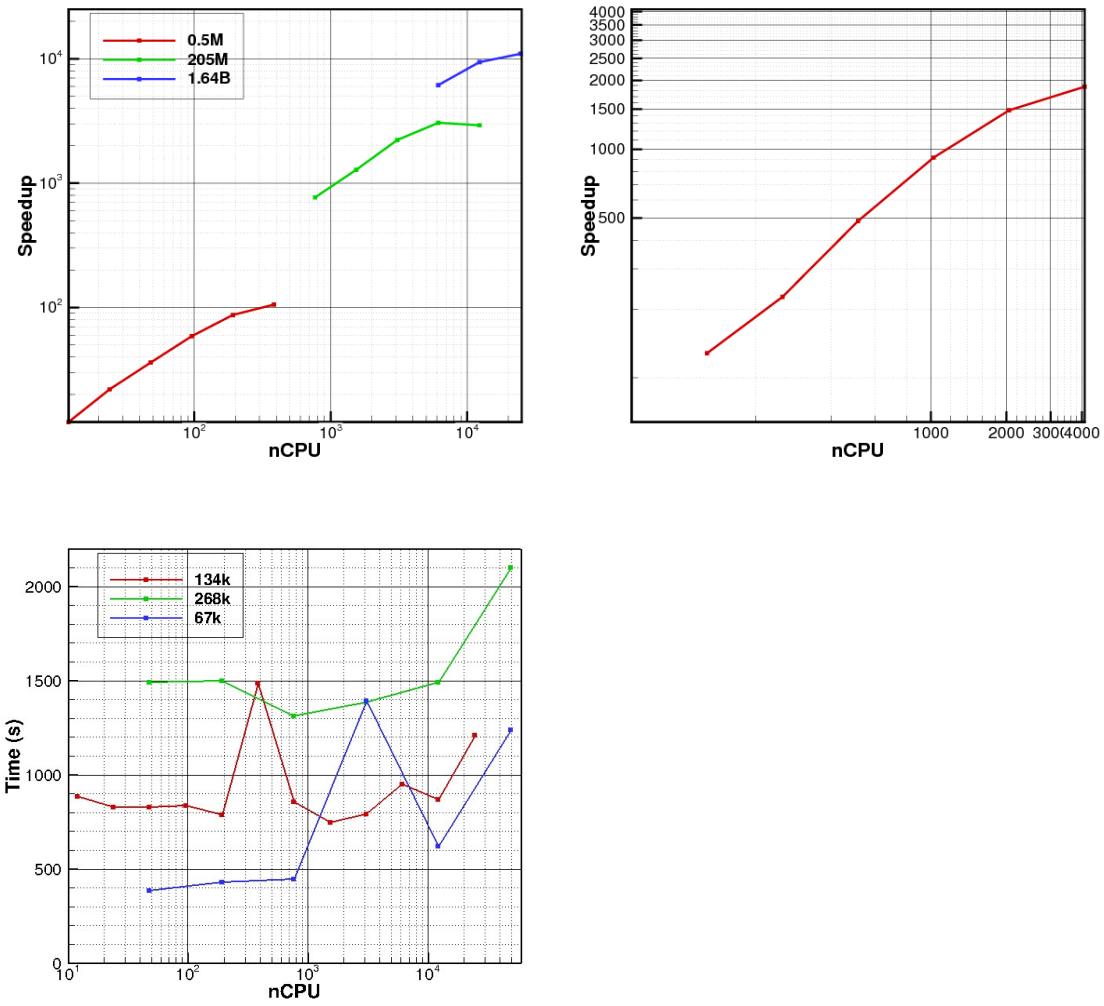

Figure 2.4: (a) Strong scaling study on Kraken with $458k$, $205M$ and $1.64B$ grid elements. (b) Strong scaling study on Itasca with a $150M$ element grid. (c) Weak scaling study on Kraken with $67k$, $134k$ and $268k$ elements per processor. Up to 49152 processors have been used.

Chapter 3

Cell Merging in Polar Coordinates

3.1 Introduction

Complex real world problems can be broken down into simpler canonical problems that are easier to define and understand. A number of these canonical problems are naturally defined in polar or cylidrical coordinates such as flows in pipes, round jets, vortices, axisymmetric wakes and shear layers. The applications range from transport of fluids, mixing, combustion, aeroacoustics, external aerodynamics of axisymmetric objects and their boundary layers. Jets form a large subset of these canonical problems owing to their ubiquity in industrial applications. The need to study jets in the real world ranging from cooling microjets to jet engines necessitates us to develop algorithms that can handle round turbulent jets. More specifically, our interests lie in studying autoigniting fuel jets in vitiated coflow conditions [6]. Controlling autoignition can lead to the design of more efficient internal combustion engines based on homogeneous charge compression ignition

(HCCI).

Cartesian meshes can be used to study round jets [2, 5], but they can be inefficient when it comes to frugal usage of grid cells. In general, structured meshes have an inherent advantage over unstructured meshes in computational cost due to the regular data structure. Among structured meshes, uniformly spaced Cartesian meshes are the simplest to work with as they do not require storage of grid metric terms. Some of the largest direct numerical simulations have been performed with Cartesian meshes [57, 56]. For round jets however, most of the grid cells are needed in the vicinity of the jet's shear layer and this is better served by a cylindrical mesh. The same effect can also be achieved by a spherical mesh, as shown by Boersma et al. [4], who used it for a jet simulation with the pole placed along the streamwise direction. Note that both a cylindrical and spherical mesh are three dimensional extensions to a polar mesh and the issues discussed here are equally applicable to both meshes.

A polar mesh allows the cells in the radial direction to be clustered along the jet's shear layer. Creating a Cartesian mesh that equally resolves the shear layer incurs the cost of adding extra resolution along both the x and y axes creating a plus shaped region of fine grid spacing. The Cartesian mesh is estimated to require about 10 times more grid cells to simulate a jet at a Reynolds number of $Re = 10,000$. A cylindrical mesh with a domain size of 10 jet diameters (D) would need about 384 cells in the radial direction to cluster enough cells close to the jet and have a radial spacing of $0.001D$ at the shear layer $r = 0.5D$. To resolve this shear layer with a Cartesian mesh, 1000 cells each would be necessary in both x and y axes just to capture the region along the jet's shear layer. With non-uniform meshing away from the jet, atleast 1200 cells would be necessary in each

axis to mesh the entire domain. Assuming 384 cells in the azimuthal direction and 512 cells in the streamwise direction which is common to both meshes, we find that the Cartesian mesh has 737 million cells compared to 75 million cells in the cylindrical mesh.

This ratio shoots up to about 100 times more cells for a jet Reynolds number of $Re = 24,000$. The higher the Reynolds number of the jet, the easier it is to make a case for a cylindrical mesh over a Cartesian mesh. A cylindrical mesh however may not be suitable when symmetry is broken as in the case of a jet with cross-flow or multiple jets. A cylindrical mesh, when appropriate for the problem to be simulated, still has two numerical difficulties to overcome: (a) a grid singularity at the pole $r = 0$ and (b) the severe time-step limitation from the small azimuthal edges of size $O(\Delta r \Delta\theta)$ as we get closer to the pole. These problems are addressed in various ways depending on the method used to solve the fluid equations.

Finite difference methods and pseudo-spectral methods need to explicitly address the grid singularity at $r = 0$ when the Navier-Stokes equations are solved in polar coordinates. Methods used to alleviate this problem range from directly treating singular terms to shifting the grid cells away from the center altogether. One set of methods directly address the singularity at $r = 0$. Griffin et al. [16] apply L'Hospital's rule to all the terms with a $1/r$ component. One-sided differencing was applied at the center and second-order accuracy was necessary to prevent spurious pressure oscillations. Freund et al. [14] solve for the center point in Cartesian coordinates to avoid the singularity. This procedure transforms variables back and forth from polar coordinates to Cartesian coordinates at the centerline. Constantinescu and Lele [7] derive a new set of equations at the

pole using series expansions for the variables and find that the method produces better results than using Cartesian equations at the pole.

Another set of methods avoid the singularity by not placing a grid point at $r = 0$. Mohseni and Colonius [34] note that most methods use pole conditions at the centerline which acts as a boundary condition and reduces the accuracy of the solution. In addition, points are clustered near the boundary, in this case at $r = 0$ and $r = R$ whereas the jet needs clustering at the shear layer at $r = D/2$, where D is the jet diameter. Hence, Mohseni and Colonius transform the grid from $(0, R)$ to $(-R, R)$ and avoid placing points at $r = 0$ which are instead placed at $r = -\Delta r/2$ and $r = \Delta r/2$. To remove the time-step limitation in the azimuthal direction the solution was filtered with a sharp spectral filter with a cutoff wavelength which is a function of the radial location. This grid transformation also has the benefit of applying higher order schemes to evaluate terms close to the centerline [7, 20].

Finite volume methods on the other hand avoid most of the complexities of the pole singularity problem. At the pole, grid metrics such as face normals can be undefined and multivalued variables have to be correctly addressed. These are however, easily solved by setting fluxes from the degenerate faces at the centerline to zero. The issue of restrictive time-steps, however, still needs to be addressed. Eggels et al. [13] treat all azimuthal derivatives implicitly to avoid the explicit time-step limit. All radial and axial terms, however, were explicitly itegrated in time. Akselvoll and Moin [1] developed a method in which the cyclindrical domain was split into two regions. Near the centerline, the azimuthal terms were treated implicitly and for cells close to the radial boundary, the radial terms were implicit. This allowed clustering in the radial direction along the wall without its associated time-step limitations. At the interface between the two regions, conditions were

derived to maintain overall accuracy and avoided coupling the implicit terms in two axes.

We propose a unique finite volume strategy to address the time-step limitation in the azimuthal direction which is easily coupled to an implicit method in the radial direction. We note that a jet or pipe flow does not require the excessive azimuthal resolution at the centerline and since this is the source of the time-step restriction, we can solve this problem by merging these thin cells into larger cells in the azimuthal direction. This procedure is conservative, computationally inexpensive and can be easily implemented in an existing finite volume code. This chapter describes the formulation of the cell-merging procedure and shows the validation of the algorithm for a periodic laminar pipe, a Lamb-Oseen vortex, and turbulent jets.

3.2 Numerical Method

The governing equations in section 2.2 are general and are applicable to any finite volume grid, In this chapter, however, we focus on a cylindrical grid. The equations are now split into fluxes that contain radial terms and non-radial terms (azimuthal and longitudinal). Radial inviscid terms are integrated in time with an implicit Crank-Nicholson scheme and solved with a direct block-tridiagonal line solver. Only density, momentum and energy equations are coupled together and the Jacobian is derived for the inviscid terms. The viscous terms and terms involving heat of formation are treated explicitly. This method was chosen to eliminate stiffness due to the acoustic time-scale which was the limiting factor in the current

simulations. Linearization of energy was performed assuming constant heat capacity ratio, γ, which was locally computed based on species mass-fractions. The non-radial terms use the fully explicit second order Adams-Bashforth scheme, described by equation 2.24.

3.3 Cell Merging

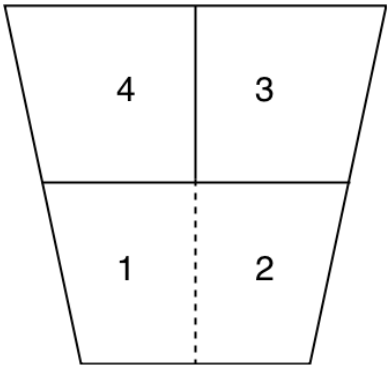

Figure 3.1: Cell merging schematic

Stiffness in the azimuthal direction arises from the very thin cells of size $O(\Delta r \Delta\theta)$ as we approach the centerline. By merging cells together in the azimuthal direction, we construct larger cells that do not impose a time step restriction as severe as thinner cells. When enough cells are merged to make the azimuthal spacing similar to the radial spacing, we effectively relax the time step restriction to depend on the radial spacing alone. In the process of merging cells, we have to ensure that fluxes from the merging process are still conservative. We describe the process using the schematic in Fig.3.1. The schematic shows 4 cells with cells labelled '1' and '2' being merged.

All terms on the right-hand side of the governing equations (2.20) are expressed as fluxes and can be represented by the following equation 3.2. In two dimensions, we write fluxes from four faces identified by directions North, South, East and West in the subscript.

$$\frac{\partial \phi}{\partial t} = -\frac{1}{V}\sum_{faces} \phi_f v_n A_f = \frac{1}{V}[F_N + F_S + F_E + F_W] \tag{3.1}$$

The finite volume equations for the unmerged cells C_1 and C_2 and merged cell C_{12} as shown in the schematic can be written as follows:

$$\begin{aligned}
\frac{\partial \phi_1}{\partial t} &= \frac{1}{V_1}[F_{1N} + F_{1S} + F_{1E} + F_{1W}] && = RHS_1 \\
\frac{\partial \phi_2}{\partial t} &= \frac{1}{V_2}[F_{2N} + F_{2S} + F_{2E} + F_{2W}] && = RHS_2 \\
\frac{\partial \phi_{12}}{\partial t} &= \frac{1}{V_{12}}[(F_{1N} + F_{2N}) + (F_{1S} + F_{2S}) + F_{2E} + F_{1W}]
\end{aligned}$$

Since $F_{1E} = -F_{2W}$ by construction, i.e. they are fluxes of the same face from opposite directions, we observe that the right-hand side (RHS) of the merged cell can be exactly written in terms of the RHS of the constituent cells as a simple volume weighted average.

$$\frac{\partial \phi_{12}}{\partial t} = \frac{(RHS_1)V_1 + (RHS_2)V_2}{V_1 + V_2} = \frac{\sum_n (RHS_n)V_n}{\sum_n V_n} \tag{3.2}$$

Having expressed the discretized equation for a merged cell, we extend the process to include the explicit time-integration in non-radial terms and implicit radial terms. A purely explicit method with cell-merging would be written as:

$$\delta\phi^t = h\frac{\sum_{fn} F_f^t}{\sum_n V_n} + R^t \tag{3.3}$$

The same procedure applied to a fully implicit Crank-Nicholson time-integration gives us:

$$\delta\phi^t + \frac{\Delta t}{2}\left[\frac{\sum_{fn} F_f^{t+1}}{\sum_n V_n} + \frac{\sum_{fn} F_f^t}{\sum_n V_n}\right] = R^t \tag{3.4}$$

We can now write the semi-implicit form: Crank-Nicholson in the radial direction and Adams-Bashforth in azimuthal and longitudinal directions for the unmerged cells and merged cell:

$$\delta\phi_1{}^t + \frac{\Delta t}{2}\left[\frac{F_{1N}^{t+1} + F_{1S}^{t+1}}{V_1} + \frac{F_{1N}^t + F_{1S}^t}{V_1}\right] + \frac{\Delta t}{2}\left[3\frac{F_{1E}^t + F_{1W}^t}{V_1} + \frac{F_{1E}^{t-1} + F_{1W}^{t-1}}{V_1}\right] = R_1^t$$

$$\delta\phi_2{}^t + \frac{\Delta t}{2}\left[\frac{F_{2N}^{t+1} + F_{2S}^{t+1}}{V_2} + \frac{F_{2N}^t + F_{2S}^t}{V_2}\right] + \frac{\Delta t}{2}\left[3\frac{F_{2E}^t + F_{2W}^t}{V_2} - \frac{F_{2E}^{t-1} + F_{2W}^{t-1}}{V_2}\right] = R_2^t$$

$$\delta\phi_{12}{}^t + \frac{\Delta t}{2}\left[\frac{(F_{1N} + F_{1S} + F_{2N} + F_{2S})^{t+1}}{V_1 + V_2} + \frac{(F_{1N} + F_{1S} + F_{2N} + F_{2S})^t}{V_1 + V_2}\right]$$
$$+\frac{\Delta t}{2}\left[3\frac{(F_{1E} + F_{1W} + F_{2E} + F_{2W})^t}{V_1 + V_2} - \frac{(F_{1E} + F_{1W} + F_{2E} + F_{2W})^{t-1}}{V_1 + V_2}\right] = \frac{R_1^t V_1 + R_2^t V_2}{V_1 + V_2}$$

In a regular polar grid, assuming $V_1 = V_2 = V$ in the azimuthal direction, we can write for n merged cells:

$$\delta\phi^t + \frac{\Delta t}{2}\left[\frac{\sum_{NS} F_f^{t+1}}{nV} + \frac{\sum_{NS} F_f^t}{nV}\right] + \frac{\Delta t}{2}\left[3\frac{\sum_{NS} F_f^t}{nV} - \frac{\sum_{NS} F_f^{t-1}}{nV}\right] = \frac{\sum_n R_n^t}{n}$$

Linearizing the fluxes for a coupled implicit line solve in the N-S direction:

$$\delta\phi^t + \frac{\Delta t}{2}\left[\frac{\sum_{NS} J_f^t \delta\phi_f^t A_f}{nV} + 2\frac{\sum_{NS} F_f^t}{nV}\right] + \frac{\Delta t}{2}\left[3\frac{\sum_{NS} F_f^t}{nV} - \frac{\sum_{NS} F_f^{t-1}}{nV}\right] = C(R^t)$$

In a more compact and general form, this can be written as:

$$\delta\phi^t + \frac{\Delta t}{2}\sum_{NS} C(J_f^t)\delta\phi_f^t = C(RHS_{CN}^t) + \frac{3}{2}C(RHS_{AB2}^t) - \frac{1}{2}C(RHS_{AB2}^{t-1}) + C(R^t) \tag{3.5}$$

where $C(x)$ is the coarsening operator defined as:

$$C(x) \equiv \frac{\sum_n (x) V_n}{\sum_n V_n} \tag{3.6}$$

Note that under a uniform azimuthal grid assumption, the coarsening operator is equivalent to a box filter.

Numerical implementation

All data is stored at the cell centers with face-centered quantities computed on the fly. The finite volume grid is structured and three-dimensional arrays are used to store all the variables for a simulation. In the current implementation, a regular cylindrical grid is assumed. The grid is allowed to be non-uniform in the radial direction to cluster cells near walls or shear layers. The grid is uniform in the azimuthal and longitudinal directions.

The cells in the azimuthal direction are then merged based on the azimuthal edge length $r\Delta\theta$. If this edge is smaller than the local radial edge of length Δr, n cells in the azimuthal direction are merged until the condition $nr\Delta\theta > \Delta r$ is met. The resulting grid is shown as a schematic in figure 3.2. The figure shows a quadrant of a cylindrical grid with different levels of merging. The cells closest to the pole have 4 cells merged into 1 cell, followed by 2 cells merged into 1 cell. The third level of cells are not merged. This condition used for merging ensures

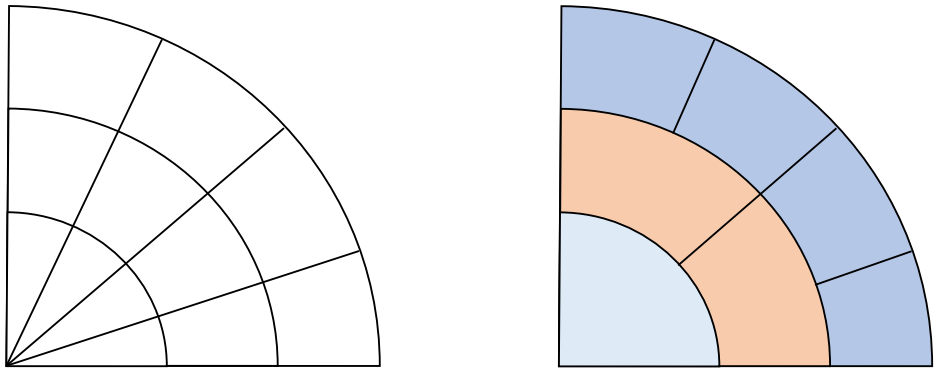

(a) (b)

Figure 3.2: Schematic of cell-merging of (a) a regular grid in cylindrical coordinates. A quarter of the grid is shown with three cells in the radial direction. (b) The merged grid is shown with different levels of merging

that the aspect ratio of the merged cell is least skewed.

In the first step, the fluxes are computed based on the cell-centered values stored on the fine grid. The jacobians for the implicit formulation, right hand side terms and source terms are computed for all the cells. Once this is done, the coarsening operator is applied on these terms as per equation (3.5). This step takes the values stored in the arrays and replaces them with the coarsened value for all cells that are being merged. These coarsened values are then used to compute the change in variable over time step ${\delta\phi_{12}}^t$. Since the coarsening operator is linear, $\delta\phi^t$ can be computed for each fine grid cell and the resulting ${\delta\phi_1}^t$ and ${\delta\phi_2}^t$ can be coarsened to achieve the same result.

This process of cell merging therefore operates on structured data and does not need unstructured representation. We also avoid resorting to complex block-structured meshes. The underlying structured data representation brings the benefit of a regular memory access, extensions to higher order flux reconstruction and as discussed in the next section: simpler parallelization with balanced loads.

Cost of Cell-Merging

Grid	Δt w/ C()	Δt w/o C()
8×8	0.79	0.77
16×16	1.42	1.37
32×32	3.92	3.72
64×64	13.4	12.6

Table 3.1: Cost of simulations in seconds per hundred iterations, with and without the coarsening operation

The cost of the merging operation is estimated by running the simulation with and without cell merging for the periodic pipe problem discussed in section (3.5). Table 3.1 shows the cost of the simulation in seconds per hundred time steps. This test was performed on small meshes on a single desktop processor. The time taken by merging is less than 7% of the total simulation time. This is therefore a very cost-effective solution to the stiffness posed by the azimuthal cell-size, which imposes an orders of magnitude larger cost due to time step limitation.

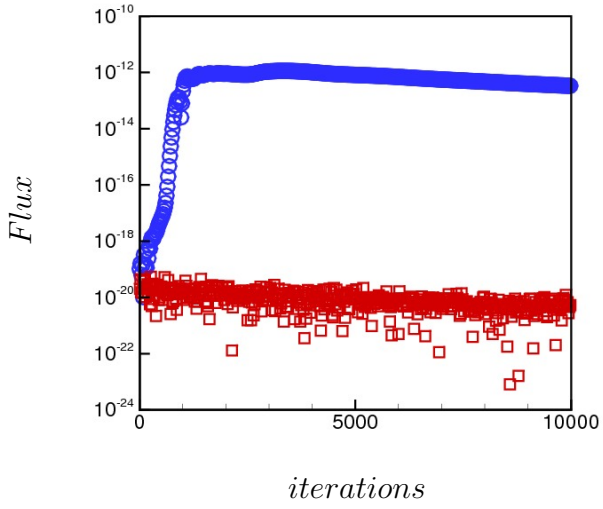

Figure 3.3: Conservation error: Total mass flux in shown in blue and the error due to merging as a function of time for the Lamb-Oseen vortex simulation is shown in red.

Discrete Conservation of Cell-Merging

The cell merging step effectively add fluxes together for the supercell from its constituent cells and therefore ensures discrete conservation of cell-centered quantities. This property is demostrated in figure 3.3 where the difference in total mass flux after the coarsening operation is shown as a function of simulation time for the Lamb-Oseen vortex problem, which is discussed in section (3.6). The comparison is made with the total mass flux in the domain which shows that the cell merging operation conserves to machine zero accuracy.

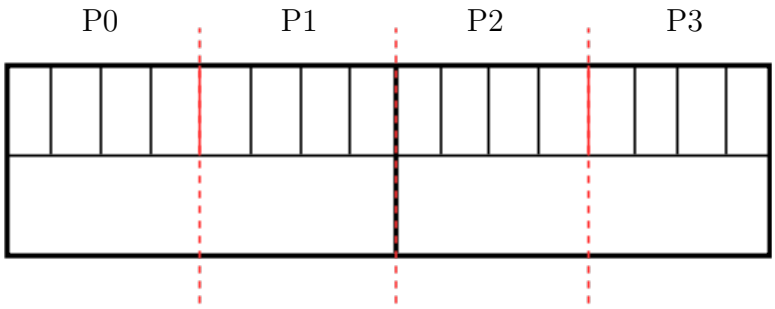

Figure 3.4: A schematic showing cell merging on parallel machines: In this case 16 cells are merged into 2 coarse cells but split among 4 processors as shown by the dotted lines

3.4 Parallel Algorithm for Merging

Large simulations on parallel computers can result in coarsened cells that span multiple processors. A parallel algorithm for coarsening is described in this section for 2^n cells in the azimuthal direction. If the azimuthal domain is split into 2^p processors and the cells are merged into 2^k coarse cells, a single coarse cell will span $2^p/2^k$ processors. Thus the coarsening operator has to be split across processors and this is achieved by successively applying the operator within a processor and then across processors:

$$C_{n/k}(x) = \frac{\sum_{2^n/2^k}(x)}{2^n/2^k} = \frac{\sum_{2^p/2^k}(\sum_{2^n/2^p}(x))}{2^p/2^k \times 2^n/2^p} = C_{p/k}(C_{n/p}(x))$$

Programmatically, this is accomplished in a Message Passing program by computing the local coarsening and storing it in an array with 2^p elements where each element would correspond to a processor. The inter-processor coarsening operator is applied next after gathing all elements using an *MPI_ Allreduce* call. The final value can now be stored in each grid cell.

The schematic in Fig. 3.4 represents the storage of cells in multiple processor domains. Here, 16 fine mesh cells are decomposed into 4 processors partitions and merged into 2 coarse cells. The 4 cells within each processor are first coarsened and stored in an array with 4 elements. The 4 element array is then coarsened into the final 2 coarse cells.

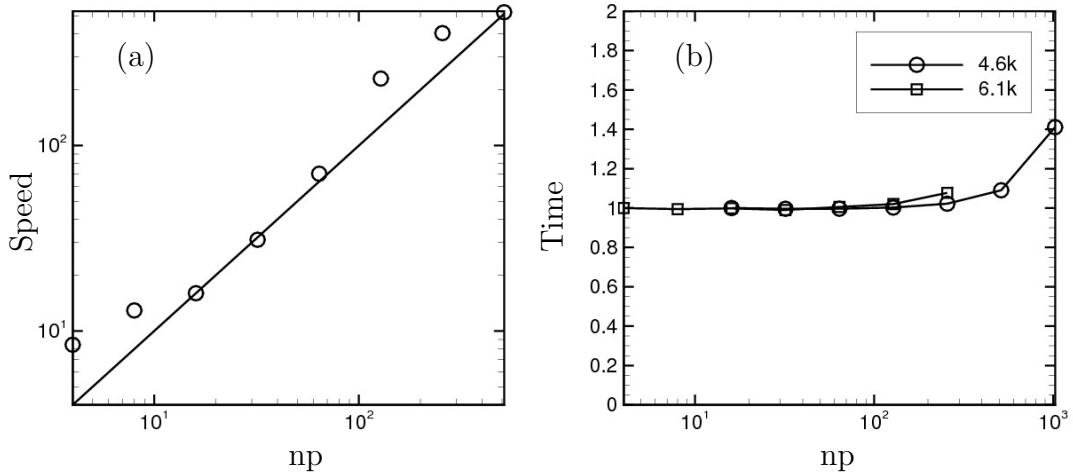

Figure 3.5: Scaling results for the parallel cell merging algorithm are shown: (a) plot of normalized speed versus number of processors showing Strong scaling using a grid with 590 thousand elements, (b) plot of normalized time versus number of processors showing Weak scaling with 4.6 and 6.1 thousand cells per processor.

Scaling tests were performed on Argonne National Laboratory's supercomputing facility and the results are shown in figure 3.5. The two plots correspond to strong scaling and weak scaling respectively. Strong scaling measures how much faster the program is executed upon increasing the number of processors for a given simulation. Weak scaling measures the time taken to execute the program with a constant number of grid elements per processor. Note that the scaling tests

shown in figure 3.5 try to measure the parallelizability in the radial direction only.

Strong scaling is shown in figure 3.5(a) and the plot shows scaled speed versus number of processors. The number of processors (np) ranges from 4 to 512. The speed of 16 processors is set as the reference for normalization as the underlying architecture of this supercomputer dictates that 16 processors form a single node. The straight line shows the linear speedup which is the goal for an algorithm to achieve. The grid used for this scaling test has (384,512,3) cells in the (r, θ, z) directions for a total of 589,824 elements. We obtain close to linear speedup for 32 and 64 processors. We also observe that superlinear speedup is obtained under two circumstances: below 16 processors and above 64 processors. Since a node on this architecture had 16 processors, using less processors provides each processor with more cache and other hardware resources per processor which is reflected by the additional speed. On the other end of the spectrum, with 128 or more processors, the number of grid elements per processor drops to 4,608 and below. With very few elements per node or processor, all the data would be stored on the cache. Without the need to transfer data back and forth from the slower main memory, the program executes faster which again results in superlinear speedup. However, with more processors, the cost of communication increases and this reduces the benefit from superlinear speedup.

Weak scaling is shown in figure 3.5(b) with two datasets. In this test, the objective is achieve contant runtimes for any number of processors since the workload per processor remains constant. As with the strong scaling test, the cost of communication increases with the number of processors and the program would take longer to complete. Two different workloads were tested here with 4,608 and 6,144 elements per processor. The number of elements in the azimuthal direction in the

first dataset was 8 times the number of processors and the second dataset had 2 times the number of processors. The first dataset also had 4 processors assigned in longitudinal direction which allowed testing upto 1024 processors. Both datasets indicate almost linear scaling upto 128 processors in the azimuthal direction. Using 256 processors, while not linear, still results in faster execution.

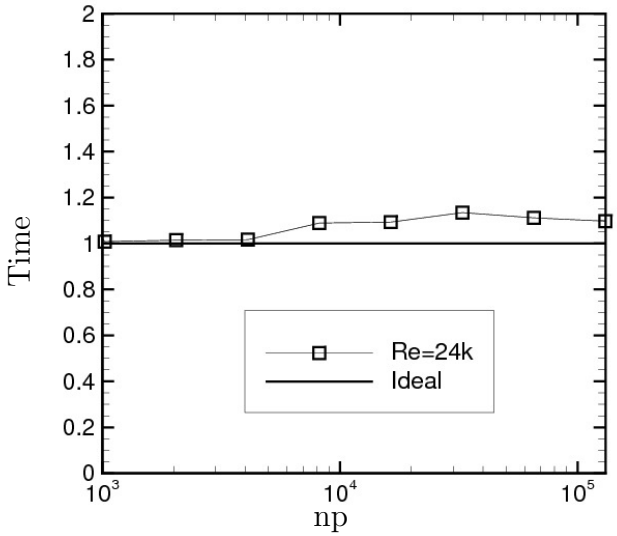

Figure 3.6: Weak scaling plot showing normalized time versus number of processors with 10.2 thousand cells per processor.

The program is fully parallel in the longitudinal direction as well and has been run efficiently on hundreds of thousands of processors. Accounting for parallelization in all three axes, the algorithm can potentially scale up to a million or more processors. Weak scaling in the longitudinal axis in addition to the azimuthal axis scales well up to a hundred thousand processors as shown in figure 3.6. In this plot, the number of processors in the azimuthal direction is kept constant at 256

and more processors are added in the longitudinal direction. The grid used has (640,4,4) cells per processor for a maximum of (640,1024,2048) cells corresponding to (1,256,512) processors in the (r, θ, z) direction respectively. This corresponds to a weak scaling study with 10,240 cells per processor. The largest grid tested has $1.34 Billion$ cells on 131,072 processors. This grid was designed for and is currently being used for a Direct Numerical Simulation (DNS) of a reacting jet at a Reynolds number of $23,600$.

3.5 Periodic laminar pipe

A fully developed laminar pipe flow (Hagen-Poisueille Flow) is simulated for validation of the scheme and to confirm second order accuracy. The analytical solution for pipe flow is:

$$u(r) = \frac{Re}{4} F_b (1 - r^2) \tag{3.7}$$

where $u(r)$ is the streamwise velocity, Re is the Reynolds number, F_b is the body force and r the radial distance. The diameter of the pipe is denoted by D and the bulk velocity U_b. The body force is set to $F_b = 4/Re$ and $Re = 1$ for all cases tested. The grid size is varied from 8×8 to 64×64 in the radial and azimuthal directions respectively. All cases are simulated up to three flowthrough time-units, $3D/U_b$, which was found to provide a converged solution. Figure 3.7 shows the velocity profile from different grid resolutions and the order of accuracy estimated to be second order.

In figure 3.8 we estimated the maximum time step that could be taken with and without the coarsening operation. When the limiting grid size changes from $\Delta r \Delta \theta$

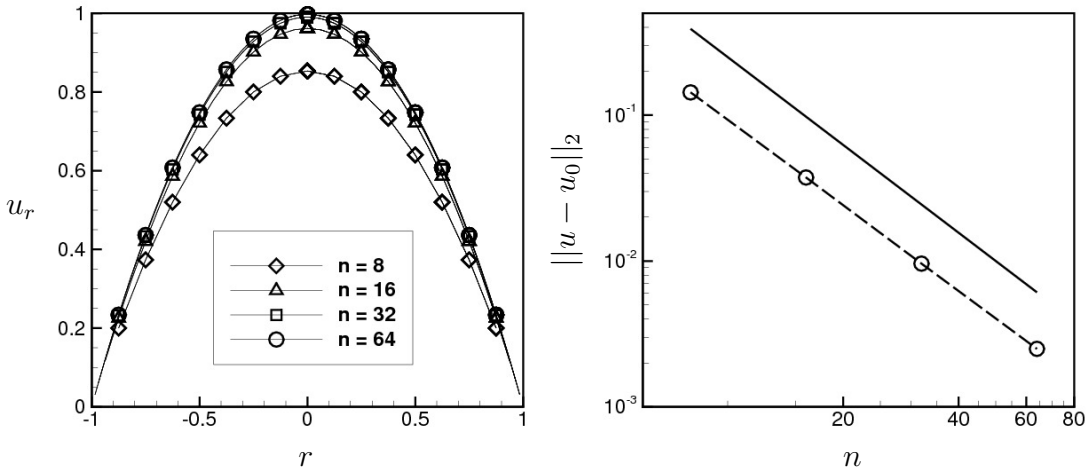

Figure 3.7: (a) Streamwise velocity profile vs radial distance for different grid resolutions (b) Log plot of L2 error norm versus grid cells in the radial direction. The solid line indicates a slope of -2.

to Δr the maximum time-step that can be taken should increase proportionately. Note that without coarsening the smallest cell spacing is $\Delta r \Delta\theta/2$ in the azimuthal direction whereas with coarsening it is Δr. The viscous time limit for an explicit method in one-dimension is $\nu\Delta t/\Delta x^2 \leq 1/2$ We observe this behavior in figure 3.8 where merging (line with circles) increases the maximum time step size by orders of magnitude compared to the case without merging (line with squares). In addition, the time step decrease is proportionate to the square of grid spacing. Without merging, the time step drops faster as the smallest grid spacing depends on Δr and $\Delta\theta$.

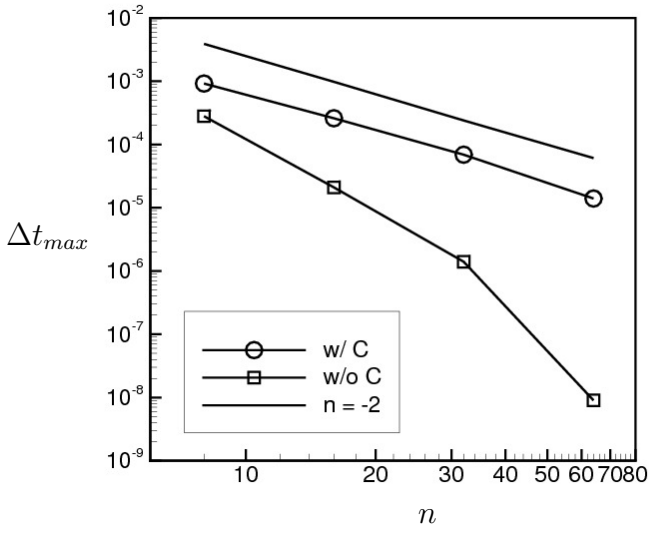

Figure 3.8: Maximum time step size vs analytical limit. Simulations with cell merging are shown in circles and squares without. The solid line is drawn at a slope of -2

3.6 Lamb-Oseen vortex

The Lamb-Oseen vortex is another axisymmetric fluid flow problem with an analytical solution to the incompressible Navier-Stokes equations. While the radial velocity field is axisymmetric, the cartesian velocities are not and since we solve for cartesian velocities, this problem is a good validation test on a cylindrical mesh. This problem is also different from the pipe flow in that there is a non-zero velocity field in the $r-\theta$ plane. The governing equation and its analytical solution for the Lamb-Oseen vortex can be written for the vorticity field, ω as :

$$\frac{\partial \omega}{\partial t} = \nu \nabla^2 \omega \tag{3.8}$$

$$\omega = \frac{\Gamma_0}{4\pi\nu t} e^{-r^2/4\nu t} \tag{3.9}$$

The azimuthal velocity field corresponding to the vorticity solution expressed as a function of radial distance and time can be written as follows:

$$v_\theta(r,t) = \frac{\Gamma_0}{2\pi r}\left(1 - e^{-r^2/4\nu t}\right) \tag{3.10}$$

where v_θ is the azimuthal velocity field, Γ_0 is the initial circulation, r is the radial distance, t is time and ν is kinematic viscosity.

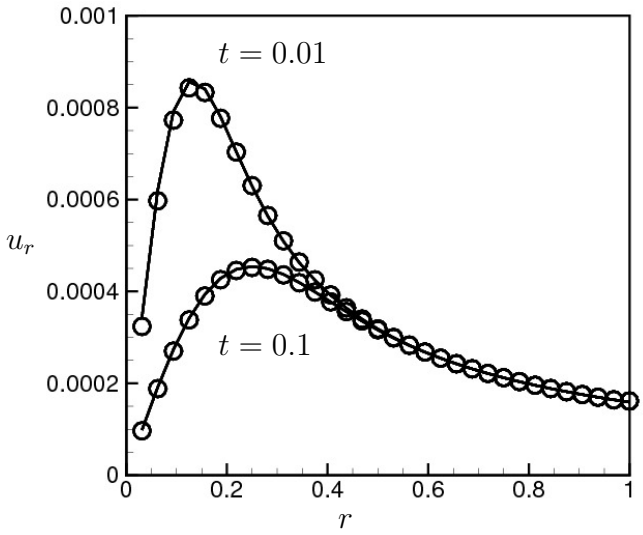

Figure 3.9: Velocity vs radial distance at times t = 0.01 and t = 0.1. The circles are the numerical simulation compared with the solid lines from the analytical solution

The comparison between the analytical velocity profile and simulation result as a function of radial distance from the vortex center is shown in figure 3.9. The

parameters used for the simulation are $\Gamma_0 = 0.001$, $\nu = 0.01$ and the initial radius at time $t = 0$ was set to $r_0 = 0.1$. The (r, θ) grid was $(64, 64)$ for this simulation. The figure shows the solution obtained at two instants, $t = 0.01$ and $t = 0.1$ from the initialization. Since the solution is a decaying velocity field in time, the comparison is made at different time instants and the numerical solution is expected to capture the decay in time and the spatial changes in the field. The numerical solution shown by circles are compared with the analytical solution plotted as solid lines. We observe good agreement with the theoretical solution.

3.7 Turbulent Cold Jet

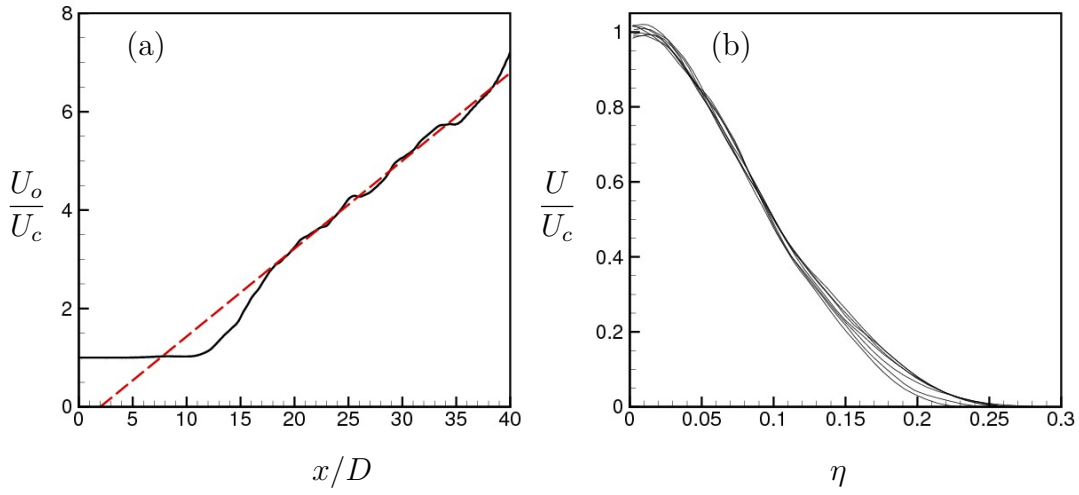

Figure 3.10: (a) Centerline velocity vs axial distance (b) Self-similarity of axial velocity cross-section with profiles taken between 18D and 30D downstream

The merging algorithm was developed to perform very large scale Direct Numerical Simulations (DNS) of reacting round jets and in this section we discuss

the results from a cold jet. The simulation is carried out on a fairly coarse grid to demonstrate the robustness of the numerical method. The jet is simulated at a Reynolds number of $2,400$ on a domain of $20D \times 2\pi \times 45D$ where D refers to the jet diameter. The grid had $(80, 64, 450)$ cells in (r, θ, z) directions with a total of $2.3M$ elements. The inflow was specified using a hyperbolic tangent function, which closely approximates a top-hat profile but has smooth edges and was initially perturbed with random velocities of magnitude 0.1%. The cells in the radial directions were clustered near the center and in the axial direction the cell density was gradually decreased downstream. The simulation is compressible and the Mach number of the jet was set to 0.2 to minimize compressibility effects.

The results obtained are shown in figure 3.10. U denotes jet velocity in the streamwise direction, U_o is the velocity at the inlet and U_c is the centerline velocity. The centerline velocity U_c follows a $1/x$ scaling as seen in figure 3.10(a) where the normalized inverse centerline velocity U_o/U_c increases linearly with the slope of dashed red line. Figure 3.10(b) shows the self-similarity of the jet where the axial velocity cross-section profiles are taken from $18D$ to $30D$ downstream of the inlet. The velocity ratio U/U_c is plotted against the self-similar variable $\eta = r/(z - z_0)$ for all the profiles taken and can be seen to collapse onto each other. We obtain a velocity decay constant of $B_u = 5.6$ and a spreading rate of $S = 0.99$ which compares well with experimental observation of Hussein et al. [21] and Panchapakesan & Lumley [38]. The potential core was also observed to close $11D$ downstream of the inlet which matches well with the simulation results of Babu & Mahesh [3] and Boersma et al. [4]. This simulation shows that the cell merging algorithm can is able to handle a turbulent flow-field and produce results that compare well with existing data while offering an increased time-step

and lower grid cell cost.

3.8 Conclusion

A conservative finite volume formulation to prevent the restrictive time-step limitation from a cylindrical grid has been presented. Extremely thin grid cells close to the centerline are merged together in the azimuthal direction to form thicker cells with an aspect ratio close to 1. The cell width is thus effectively increased which removes the excessive time-step limitation. This method also allows an implicit time integration in the radial direction without coupling the azimuthal terms.

Chapter 4

Laminar simulations

Laminar simulations of autoigniting jets are performed to gain knowledge from the simplified problem where the effect of initial turbulence is absent before we attempt to study the fully turbulent flames. In this simplified configuration we tested different fuels and compared results. These simulations help determine the grid requirements and sensitivity of the problem to inlet and boundary conditions.

4.1 Two-dimensional unsteady reacting jet

We perform two dimensional simulations of an autoigniting flame. Cold nitrogen-diluted fuel is injected into hot ambient air. This problem has practical applications ranging from compression ignition engines, internal combustion engines with exhaust gas recirculation to gas-turbine combustors with hot product recirculation. The 'vitiated coflow burner' by Cabra *et al.*[6] and the 'jet in hot coflow' burner by Dally *et al.*[8] are model flames of such applications.

Three fuels: hydrogen, methane, and ethylene are simulated in a two-dimensional slot-jet like geometry. A cold fuel jet at $M_{jet} = 0.3$ issues into heated air with

a coflow velocity one-third of the jet. The Mach number is defined based on the characteristic velocity set to the speed of sound of the fuel jet. The hydrogen jet uses the Mueller *et al.*[35] mechanism whereas a 17-species skeletal mechanism for methane [48] and a 22-species reduced mechanism for ethylene [54] are chosen to speed up the calculations of otherwise prohibitively expensive mechanisms for hydrocarbons. Table 4.1 lists the inlet conditions for the jet and the coflow. The jet and coflow velocities are not varied across the fuels. The inlet velocity profile is given by the following equation with $\delta = 0.01H$, where H is the width of the slot jet:

$$u_{in} = \frac{u_{jet} - u_{coflow}}{2}\left[1 - \tanh\left(\frac{|y| - H/2}{2\delta}\right)\right] + u_{coflow} \tag{4.1}$$

Fuel	T_{fuel}	T_{air}	Y_{fuel}	Y_{O_2}	Re	U_{jet}	U_c
H_2	1	3.5	0.029	0.233	3600	0.3	0.1
CH_4	1	5.0	0.055	0.220	7200	0.3	0.1
C_2H_4	1	5.5	0.082	0.299	7200	0.3	0.1

Table 4.1: Fuels and their respective inlet conditions

Non-reflecting far field boundary conditions [45] are applied at the other three faces. The domain is $40H \times 40H$ along the length of the jet and across the jet. Figure 4.1 is a temperature contour plot of the three jets. They are at different stages of combustion with hydrogen sustaining a stable lifted flame and the hydrocarbons with small autoignition kernels. The hotter coflow needed to ignite the hydrocarbons had the effect of reducing the coflow density, which led to thick shear layers with little reaction at $Re = 3600$. This was the reason to increase the Reynolds number to 7200 for the hydrocarbons which allowed

increased mixing along the shear layer.

Figure 4.3 is scatter plot of temperature plotted against the mixture fraction (at every computational volume) over different regions of the computational domain. $z = 0$ indicates pure oxidizer, (originally at a high temperature $T/T_r = 3.5$) and $z = 1.0$ indicates pure fuel (originally at a cold temperature $T/T_r = 1$). Towards the left half of the domain, $x < 20H$, figure 4.3(a) shows the absence of any chemical reaction. Figure 4.3(b) (corresponding to the instantaneous contours shown in figure 4.2(a) depicts the auto-ignition of fuel; note that auto-ignition appears to begin at lean, relatively hotter regions of the flow, and the reaction then spreads to the fuel-rich regions (as shown in figure 4.3(c)). Figure 4.3(d), corresponding to the right half of the domain, indicates that the lean mixture is completely burnt (as evidenced by the temperature) and that the domain contains a significant amount of unburnt, fuel-rich region.

The more interesting aspect of this lifted flame was the flame base towards the center of the domain. Here the flame appears to leapfrog a vortex pair in front of it, and while it grows stronger in temperature levels it also gets advected downstream before it makes the jump again over the next set of vortices. Fig. 4.4 illustrates this process which shows a sequence of frames from $\tau_j = 180$ to $\tau_j = 195$ where τ_j is non-dimensional time with the reference time being the time taken for the jet to cover one jet width. The corresponding Y_{HO_2} contours however reveals that this peculiar leapfrogging is aided by autoignition. With a high concentration of Y_{HO_2} radicals, understood to be an important indicator of autoignition [30], along the shear layers of the jet well ahead of the temperature rise, an increase in temperature or thermal runaway is simply waiting to happen. The high shear along the vortices' edges expose these radicals to the much hotter

coflow which could initiate thermal runaway and hence explain our observation. The scatter plots from fig. 4.3 are consistent with this explanation that leads to the lean hot mixtures igniting first. A similar mechanism was found to play a role in a turbulent auto-igniting lifted slot jet simulation [57].

4.2 Reacting round jet

A round jet is the first set of results which is three dimensional. The experiment by Cabra *et al.*[6] serves as a reference for this case although we perform the simulation at a much lower Reynolds number than what was measured in the experiment.

The jet inlet velocity is specified with the hyperbolic tangent profile given by

$$u_{in} = \frac{u_{jet} - u_{coflow}}{2}\left[1 - \tanh\left(\frac{r - D/2}{2\delta}\right)\right] + u_{coflow} \tag{4.2}$$

For this calculation, $\delta = 0.01D$. The Reynolds number of the jet is $Re_{jet} = 7200$ and the domain size is $40D \times 40D \times 40D$ where D is the diameter of the round jet. The grid used for the simulation is Cartesian. Non-reflecting boundary conditions are applied at the side and exit planes. Turbulent fluctuations in the form of homogeneous isotropic turbulence are not added to the inlet, something often done in DNS studies of turbulent autoigniting flames [57]. Improved transport properties are taken into account with viscosity modified by temperature, modelled with a power law, $\mu/\mu_\circ = (T/T_\circ)^{0.67}$, and species are allowed to have different Schmidt numbers[18]. The effect of Lewis numbers on hydrogen flames is important and can affect autoignition times and intensities [11, 12]. This simulation took a total of $0.2M$ cpu-hours and was run on 1024 cpu-cores.

For these conditions a laminar flame close to the inlet is observed. Contour plots in fig. 4.5(a) and 4.5(b) show the contours of temperature and Y_{OH} which are correlated with a lifted height of the flame at $x = 4D$, Y_{HO_2} in 4.5(c) however is leading the flame by almost one jet diameter again indicating a autoignition based flame stabilization. Figure 4.6 illustrates with a cutaway of isocontours and we can see the substantial buildup of blue Y_{HO_2} structures ahead of the orange temperature increase zones.

A plausible reason for this flame to remain laminar in spite of the high Reynolds number is likely due to the low lift-off height where expansion due to the flame's heat release stabilizes upstream instabilities. The effect of hydrogen's low Lewis number also leads to faster ignition [11]. This effect is also clear in fig. 4.5(d) where the mixture fraction shows increased diffusion after the flame anchor location. The effect of adding high turbulence intensities at the jet inlet to the lifted flame height will be explored in the next chapter plays a role in differentiating our laminar observation with the turbulent flame in Yoo *et al.*[57].

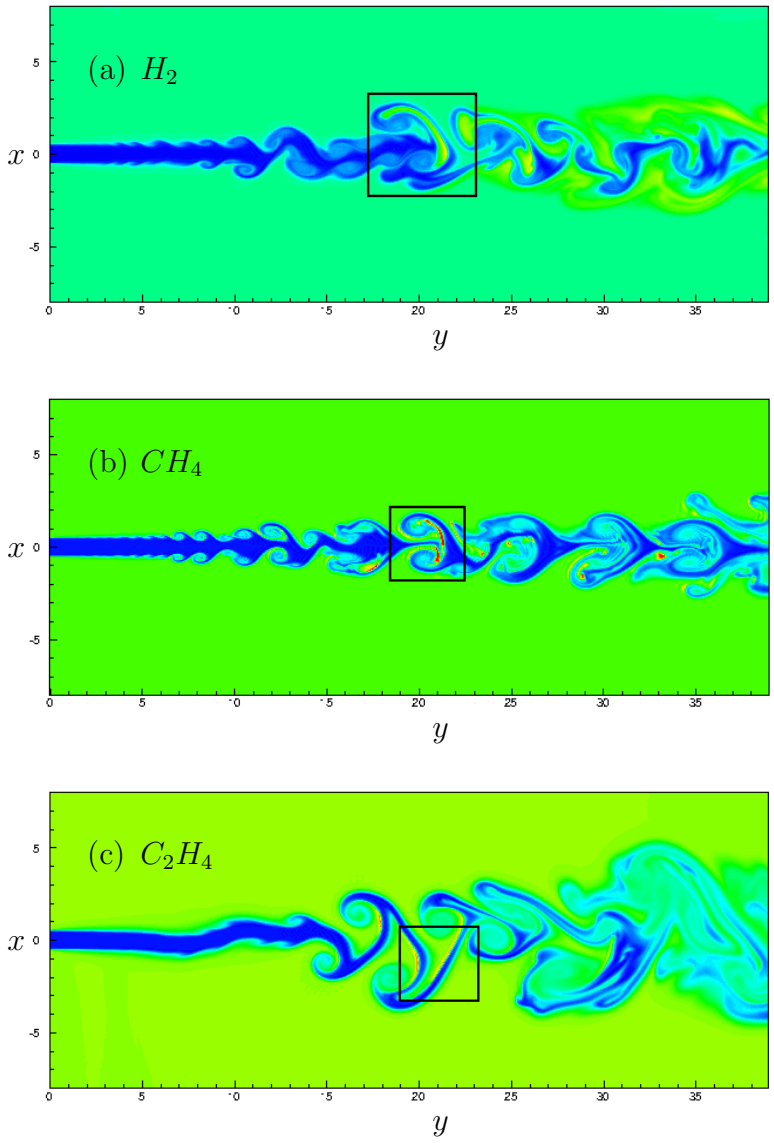

Figure 4.1: Normalized temperature contours for (a) H_2, (b) CH_4, and (c) C_2H_4 ranging from 1 to 8, corresponding to blue and red respectively. The box highlighting autoigniting flame kernels is shown in detail in Fig. 4.2

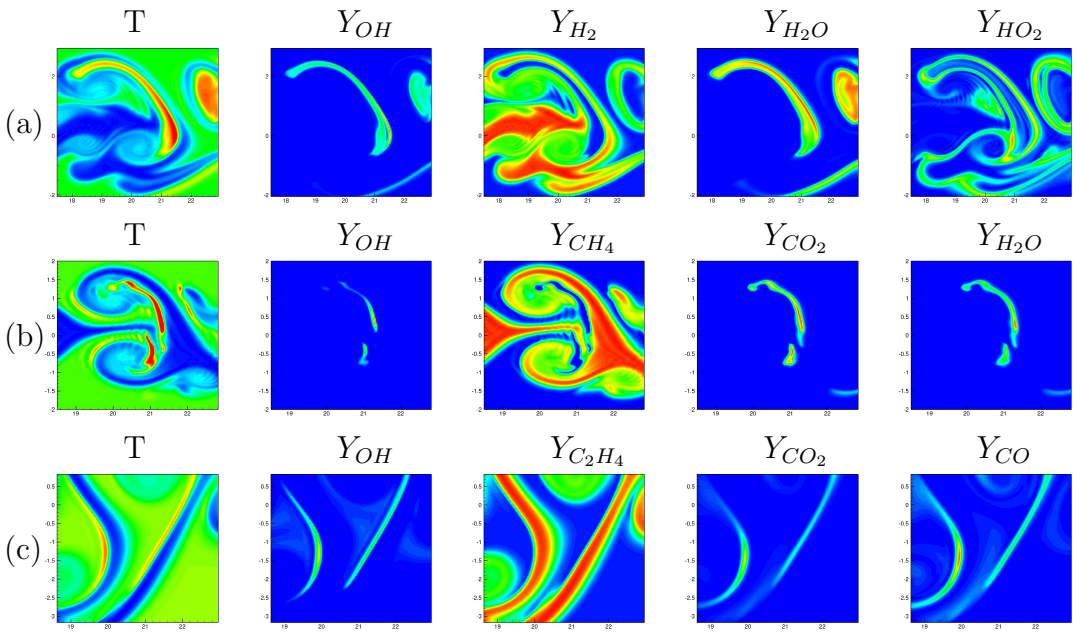

Figure 4.2: Autoigniting flame kernels for (a) H_2, (b) CH_4, and (c) C_2H_4 respectively

(a) $x = [0, 20]$ (b) $x = [20, 22.5]$

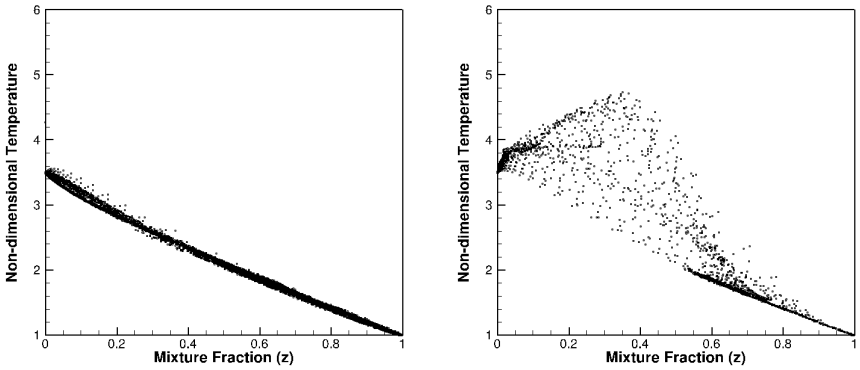

(c) $x = [22.5, 25]$ (d) $x = [25, 40]$

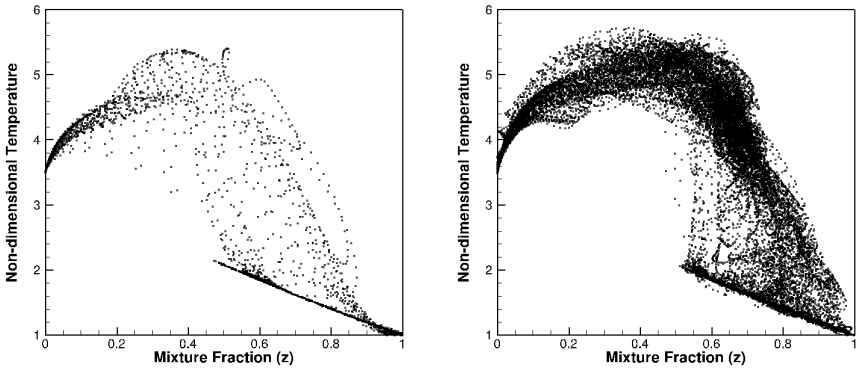

Figure 4.3: Scatter plot of temperature against mixture fraction at various intervals of x (in units of jet diameter H). The auto-ignition of fuel at lean conditions is evident in (b) and (d) indicates that the lean mixtures have completely burnt, while there is still unburnt rich fuel indicated by the thick line at the bottom right corner.

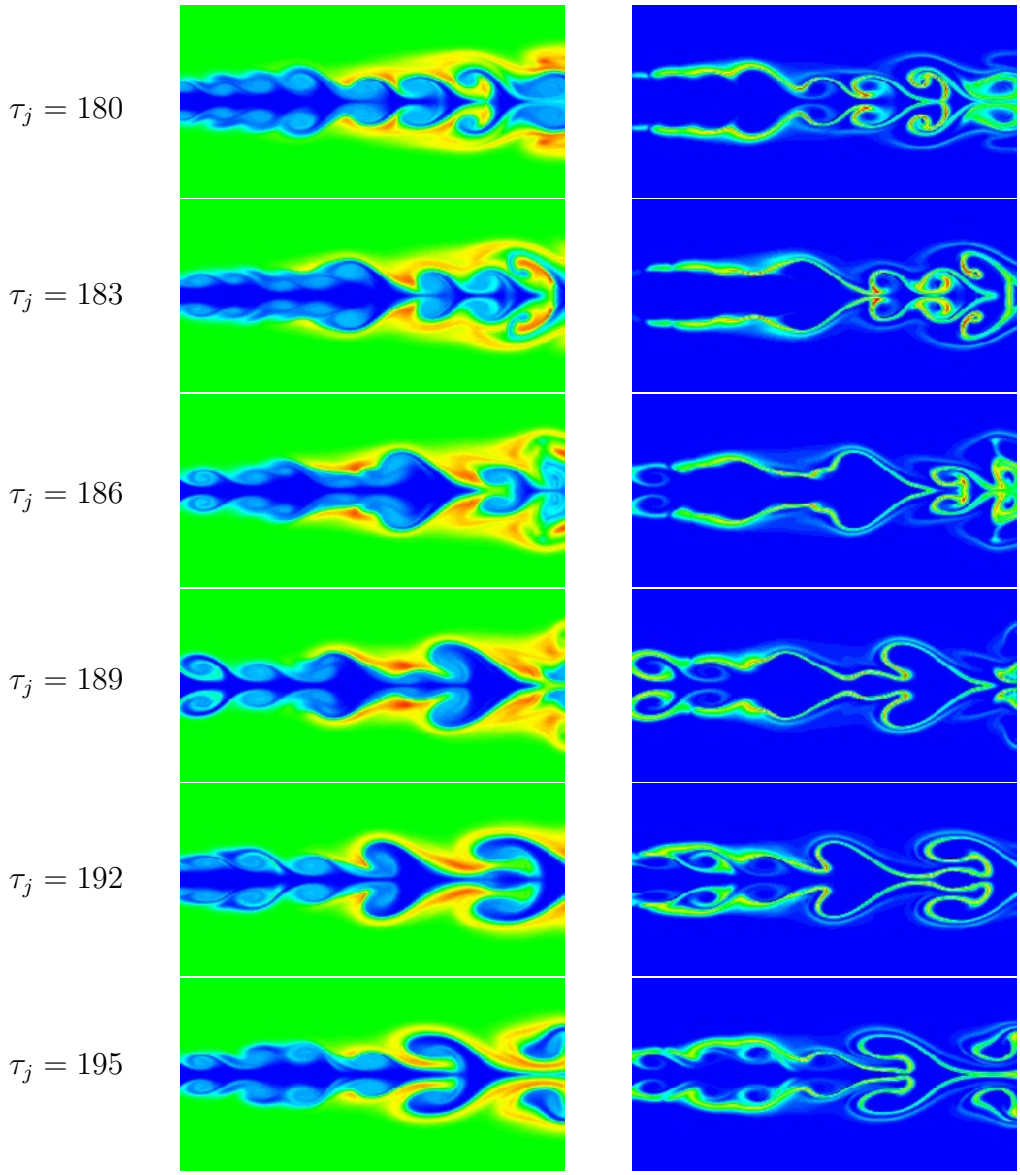

Figure 4.4: Temporal evolution of (a) temperature and (b) Y_{HO_2} at the base of the lifted flame from $\tau_j = 180$ to $\tau_j = 195$

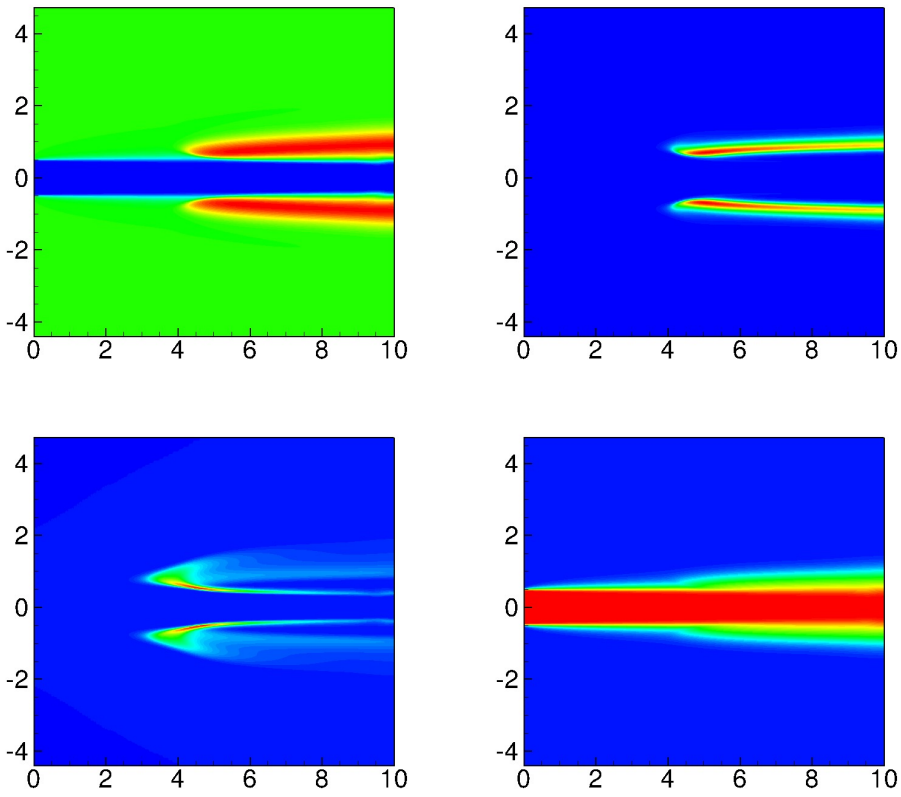

Figure 4.5: Contour plots of (a) Temperature, (b) Y_{OH}, (c) Y_{HO_2}, and (d) Mixture fraction ζ for the round jet

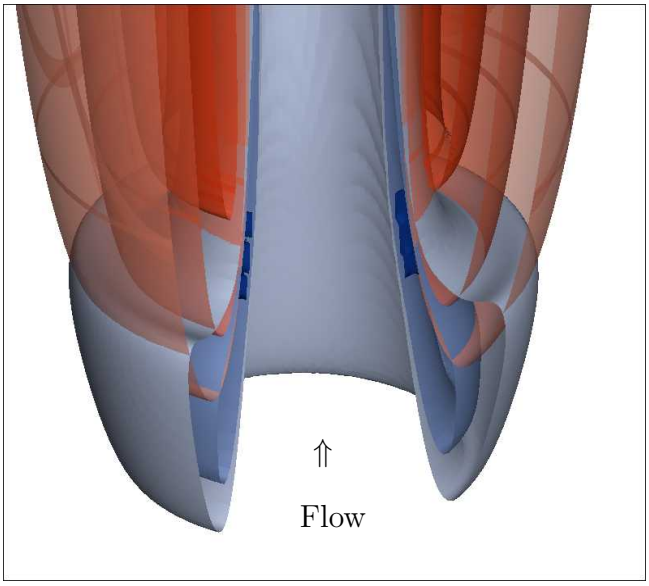

Figure 4.6: Flame cutaway superposing the two sets of isosurfaces, the bluish-gray isocontours of Y_{HO_2} positioned below the orange temperature isocontours indicate that the flame is stabilized by autoignition.

Chapter 5

DNS of Turbulent Round Jet Flame

5.1 Problem Statement

A cold fuel jet is injected into hot coflowing oxidizer which results in a lifted autoignition stabilized flame. The fuel jet is hydrogen diluted with nitrogen with a hydrogen mass-fraction of $Y_{H_2} = 0.029$ and at a temperature of $298K$. The hot coflowing oxidizer is air, oxygen diluted with nitrogen with an oxygen mass-fraction of $Y_{O_2} = 0.233$ at a temperature of $1043K$. The Mach number of the jet based on bulk velocity is 0.3. The jet's bulk velocity is $123.8m/s$ and the coflow velocity is one third of the jet's bulk velocity at $41.3m/s$. The inlet velocity profile for the fuel jet is that of a fully developed turbulent pipe. The coflow velocity is specified as a hyperbolic tangent function at a magnitude of one-third of the jet's bulk velocity. The open far-field is assumed to held at atmospheric pressure. The jet is assumed to be issuing from a pipe with an inner diameter of $5mm$ and an outer diameter of $5.5mm$. The reference length scale is $5mm$ and reference

temperature and pressure are $298K$ and $1atm$.

A schematic of the jet flame is shown in figure 5.1. The arrows at the bottom indicate the inlet velocity profile. A constant coflow velocity and a turbulent pipe outflow is seen along with a dip in velocity between the two due the finite thickness of the pipe. Intermediate radicals form along the shear layer which lead to autoignition and a high temperature combustion zone or flame.

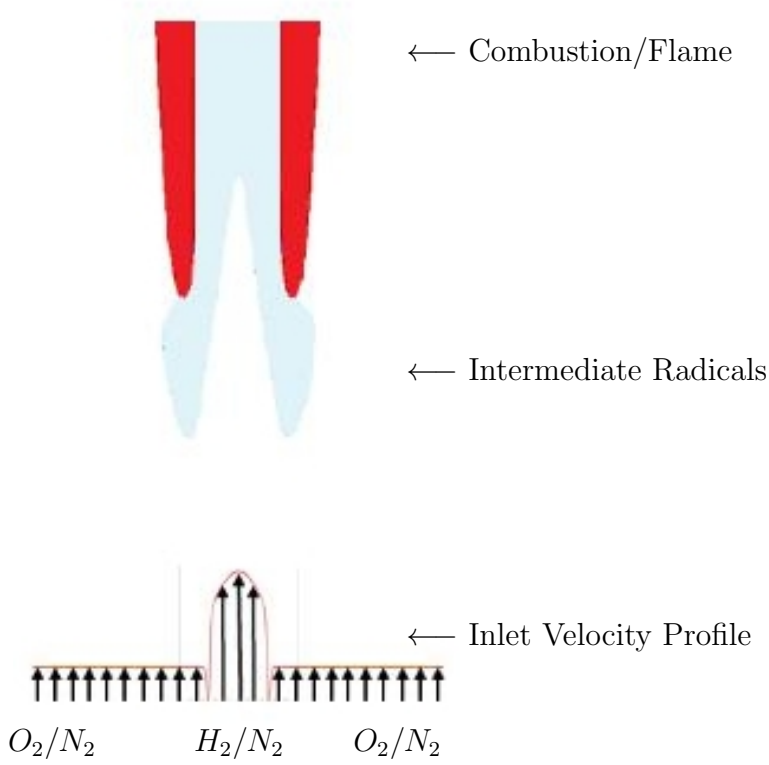

Figure 5.1: Turbulent jet flame schematic.

5.2 Computational Domain

This simulation was performed on a cylindrical grid with $84M$ elements. The grid has $(320, 512, 512)$ cells in (r, θ, z) directions. The computational domain is $(10, 2\pi, 10)$ jet diameters in (r, θ, z) directions.The grid is uniform in the azimuthal and axial directions. In the radial direction, the cells are clustered along the shear layer at $r = 0.5$. This clustering is needed to capture the turbulent boundary layer from the turbulent pipe inflow and the rolling up of the jet's shear layer. The mixing within the shear layer determines the scalar dissipation rates which can have a large effect on autoignition delay.

The grid spacing in the radial direction is changed linearly between control points along the radius. At $r = 0$, the radial spacing is $0.01D$ and is kept constant up to $r = 0.3$. The spacing then reduces to a minimum of $0.005D$ at $r = 0.5$, which corresponds to the location of jet's turbulent shear layer. The spacing goes back up to 0.01 at $r = 1$. At $r = 2$, the grid spacing is $0.021D$. At $r = 5$, the grid spacing is $0.05D$ and from this point, the grid is coarsened fairly rapidly to a final spacing of $0.2D$ at $r = 10$. In the axial direction, the grid spacing is a constant $0.0195D$. In the azimuthal direction, there are 512 points with a uniform spacing of $0.0123rad$. This corresponds to $0.0123D$ at $r = 1$. Note that the cell merging process reduces the effective azimuthal spacing to roughly the same as the radial spacing as we get closer to $r = 0$.

The time step for the simulation was kept constant at $\Delta t = 0.0005$. The simulation was run for $45D/U$ non-dimensional time units on 512 processors for a total of $0.5M$ *cpu-hours* on the Itasca cluster at Minnesota Supercomputing Institute.

5.3 Turbulent pipe simulation & validation

A fully developed pipe simulation is performed to obtain the inlet velocity conditions for the turbulent fuel jet. This provides realistic inlet velocity conditions for as against perturbing the flow with random noise or superposing homogeneous isotropic turbulence. The pipe simulations are performed with a separate solver that was written for incompressible pipe flows by Charles Pierce [41]. It uses a second-order staggered grid discretization and a second-order time advancement on a structured cylindrical grid.

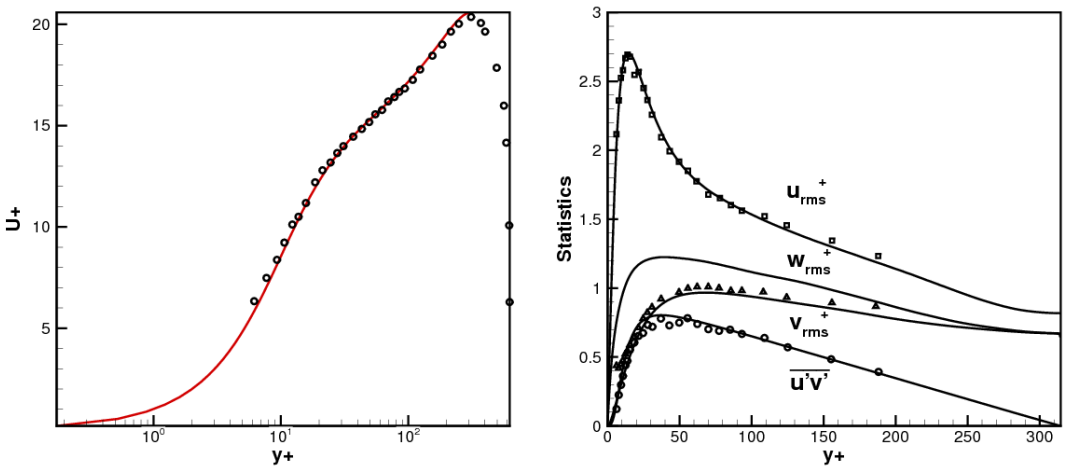

Figure 5.2: Turbulent pipe flow comparison, mean velocity and turbulent intensities, with den Toonder & Nieuwstadt [9]. Simulation results are shown as straight lines and the experiment in symbols.

A domain size of $(0.5D, 2\pi, 5D)$ with $(256, 512, 512)$ points in the (r, θ, z) directions defines the grid used for the pipe simulation. The grid spacing is non-uniform

in the radial direction to capture the boundary layer at the wall. The radial spacing in the wall normal direction is a minimum of $\Delta r^+ = 0.34$ at the wall. The grid spacing in wall units is $\Delta z^+ = 6.14$ in the axial direction. The maximum spacing in the azimuthal direction at the wall is $\Delta\theta^+ = 7.72$. The Reynolds number based on the bulk velocity and pipe diameter was $10,000$ which is chosen to match the inlet Reynolds number used for the turbulent flame simulation. The friction Reynolds number based on the pipe diameter is $Re_\tau = 629$. The numerical results are validated against the experimental measurements by den Toonder & Nieuwstadt [9] and the comparison is shown in figure 5.2. Note that we obtain good agreement for the mean velocity and the second order statistics: u^+_{rms}, w^+_{rms} and $\overline{u'v'}$.

Once the flow statistics reach a steady state, instantaneous velocity data is collected at a single plane and written to a file continuously as a function of time and space (r, θ). Data was collected for $2,000D/U_{bulk}$ non-dimensional units of time for the current simulation. This file is then read by the compressible solver and interpolated in time and space onto the jet's inlet plane for all cells that lie within $r = 0.5D$. The collected data was long enough that there was no need to run the pipe simulation longer or to reuse the data. This process of obtaining fully developed velocity profiles from a separate pipe simulation ensures that the fuel jet has a realistic velocity inlet condition that would correspond to the experimental fuel injection from a long pipe into the coflow. Figure 5.3 shows the total vorticity at the inlet plane of the jet simulation after the velocities from the pipe are interpolated.

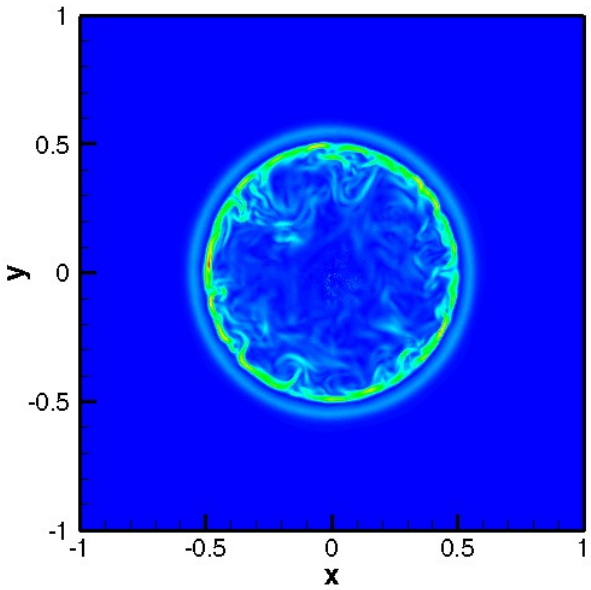

Figure 5.3: Vorticity magnitude on the inlet plane showing the interpolated turbulent pipe flow

5.4 Results & Discussion

5.4.1 Mean flow description

The turbulent flame can be described as a lifted flame which can be split into three zones: pre-ignition, ignition and post-ignition. The turbulent flame is anchored at a distance of 4.5 jet diameters downstream. In the pre-ignition phase, the two streams: the cold fuel jet and the hot oxidizer coflow, mix along the turbulent shear layer producing a pool of intermediate species. This radical pool forms in a near isothermal environment, i.e., the process is not exothermic and

is mildly endothermic. The temperature stratification along the mixing layer implies that more radicals are produced closer to the hotter oxidizer than the cold fuel. Once the radical pool reaches a critical mass, chain reactions lead to thermal runaway and a rapid increase is temperature is observed. This is autoignition and the process stabilizes and anchors the flame at the observed lifted height. Post-ignition, the high temperature radical pool along with the product actively mixes with neighboring reactive mixtures and spreads the flame. This process can be premixed flame propagation along unburnt but mixed fuel-oxidizer mixtures or diffusion-like flame thickening as fuel and oxidizer diffuse into the burning flame.

Figure 5.4 shows an instantaneous isometric view of the fully reacting turbulent jet simulation. A contour of vorticity magnitude at the inlet plane shows the turbulent structures from the fully developed pipe flow. The turbulent structures in the jet's shear layer are seen in the isosurfaces of the Q-criterion. This is followed by the isosurface of the HO_2 radical a few diameters downstream which initiates the autoignition process. This leads to a thermal runaway and the next set of isocontours further downstream show the high temperatures of the flame.

In figure 5.5, the temporally and radially averaged temperature and product fields show the lifted flame structure. The contour map?s x-axis is the axial distance and the y-axis the radial distance. The cold fuel and hot oxidizer mix and at the interface a lifted flame indicated by the increasing temperature in figure 5.5(a) and corresponding increase in product concentration shown in figure 5.5(b). The mixture fraction field in figure 5.5(c) shows the evolution of scalar mixing along the shear layer. Post-ignition the divergence and increased viscosity due to heat release causes rapid spreading of the scalar field. In figure 5.5(d) the OH radical which is a high temperature radical indicates the position of the flame.

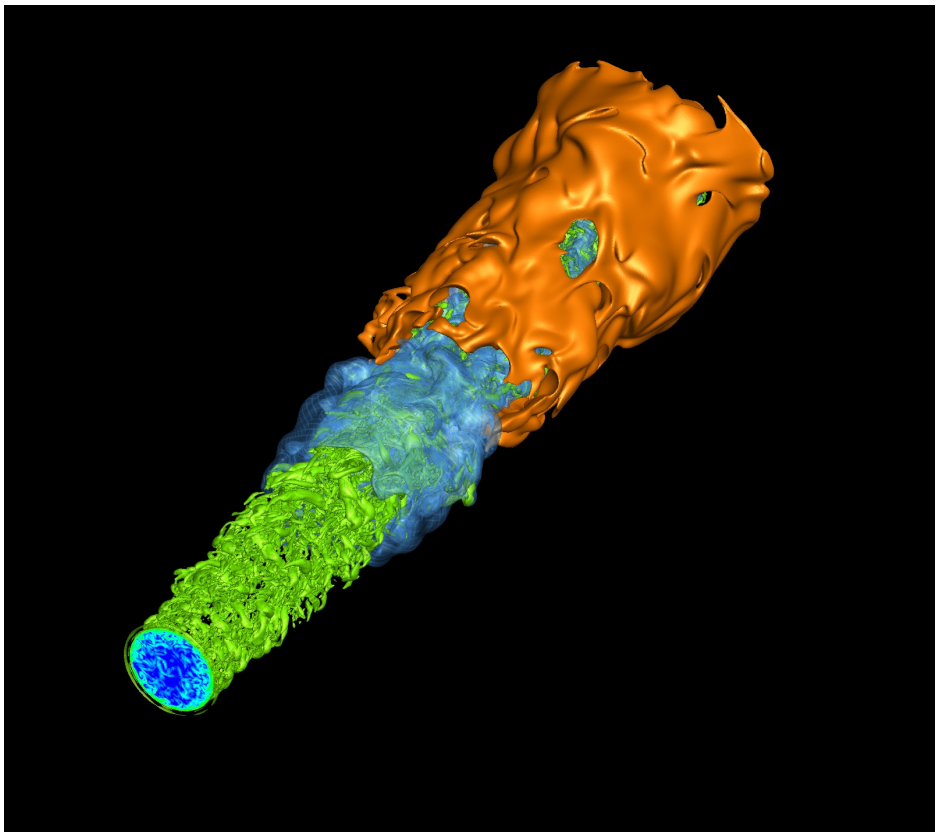

Figure 5.4: 3D Isometric view of a reacting hydrogen jet. The isocontours are (a) Q-criterion in green, (b) HO_2 radical in blue, and (c) Temperature in orange. The inlet plane shows vorticity magnitude contours of the turbulent inflow conditions.

The contours of the fuel and oxidizer in figures 5.6(a) and 5.6(b) show that both get depleted in the combustion zone. However, some of the oxidizer makes its way into the central core of the jet without getting consumed. The fuel, hydrogen, is fully consumed and is not detected on the outer edge of the flame along the coflowing stream. Figure 5.6(c) shows the nitrogen field which is a scalar in this problem, as it does not react with any other species. We see nitrogen evolves exactly like the mixture fraction field, another scalar field. Figure 5.6(d) shows

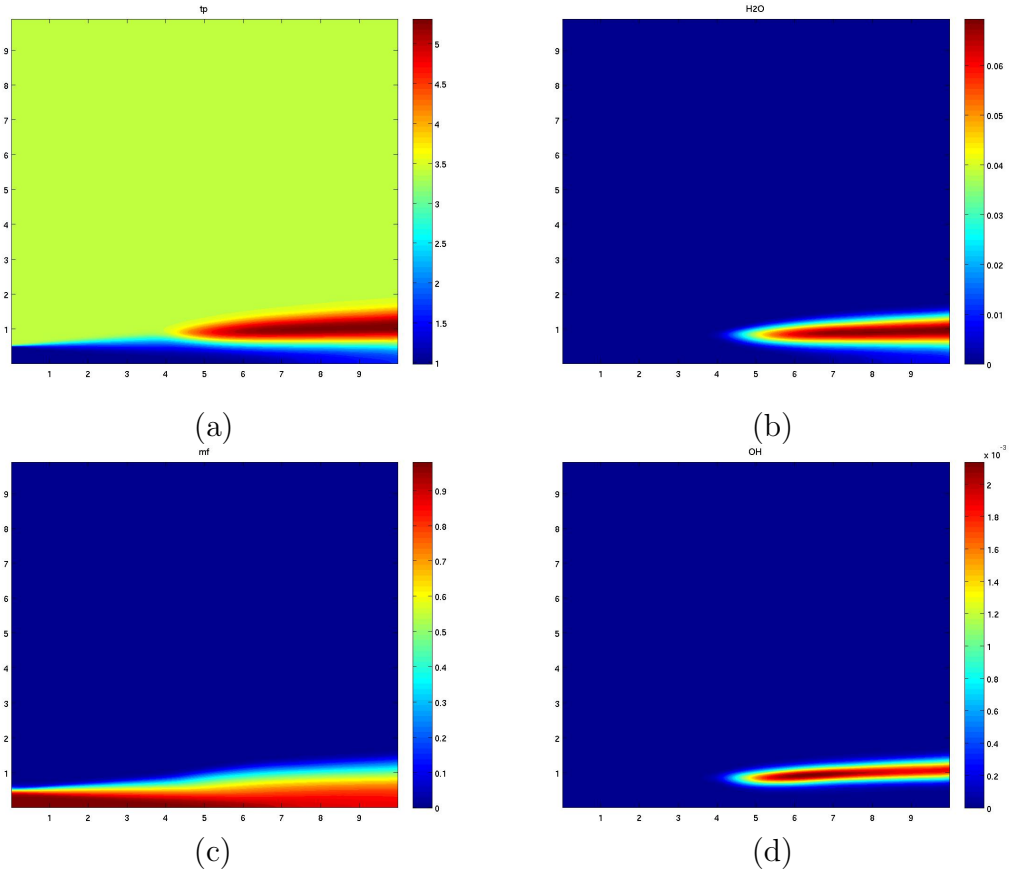

Figure 5.5: Mean profiles for (a) temperature, (b) the primary product H_2O, (c) mixture fraction z and (d) OH radical

the contour of HO_2 radical which is an indicator of hydrogen autoignition. The HO_2 radical starts forming along the jet's shear layer at 3 diameters downstream and peaks ahead of the flame's lifted height. HO_2 combines with H producing two OH radicals which aids in the thermal runaway process leading to the rapid heat release. This process rapidly reduces the HO_2 concentration within the flame but the radical formed ahead of the flame but we also see high concentrations of the radical in the turbulent cold core of the fuel jet. It is likely that the radical is

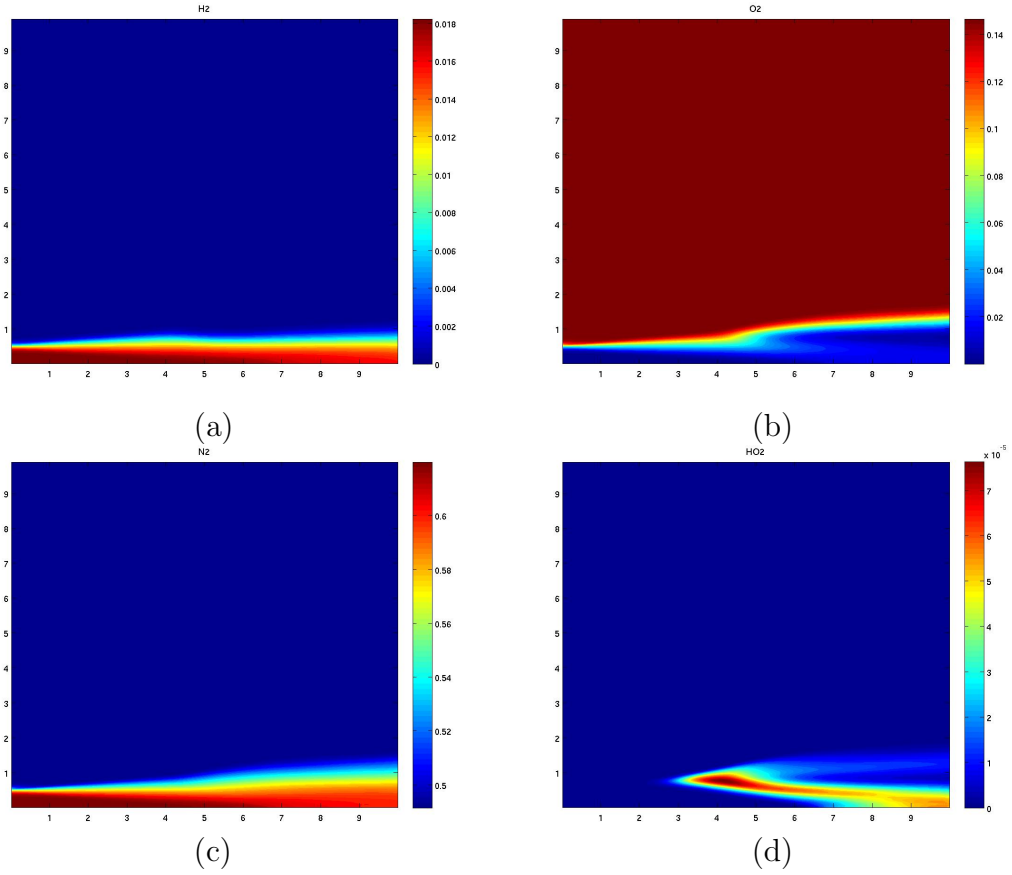

Figure 5.6: Mean profiles for (a) fuel H_2, (b) oxidizer O_2, (c) diluent N_2 (d) HO_2 radical

being advected into the core and is also being created actively at the inner edge of the flame.

In figures 5.7(a) and 5.7(b) we see the high temperature radicals H and O that form along the hot flame. While both radicals peak in concentration at the same location along the shear layer at the ignition point, further downstream we see the O radical shift to the upper edge of the flame and H along the lower edge. At the location of autoignition, the fuel and oxidizer streams have been mixed

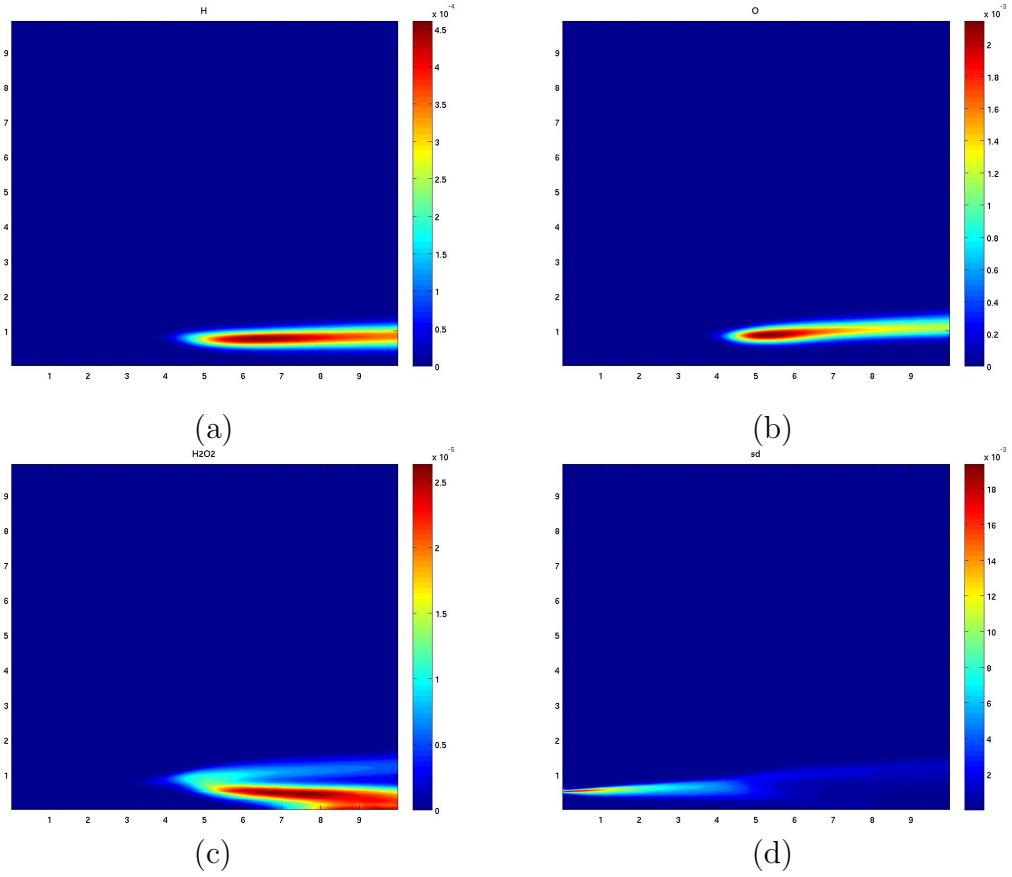

Figure 5.7: Mean profiles of radicals (a) H, (b) O, (c) H_2O_2, and (d) scalar dissipation χ

well by the turbulence in the shear layer but post ignition, the flame takes on the characteristics of a diffusion flame. The diffusion flame is aided by the hot oxidizer from the coflow and cold fuel from the central jet's core. The diverging radicals is indicative of this transition from a homogeneous reaction zone to a diffusion flame like reaction zone. The H_2O_2 radical, hydrogen peroxide, is shown in figure 5.7(c). This is a stable species at low temperature and survives when advected into the cold fuel core. Finally in figure 5.7(d), the scalar dissipation

contours show the high values along the shear layer rapidly fall post ignition. The magnitude of scalar dissipation ahead of the flame is measured at $80s^{-1}$ not high enough to impede with the ignition process [57].

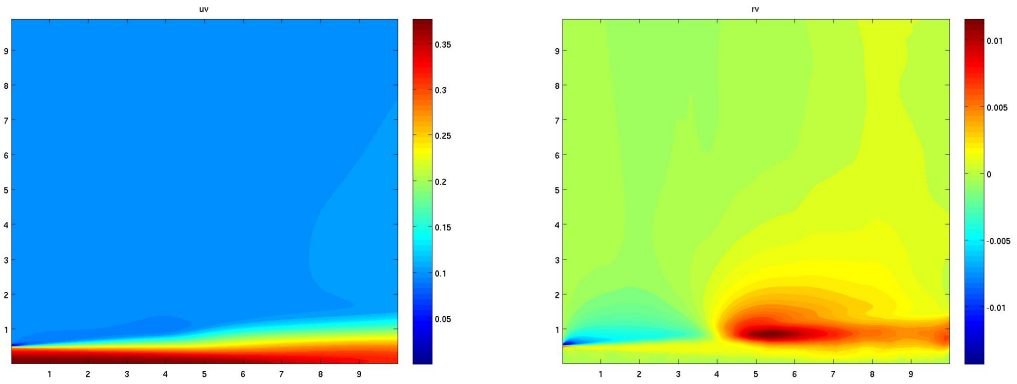

(a) (b)

Figure 5.8: Mean profiles of (a) axial velocity, and (b) radial velocity

The mean velocity field is shown in figures 5.8(a) and 5.8(b). The axial velocity field shows the shear layer expand in thickness similar to the scalar field evolution. The low velocity due to the pipe's lip at the inlet plane is also visible. The radial velocity shows the entrainment of the coflow by the jet before the ignition. Post-ignition, the heat release from the combustion causes divergence. This is shown by the high positive values in the radial velocity field.

In figure 5.9 we can observe the flame ignite and spread in mixture fraction space. Profiles are taken at four downstream locations $x = [4, 5, 6, 7]$. We can clearly see the HO_2 radical peak at very lean mixture fraction pre-ignition at 4 diameters downstream. Post-ignition at 5 diameters, the temperature has increased from that of pure scalar mixing and this is accompanied by positive heat

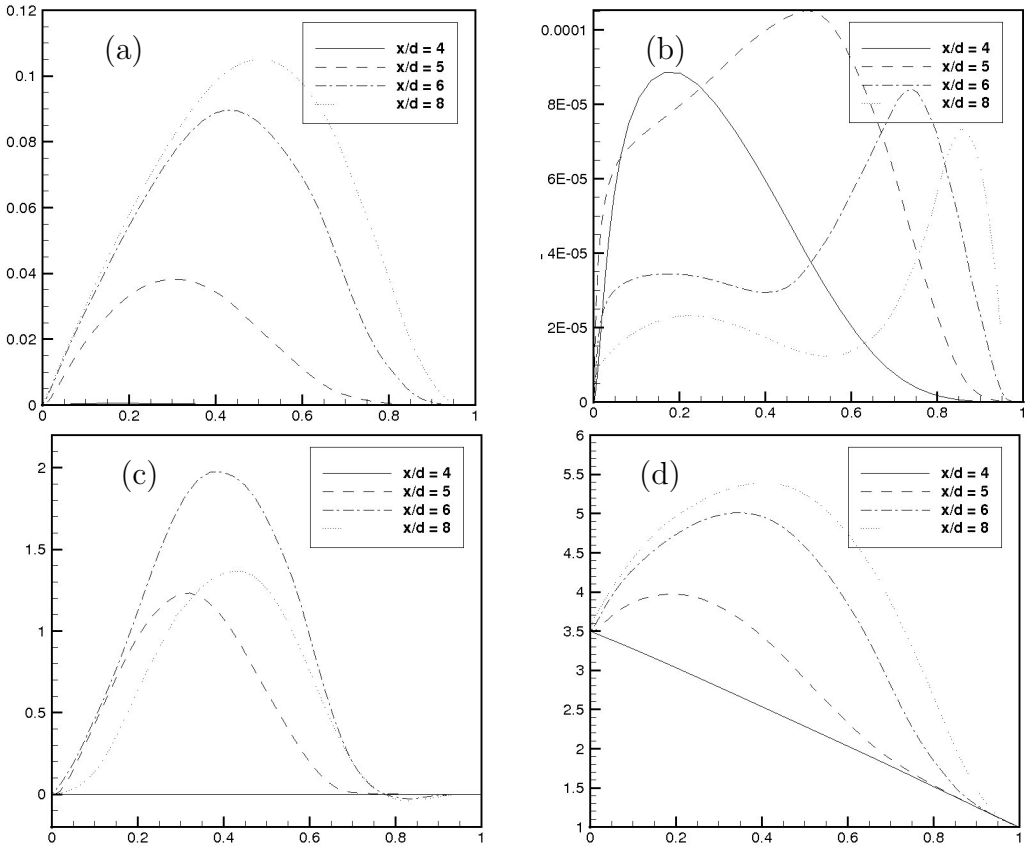

Figure 5.9: Profiles of (a) H_2O mass fraction, (b) HO_2 mass fraction, (c) heat release, and (d) temperature in mixture-fraction space at different axial locations

release and H_2O mass-fractions. As we go downstream, at 6 and 8 diameters, the combustion activity shifts to richer mixture fractions. Note that the heat release increases from 5 to 6 diameters and drops to back to a lower peak at 8 diameters. This is likely a transition of the flame switching from autoignition mode to a diffusion mode. The HO_2 radical drops in concentration post-ignition at lean mixture fractions which have burnt through. At very rich mixture fraction, combustion is incomplete as shown by the lack of heat release and low temperatures

and the radicals survive longer. This behavior is seen in the contour plots as high concentrations of HO_2 in the cold core of the fuel jet.

5.4.2 Flame characteristics

A lifted flame is stabilized by many mechanisms and in an autoignition based stabilization, we expect to find the HO_2 radical form ahead of the flame base. In an inhomogeneous temperature and mixture-fraction field, the most reactive mixture is often very different from the stoichiometric mixture [31]. In the present configuration, the hot coflow aids ignition in the hot lean mixtures and from simple homogeneous reactor simulations, we determine the most-reactive mixture fraction to be 0.06 for the present inlet configuration. The stoichiometric mixture fraction is 0.5 based on the fuel and oxidizer streams. Figures 5.10 (a,b,c) show the mass-fractions of species HO_2 and $H2O$, and temperature overlaid with the two important mixture fraction lines overlaid. We observe that the initial formation of the HO_2 radical is centered along the most-reactive mixture fraction line. While not as evident as HO_2, formation of H_2O and the temperature during ignition are close to the most-reactive mixture fraction line and then move towards the stoichiometric mixture fraction line further downstream. This indicates that ignition happens at the most-reactive mixture fraction and the flame spreads towards the stoichiometric mixture fractions downstream.

The instantaneous contours in figures 5.11(a,b) of HO_2 and temperature shows this behavior more clearly. Autoignition spots always form very close to the most reactive mixture fraction line at 4 to 5 diameters downstream of the inlet. The chemical energy contained at this mixture fraction is low due to the very lean fuel concentrations. The stoichiometric mixture fractions thus show the highest

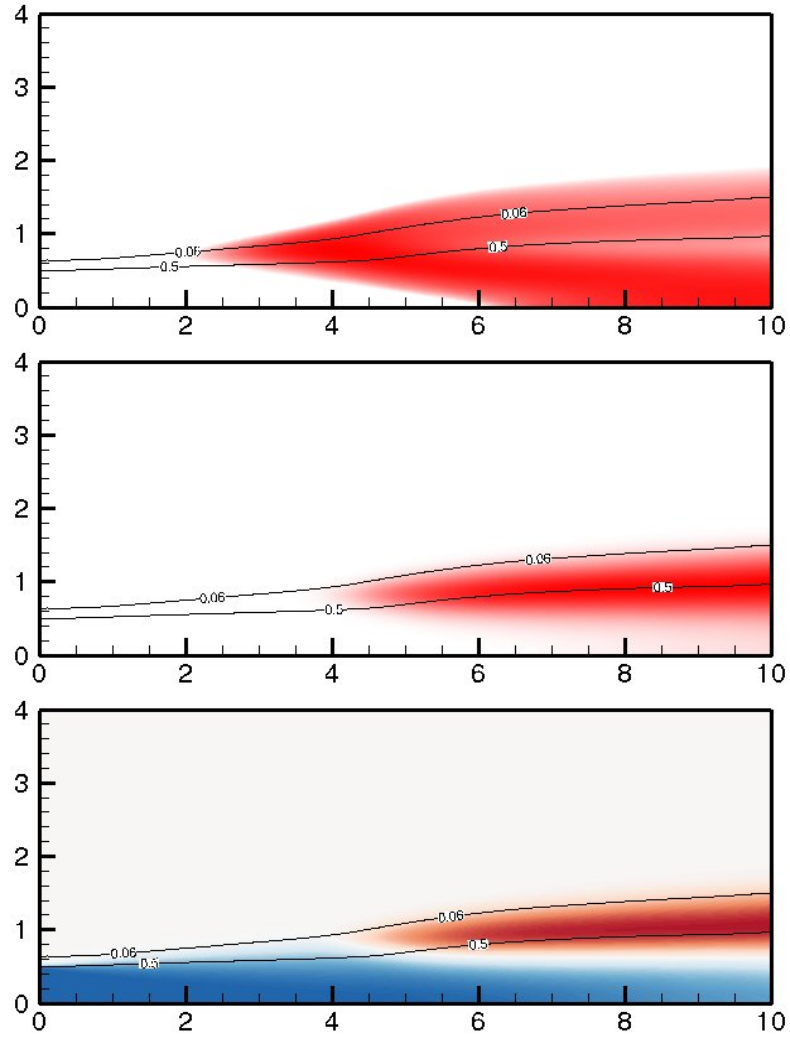

Figure 5.10: Contours of (a) HO_2 mass-fraction in log-scale, (b) H_2O mass-fraction, and (c) temperature, overlaid with the stoichiometric and most-reactive mixture-fraction lines

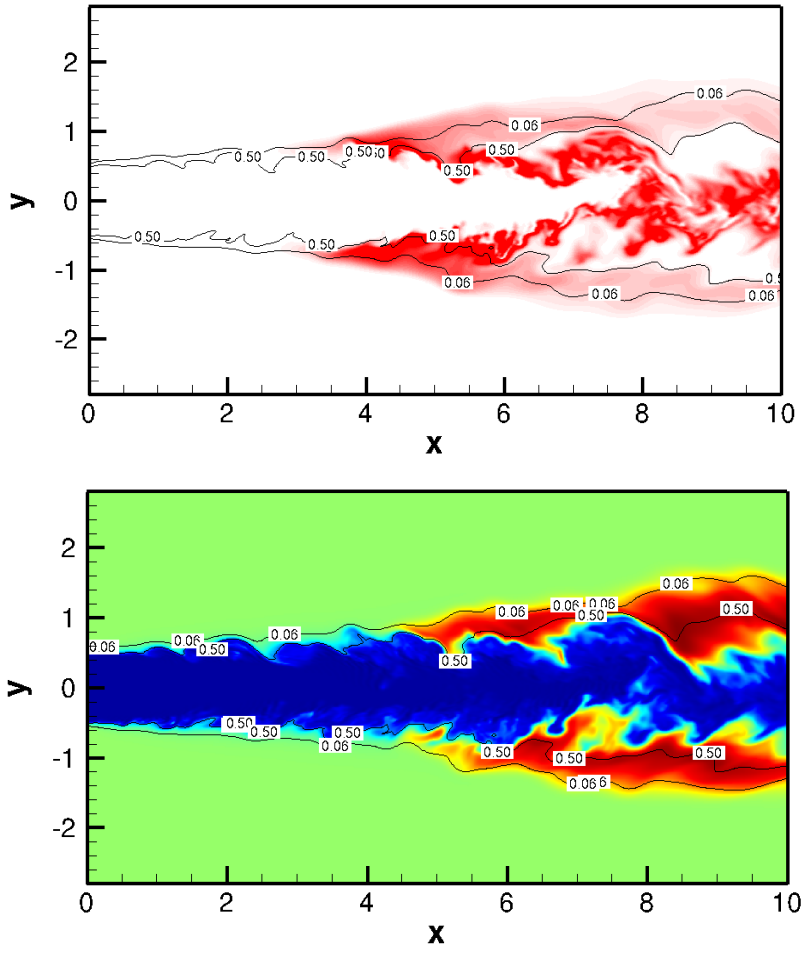

Figure 5.11: Instantaneous contours of (a) HO_2 mass-fraction, and (b) temperature, overlaid with the stoichiometric and most-reactive mixture-fraction lines

temperatures once ignition has taken place and the flame has spread across to richer mixtures. This spreading can be seen more than 6 diameters downstream of the inlet.

5.4.3 Lifted Height

The stabilization and location of a turbulent diffusion flame can be understood as the balance of a turbulent premixed flame propagating against the incoming velocity of the jet's shear layer [52]. Gautam [15] measured the lift-off heights for turbulent diffusion flames for hydrogen and presented a correlation for lift-off height with laminar flame speed and jet exit velocity. This correlation was found to yield a good estimate for the lifted flame in the vitiated coflow burner by Cabra *et al.*[6] who then speculated that autoignition along with a partially premixed flame may play a role in flame stabilization. The lifted height of the turbulent flame in the current DNS is estimated to be approximately 4.5 jet diameters from the radially averaged temperature data. The predicted lift-off height using the correlation however is 26.7 jet diameters which implies that the premixed turbulent flame may not have a role to play in stabilization.

Muniz & Mungal [36] in their experimental study of turbulent diffusion flames noted that stabilization due to premixed turbulent flames occurs at low velocity pockets in the shear and the flame speeds were measured to be less than three times the laminar flame speeds. This would indicate that a turbulent hydrogen flame would need local velocities of $9m/s$ (assuming hydrogen flame speeds of 3 m/s) or less in the flow field to not be blown-off. The coflow velocity in the current study was $41m/s$ and the mean local velocity at the flame stabilization points was close to $49m/s$ which rules out the possibility of a turbulent premixed

flame stabilization.

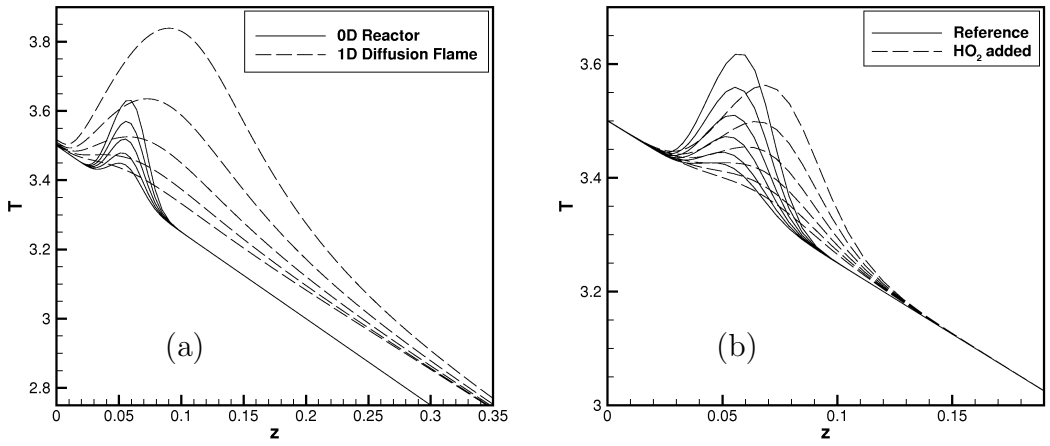

Figure 5.12: Temperature versus mixture-fraction: (a) Ignition for a 0D reactor model (lines correspond to time, $\tau = 45-49$) and a 1D diffusion flame ($\tau = 41-45$) (b) Ignition under the influence of initial $Y(HO_2) = 0.0001$ with $\tau = 22 - 27$

We therefore turn to models that let us correlate ignition delay times with autoignition as the mechanism of stabilization. Figure 5.12(a) shows the ignition of a well-stirred reactor model and a 1D diffusion flame with initial conditions set to the mixing layer at jet inlet conditions. The ignition delays obtained were 46 and 41 D/U time units which multiplied by the advection velocity of at the flame base would correspond to a lifted height of 5.5 and 4.9 diameters from the two models respectively. The ignition times from the two models suggest that the 1D diffusion flame is faster than the 0D model. The 1D flame reaches a temperature of $T = 3.6$ at $\tau = 45$ whereas the 0D model take longer at $\tau = 49$. Not only that but the diffusion flame is also less sensitive to z_{mr} and allows a larger range of mixture fractions centered at z_{mr} to ignite at similar time delays. The

turbulent flame conditions in the DNS may further accelerate the ignition time due to enhanced mixing and therefore explain the lower lift-off height than obtained from the two models. In figure 5.12(b) we see the influence of added HO_2 to a 0D model, which reduces the ignition time-delay to less than half of the original delay. This would indicate that any formation of HO_2 which occurs along the flame and is advected downstream can cause mixtures at the right temperature to rapidly autoignite. Thus the cold core of the jet where we see high concentrations of HO_2 is a location that can cause the rich mixtures to autoignite when heated by the flame.

5.4.4 Flame Index

The flame index is a measure derived to determine the combustion regime from the alignment of the fuel and oxidizer gradients and is defined as follows:

$$FI = \nabla Y_{fuel} \cdot \nabla Y_{oxidizer} \tag{5.1}$$

Positive values of the flame index indicate a premixed flame and negative values indicate a diffusion flame. This measure is referred to as the Takeno flame index [55]. A normalized flame index that varies from -1 to 1 is defined as follows:

$$FI = \frac{\nabla Y_F \cdot \nabla Y_O}{|\nabla Y_F||\nabla Y_O|} \tag{5.2}$$

Note that different normalizations for the flame index have also been chosen, such as those by Mizobuchi *et al.*[33] and Vervisch *et al.*[53]. We will use the normalized flame index as defined above.

The contour plot of the flame index is shown in figure 5.13 where the contour

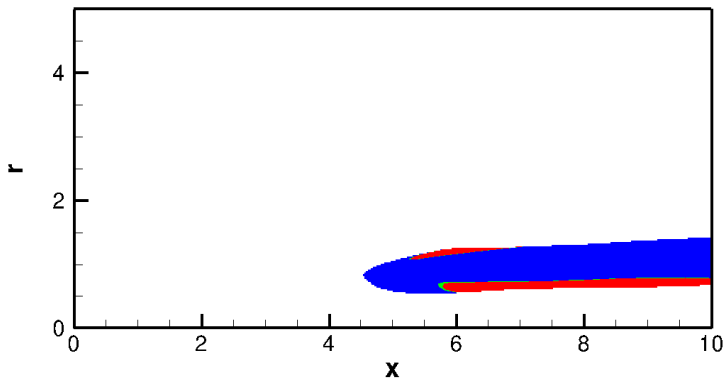

Figure 5.13: Flame index shown as a contour with premixed and diffusion zones

is masked for regions with low heat release and red indicates positive values and blue is negative. The figure shows three regions, a central diffusion mode and two premixed modes. This indicates that combustion on the inner and outer edge can sustain premixed flames, lean on the outer edge which is short lived and rich on the inner edge that is sustained for longer downstream. Autoignition occurs in a region which has primarily opposed gradients. The scatter plot of the normalized flame index vs mixture fraction in figure 5.14 shows that while the flame has two premixed zones, they are barely positive in the flame index. This is indicative of a transient premixed flame and is made clear by the instantaneous plot in figure 5.15. Here we can see the rich premixed flame on the inner edge with wrinkled surface but covers the entire length of the jet's cold core downstream.

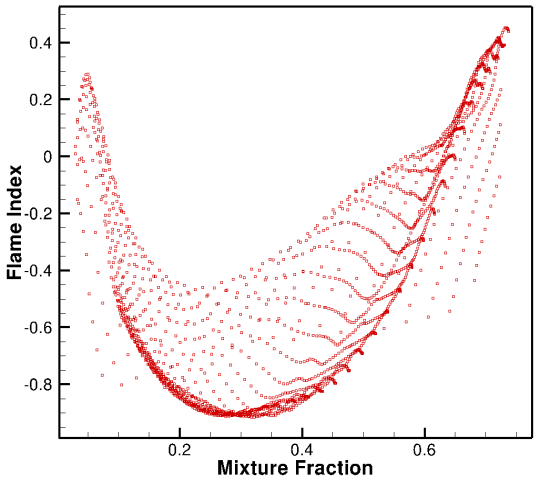

Figure 5.14: Scatter plot of normalized flame index in mixture fraction space

5.4.5 Flame base

While the triple flame is used to explain the mechanics of a laminar diffusion flame, a turbulent diffusion flame does not necessarily have a triple flame like structure and is composed of turbulent premixed and edge flames at the base and turbulent diffusion flame as a tail [36]. The DNS result points to a very similar structure but the stabilization is achieved by autoignition instead of turbulent edge flames. The flame in both cases stabilizes in low velocity zones in the shear layer and post-ignition the heat release causes acceleration of the flow and expansion leading to diverging streamlines.

Taking a closer look at the flame base to observe the effect of an autoignited flame, we plot streamlines in figure 5.16 with a background contour of radial velocities. This figure shows the jet entrain the coflow from the inlet all the way to 4 diameters downstream. The flame located 4.5 diameters downstream makes its strong influence on the coflow from 4 diameters downstream. The heat release

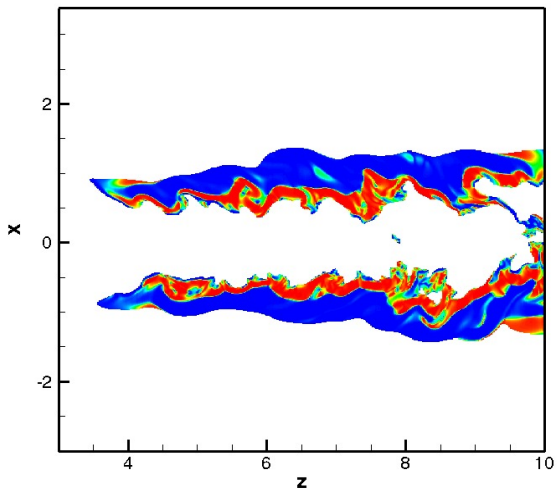

Figure 5.15: Instantaneous contour plot of flame index

from the flame produces a strong divergence causing expansion and pushes the coflow away. This influence is felt on all the scalar fields as seen in the mean plots. The scalar dissipation field is also strongly affected by the divergence field as seen figure 5.17. The H_2O mass-fraction lines indicates the region where the flame is fully burnt. The scalar dissipation values drop significantly as the flame temperature and thus divergence increases. The effect of the divergence is that the turbulence levels inside the flame have dropped as well and this is visible upon closer inspection of the contours in figure 5.11.

We computed the entrainment field as well and plot the mass flux and local entrainment rate in figures 5.18(a) and 5.18(b). The observation is consistent with the lifted flame experiments by Han & Mungal [17]. The local entrainment rate increases with axial distance until the location of the flame base at 4.5 diameters

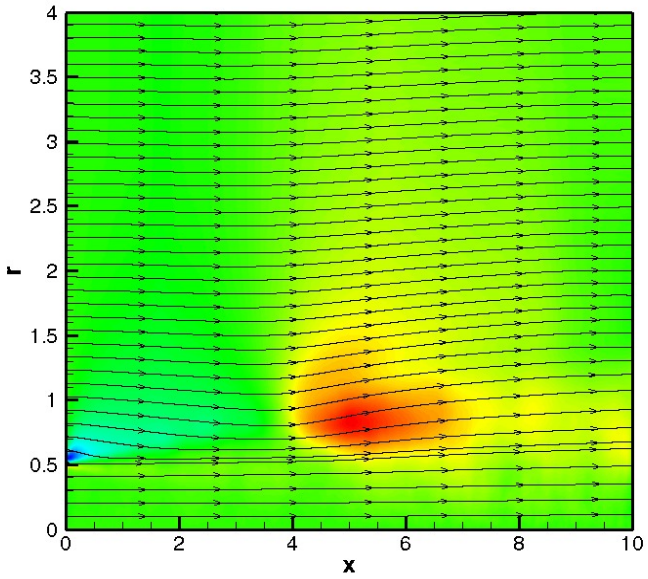

Figure 5.16: Mean radial velocity contour with an overlay of streamlines. Note that X and Y axis are plotted on a 2:1 scale to highlight the curvature of streamlines at the jet's shear layer.

and then decreases thereafter. The mass flux shows an sharp increase in rate from 5 to 6 diameters downstream that is caused by the strong divergence which accelerates the flow. The rate of increase however drops after 8 diameters which is likely the result of decreased entrainment due to the flame.

5.4.6 Scalar field evolution

The scalar field evolution is important from the point of combustion modelling, particularly for the mixture-fraction field. Mean radially averaged data is insufficient especially if the statistical distribution is not Gaussian. In figure 5.19 we

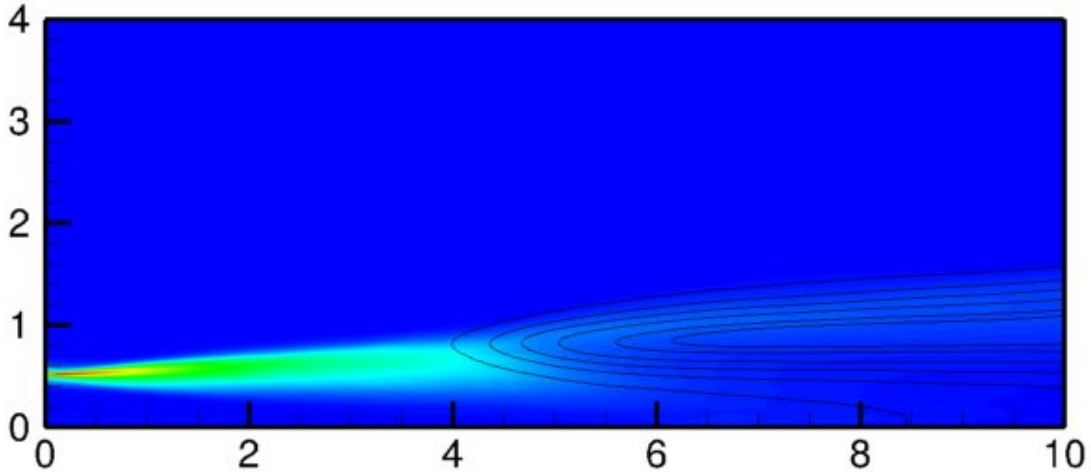

Figure 5.17: Scalar dissipation contour with an overlay of H_2O mass-fraction lines

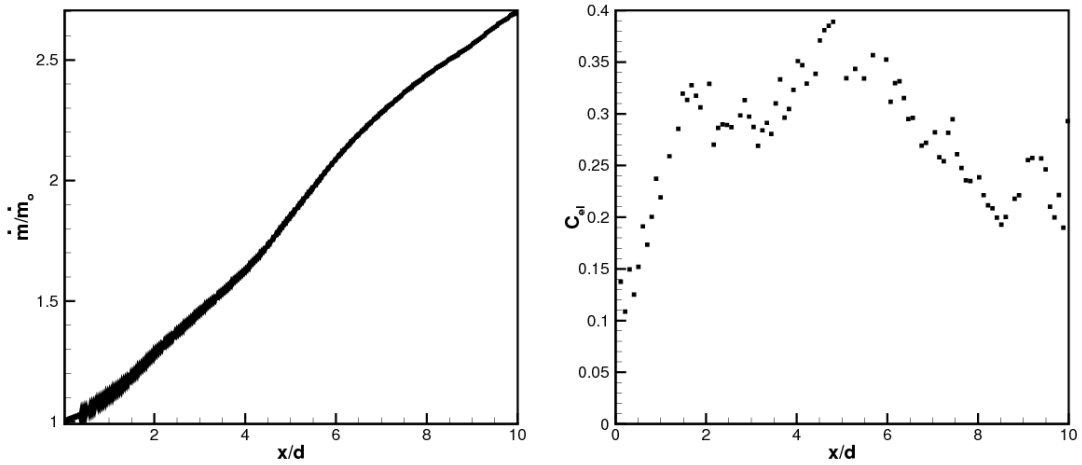

Figure 5.18: (a) Axial mass flux and (b) Local entrainment rate

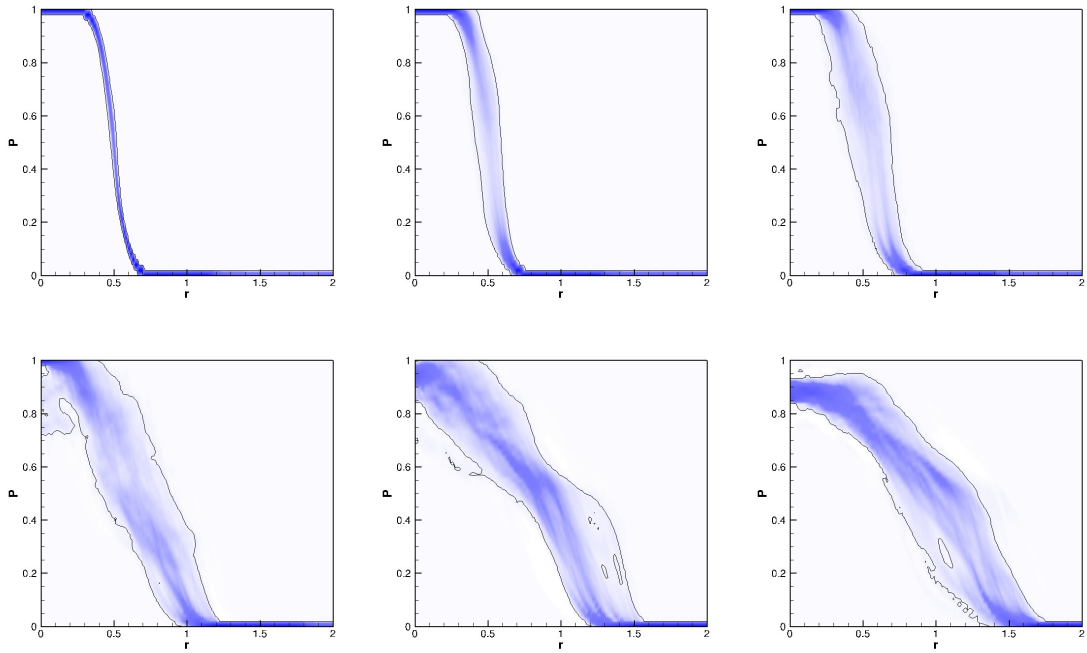

Figure 5.19: Mixture-fraction PDF contours plotted as a function of mixture-fraction vs radial distance from the centerline. Each PDF contour is computed at an axial distance of (a) 0.1, (b) 1, (c) 2, (d) 5, (e) 7, (f) 10 diameters from the inlet

plot the PDFs of mixture fraction z at various axial distances. The y-axis is mixture fraction and values of 1 indicates fuel and 0 oxidizer. The radial variation from fuel to oxidizer is clearly seen in figure 5.19(a) which is close to the inlet conditions. As we move downstream, the turbulent shear layer mixes the fuel and oxidizer thus thickening the PDF distribution in figures 5.19(b,c).

Post-ignition, the distributions as shown in figures 5.19(d,e,f) show a complex picture. All these PDFs show a non-normal distribution. The distributions also expand radially outward reflecting the expansion due to heat release, a feature

that stands out in the PDF taken 7 diameters downstream. At the centerline $r = 0$, we also see a transition from a mixture fraction of 1, indicating pure fuel, to lower values. This is the oxidizer leaking into the core of the fuel jet which we observed in the mean plots of oxygen mass-fraction in figure 5.6(b).

5.5 Statistics from probes

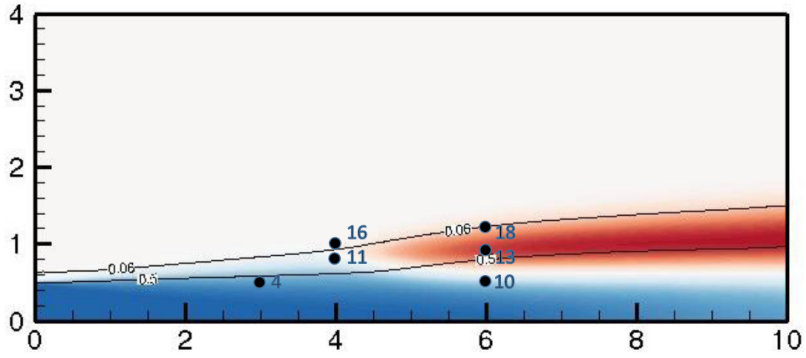

Figure 5.20: Probes located along the flame's stabilization marked by labeled dots overlaid on a contour plot of temperature with mixture-fracture isolines.

Probes allow gathering of more information on a very fine time scale at the expense of losing spatial resolution. 20 probes were placed in the computational domain along the flame. Data is presented from a selected few probes whose locations are shown in figure 5.20. These probes collect close to 50 variables every single iteration.

The location of the probes and the rationale for choosing them are as follows: The first set of probes, probes 1-10, are placed along the jet's shear layer

corresponding to $r = 0.5$ and $x = 1.5$ to $x = 6$ in steps of 0.5. These probes help study the turbulence levels and its effect on fuel-oxidizer mixing. Two more sets of probes are placed along the flame center and the outer edge of the flame. The probes, 11-15, placed along the flame center are located at (r, z) of $(0.8, 4)$, $(0.85, 5)$, $(0.9, 6)$, $(0.95, 7)$ and $(1.0, 8)$. Probes, 16-20, placed along the outer edge of the flame are located at $(1.0, 4)$, $(1.1, 5$, $(1.2, 6)$, $(1.25, 7)$ and $(1.3, 8)$. The probes collected data from $t = 23.4$ to $t = 47.7$ which corresponds to 24.3 non-dimensional time units or 2.4 flow-throughs since the domain is $10D$ long.

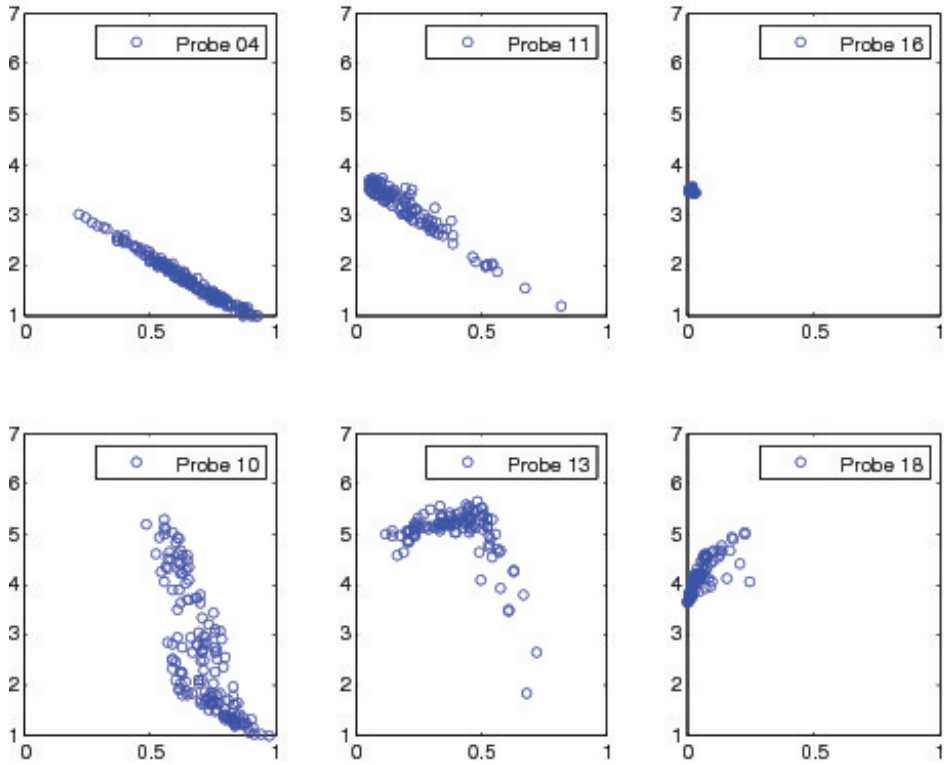

Figure 5.21: Scatter plot of temperature vs mixture fraction at the six probe locations.

In mixture fraction space, we take a look at some of the data collected in

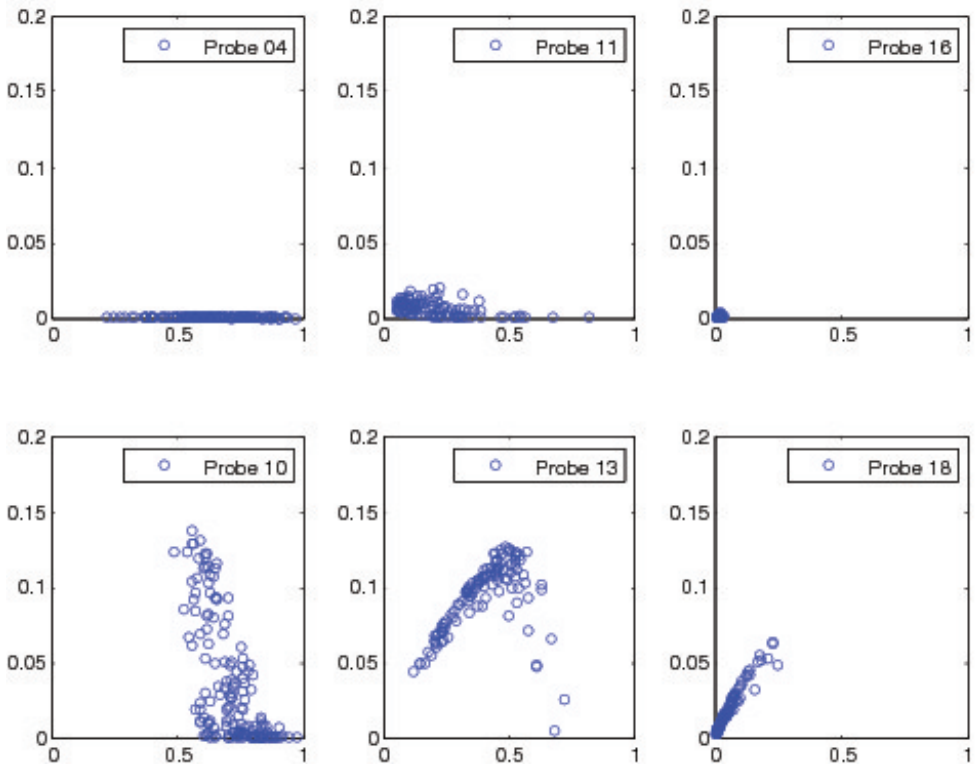

Figure 5.22: Scatter plot of reaction progress $Y_{H_2O}/Y_{H_2O_{max}}$ vs mixture fraction at the six probe locations.

the form of scatter plots. In figures 5.21 and 5.22, temperature and reaction progress (based on Y_{H_2O} normalized by $Y_{H_2O_{max}}$) are plotted against mixture fraction. Probe 4 located upstream of the flame along the shear layer shows a wide range of mixture fractions, from lean to rich, indicating high turbulent mixing and the correspond plot for reaction progress indicates no reactions. Probe 10 which is further downstream along the shear layer shows a primarily fuel rich mixture with varying levels with reaction progress. This location has rich unburnt and partially burning mixtures that indicates a fluttering flame that occasionally impinges at

this location. Probes 11 and 13 are placed along the center of the flame. Probe 11, which was placed close to the flame stabilization point more specifically shows clear signs of autoignition with temperature increase and product formation at the most-reactive mixture fraction where hot lean mixtures ignite first. Probe 13 downstream has an established flame with high temperatures and product formation. The wide range of mixture fractions observed indicates a very turbulent flame which is thick enough that both the outer lean and inner rich edges of the flame pass through this probe location. Finally, probes 16 and 18 were placed along the hot lean flame's outer edge. Probe 16 is close to the flame stabilization point and has mixtures that are hot and almost pure oxidizer with very little fuel concentration and the product formation is correspondingly minimal. Probe 18 downstream indicates a fully burning hot lean flame with high product formation. The reduced scatter in mixture fraction indicates very lean conditions at this location.

The turbulent kinetic energy (TKE) defined as $k = (1/2)(\overline{u'^2} + \overline{v'^2} + \overline{w'^2})$ is at the same probes is shown in figures 5.23 and 5.24 as a function of mixture fraction and temperature respectively. The data shows that the turbulence levels are drasctically different across the probes. Since the inflow consists of a turbulent pipe and a laminar coflow, the flow downstream will be determined by which stream is advected over the probe in addition to the effects of turbulence being generated by the jet's shear layer and reduced by the expansion from the flame's divergence. The probes, 4 and 10, placed along the jet's shear layer have the most turbulent intensities and the highest scatter, indicating mixing of the turbulent jet with the laminar coflow. Probe 10 does not have as high intensities as probe 4 which is likely due to the flame's development downstream. At the center of the

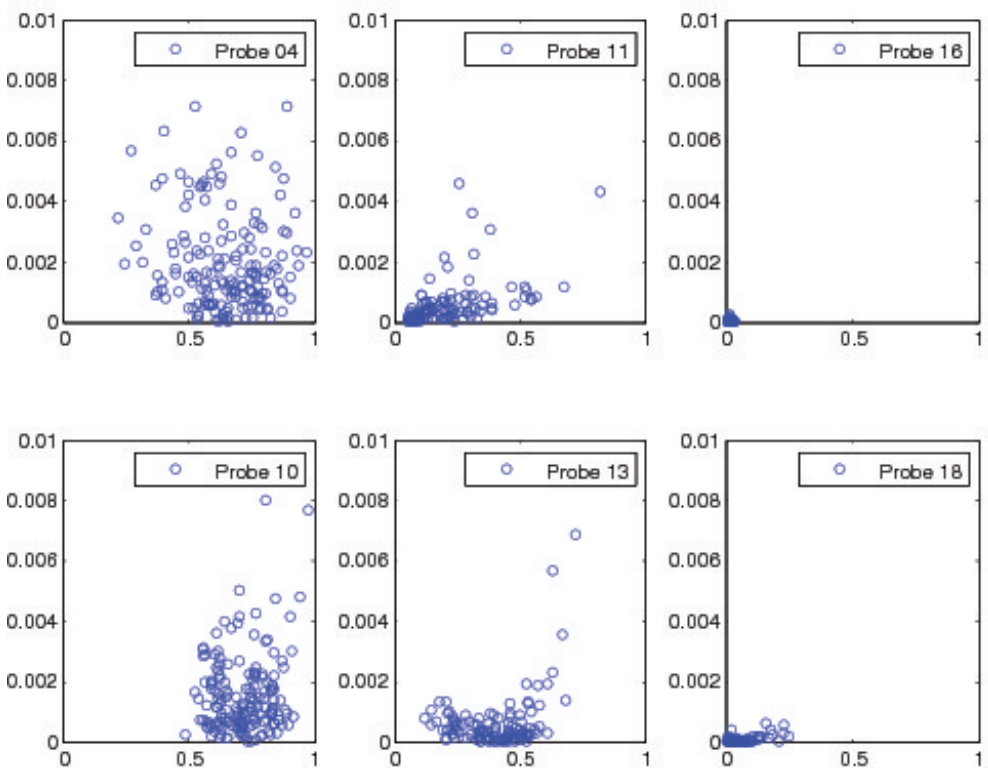

Figure 5.23: Scatter plot of TKE vs mixture fraction at the six probe locations.

flame, probes 11 and 13 show lower TKE overall. The spots with high intensities correspond to cold rich mixtures that were advected from the interior of the jet. This data shows an important characteristic of the flame, that the autoignition spot and flame stabilization point at probe 11 experiences very low turbulence levels compared to the interior of the turbulent jet. Probes 16 and 18 and the outer edge of the flame show a very quiescent flow field with hardly any turbulence. Probe 18 in particular which is further downstream does not seem to see much turbulence from the jet. The flame effectively acts as a damper on the turbulent jet from spreading radially outward any further.

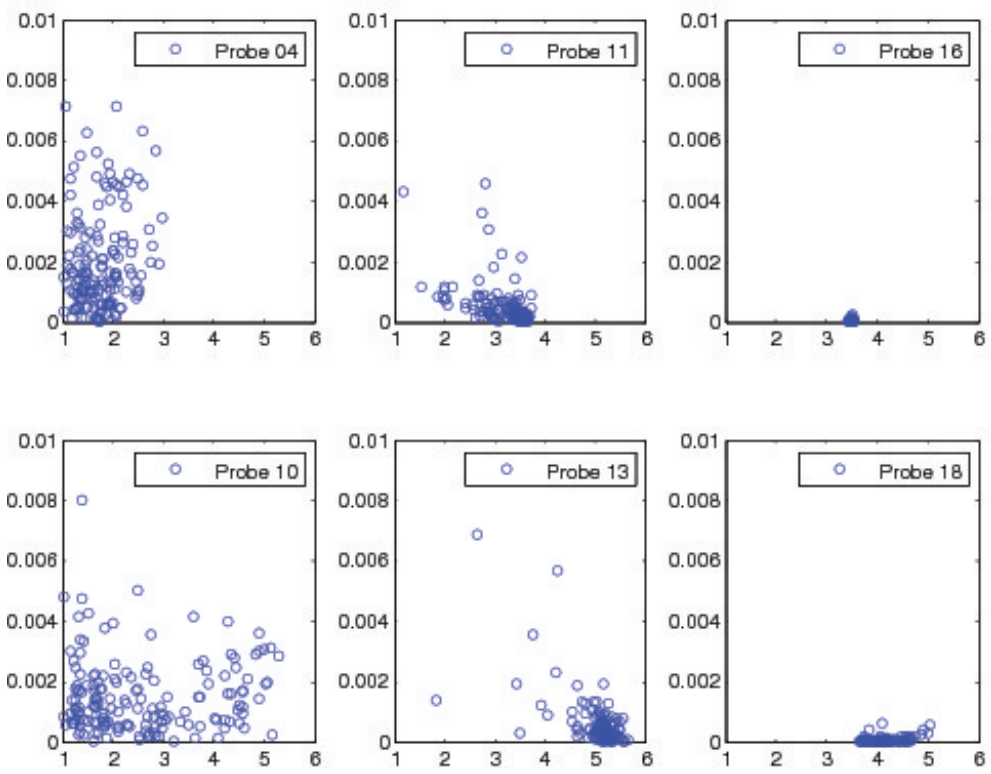

Figure 5.24: Scatter plot of TKE vs Temperature at the six probe locations.

The power spectral density (PSD) of turbulent kinetic energy (TKE) derived from data collected at probes 4, 10, 11, 13, 16, and 18 are shown in figure 5.25. The frequency is non-dimensionalized with respect to the inertial time scale D_{jet}/U_{jet}. The unit of frequency can be expressed as U/D. The data corroborates our observation with the scatter plots. The turbulence levels at probes 4 and 10, placed along the jet's shear layer, in general are higher than the probes placed along the center of the flame. The probes at the outer edge of the flame show the least amount of turbulence. Contrasting probes upstream and downstream of each other lets us analyze the evolution of the turbulence spectrum. Probe 10 shows

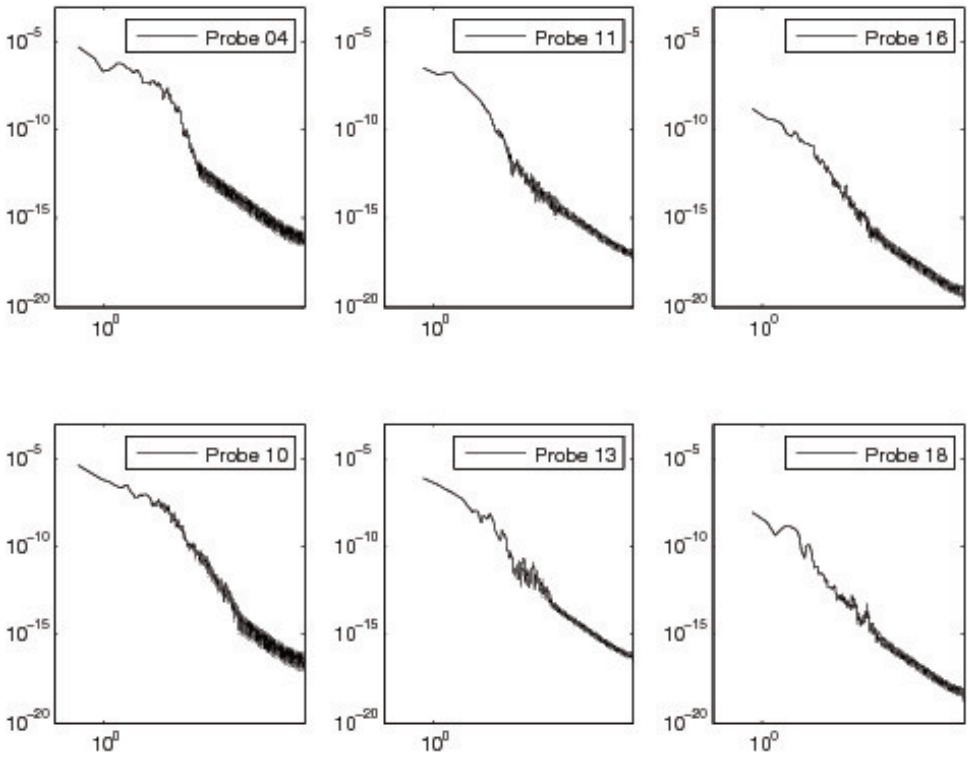

Figure 5.25: PSD of turbulent kinetic energy at the six probe locations.

development of the small scale turbulence that didn't exist at probe 4, especially between frequencies of 50 and 500. Between probes 11 and 13, there is a small increase in the turbulence levels between frequencies 10 and 100 which is likely due to mixing from the jet. The probes placed at the outer edge, 16 and 18, show very low turbulence levels to begin with, but probe 18 which is downstream seems to show an increase in low frequency mode at 2 U/D which might be a remnant of the shear layer instability. It also shows a small peak at a higher frequency of 100.

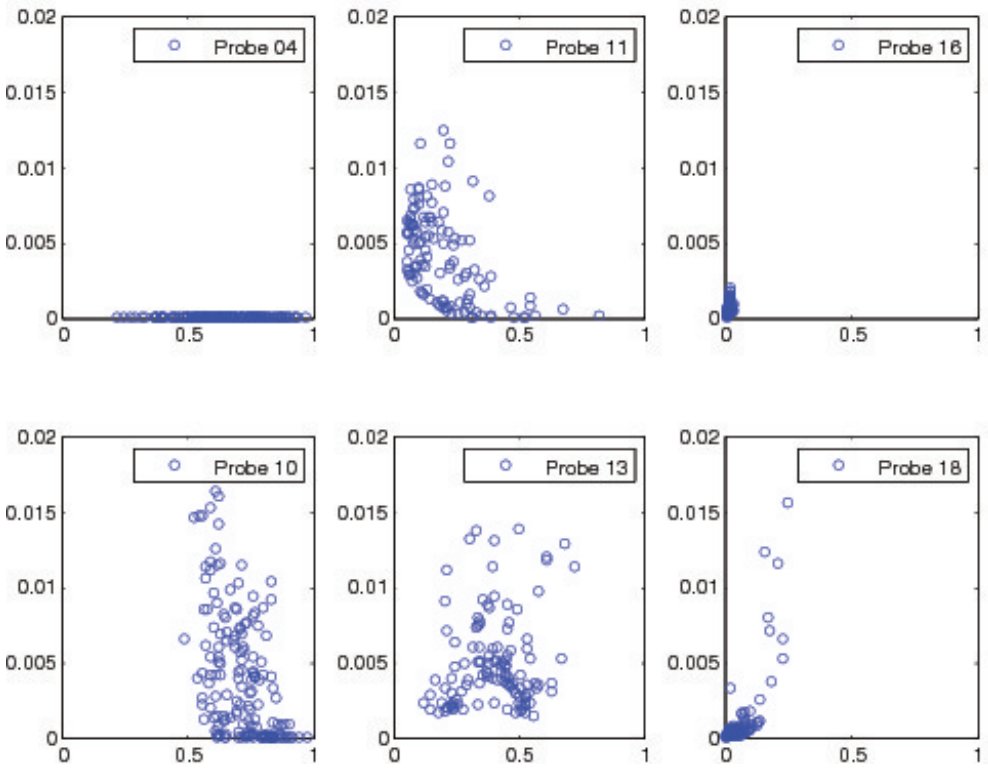

Figure 5.26: Reaction rate from reaction r9 which produces HO_2.

From the reaction kinetics collected at the probes, we look at the production and consumption of one of the key species in hydrogen autoignition, the hydroperoxyl radical HO_2. Figures 5.26 and 5.27 show the production from reaction r9: $H + O2 + M = HO2 + M$ and consumption due to reaction r11: $HO2 + H = OH + OH$ from the six probes. The data from the probes show once again the process of hydrogen autoigntion taking place at the flame stabilization zone with probe 11 showing high production of the HO_2 radical at the hot lean conditions, which correspond to the most-reactive mixture fraction. The higher consumption levels indicate that the flame's thermal runaway is already

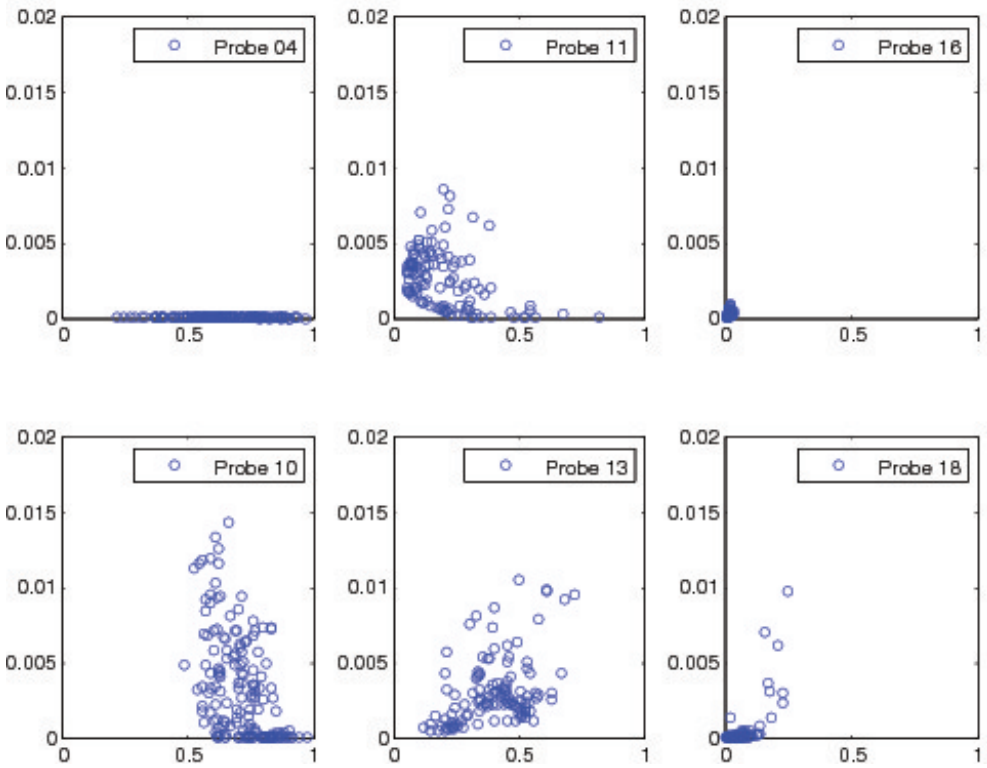

Figure 5.27: Reaction rate from reaction r11 which consumes HO_2.

taking place producing a rich pool of the hydroxyl radical OH, which defines the flame's most reactive zone. Probe 13 shows that all mixture fractions are highly reactive and the flame is established. Probe 4 shows little production and probe 10 downstream has high production at rich fuel mixtures that are hot enough to react. The temperatures are low enough to sustain high concentrations of the HO_2 radical. Probes 13 and 18 indicate minimal combustion and the very hot and lean conditions here are very different from the rest of the flame. This zone is calm with very little turbulence and the burning produces little heat due to the lean mixture.

Chapter 6

Conclusion

An algorithm to solve compressible chemically reacting flows with an explicit predictor for transport terms and iterative implicit corrector for the reaction source terms is presented. The colocated variables have allowed this method to be suitable for structured and unstructured finite volume implementations. The solver features non-reflecting boundary conditions, Chemkin compatible chemical mechanisms and exhibits good parallel scalability. Validation of the iterative corrector for reaction terms was shown with the well-stirred reactor for hydrogen-air and methane-air chemistries. Two-dimensional lifted jets with hydrogen, methane and ethylene were simulated and thin flame fronts in the case of hydrocarbons were observed.

The algorithm was extended to address the center point singularity due to a cylindrical grid by a novel cell merging method which is conservative and well suited to finite volume formulations. This was coupled with an implicit direct line solver in the radial direction to allow grid clustering at the jet shear layer.

A three dimensional simulation of a round turbulent autoignited flame at a

Reynolds number of $10,000$ was performed and the flame was characterized. A fully developed pipe flow simulation was used to specify the inflow conditions of the fuel jet. HO_2 radicals were found to form ahead of the flame base indicating autoignition as the stabilization mechanism. The radicals were also observed on the inner edge of the flame brush indicating autoignition kernel formation downstream of the stabilization point. Ignition was also observed in hot and lean conditions in accordance with the most reactive mixture fraction whereas the flame index indicates that the flame is composed of diffusion and premixed modes. A small region of lean-premixed flame was observed on the outer edge of the flame stabilization point and the inner edge of the flame is composed of a rich-premixed flame.

The flame stabilization is explained by autoignition and not by leading edge flames as in the case of a lifted turbulent diffusion flame. The ignition delay times obtained from both the well-stirred reactor and a one-dimensional unsteady unstrained diffusion flame explain the lift-off height well. The diffusion flame model also points to a larger range of mixture fractions close to z_{mr} that can ignite and this would make flame stabilization by autoignition more robust to fluctuations in mixture-fraction. Transport of HO_2 radical and oxygen from the coflow along the inner edge of the flame brush is observed which likely contribute to enhanced burning or creation of autoignition spots further downstream.

References

[1] K. Akselvoll and P. Moin. An efficient method for temporal integration of the Navier–Stokes equations in confined axisymmetric geometries. *Journal of Computational Physics*, 125(2):454–463, 1996.

[2] R. Asaithambi, S. Muppidi, and K. Mahesh. A numerical method for DNS of turbulent reacting flows using complex chemistry. *AIAA paper*, 2012.

[3] P. C. Babu and K. Mahesh. Upstream entrainment in numerical simulations of spatially evolving round jets. *Physics of Fluids*, 16(10):3699–3705, 2004.

[4] B. J. Boersma, G. Brethouwer, and F. T. M. Nieuwstadt. A numerical investigation on the effect of the inflow conditions on the self-similar region of a round jet. *Physics of Fluids*, 10(4):899–909, 1998.

[5] C. Bogey and C. Bailly. Turbulence and energy budget in a self-preserving round jet: direct evaluation using large eddy simulation. *Journal of Fluid Mechanics*, 627:129–160, 2009.

[6] R. Cabra, T. Myhrvold, J. Y. Chen, R. W. Dibble, A. N. Karpetis, and R. S. Barlow. Simultaneous laser raman-rayleigh-lif measurements and numerical

modeling results of a lifted turbulent H_2/N_2 jet flame in a vitiated coflow. *Proceedings of the Combustion Institute*, 29:1881–1888, 2002.

[7] G. S. Constantinescu and S. Lele. A highly accurate technique for the treatment of flow equations at the polar axis in cylindrical coordinates using series expansions. *Journal of Computational Physics*, 183(1):165–186, 2002.

[8] B. B. Dally, A. N. Karpetis, and R. S. Barlow. Structure of turbulent nonpremixed jet flames in hot dilute coflow. *Proceedings of the Combustion Institute*, 29:1147–1154, 2002.

[9] J. M. J. den Toonder and F. T. M. Nieuwstadt. Reynolds number effects in a turbulent pipe flow for low to moderate re. *Physics of Fluids*, 9(11):3398–3409, 1997.

[10] J. Doom, Y. Hou, and K. Mahesh. A numerical method for DNS/LES of turbulent reacting flows. *Journal of Computational Physics*, 226(1):1136 – 1151, 2007.

[11] J. Doom and K. Mahesh. Direct numerical simulation of auto-ignition of a hydrogen vortex ring reacting with hot air. *Combustion and Flame*, 156(4):813 – 825, 2009.

[12] J. Doom and K. Mahesh. Dns of auto-ignition in turbulent diffusion H_2/air flames. *AIAA paper*, 2009.

[13] J. G. M. Eggels, F. Unger, M. H. Weiss, J. Westerweel, R. J. Adrian, R. Friedrich, and F. T. M. Nieuwstadt. Fully developed turbulent pipe flow:

a comparison between direct numerical simulation and experiment. *Journal of Fluid Mechanics*, 268:175–210, 1994.

[14] J. Freund, S. Lele, and P. Moin. Direct simulation of a supersonic round turbulent shear layer. *AIAA paper*, pages 97–0760, 1997.

[15] T. Gautam. Lift-off heights and visible lengths of vertical turbulent jet diffusion flames in still air. *Combustion Science and Technology*, 41(1-2), 1984.

[16] M. D. Griffin, E. Jones, and J. D. Anderson. A computational fluid dynamic technique valid at the centerline for non-axisymmetric problems in cylindrical coordinates. *Journal of Computational Physics*, 30(3):352–360, 1979.

[17] D. Han and M. Mungal. Direct measurement of entrainment in reacting/nonreacting turbulent jets. *Combustion and flame*, 124(3):370–386, 2001.

[18] E. R. Hawkes and J. H. Chen. Direct numerical simulation of hydrogen-enriched lean premixed methane-air flames. *Combustion and Flame*, 138:242–258, 2004.

[19] O. Herbinet, W. J. Pitz, and C. K. Westbrook. Detailed chemical kinetic mechanism for the oxidation of biodiesel fuels blend surrogate. *Combustion and Flame*, 157(5):893 – 908, 2010.

[20] R. Hixon, S.-H. Shih, and R. Mankbadi. Numerical treatment of cylindrical coordinate centerline singularities. *International Journal of Computational Fluid Dynamics*, 15(3):251–263, 2001.

[21] H. J. Hussein, S. P. Capp, and W. K. George. Velocity measurements in a high-reynolds-number, momentum-conserving, axisymmetric, turbulent jet. *Journal of Fluid Mechanics*, 258:31–75, 1994.

[22] M. Ihme and Y. C. See. Prediction of autoignition in a lifted methane/air flame using an unsteady flamelet/progress variable model. *Combustion and Flame*, 157(10):1850–1862, 2010.

[23] S. Lam and D. Goussis. Understanding complex chemical kinetics with computational singular perturbation. In *Symposium (International) on Combustion*, volume 22, pages 931–941. Elsevier, 1989.

[24] T. Lu and C. K. Law. A directed relation graph method for mechanism reduction. *Proceedings of the Combustion Institute*, 30(1):1333–1341, 2005.

[25] U. Maas and S. B. Pope. Simplifying chemical kinetics: intrinsic low-dimensional manifolds in composition space. *Combustion and flame*, 88(3):239–264, 1992.

[26] K. Mahesh, G. Constantinescu, S. Apte, G. Iaccarino, F. Ham, and P. Moin. Large-eddy simulation of reacting turbulent flows in complex geometries. *Journal of applied mechanics*, 73(3):374–381, 2006.

[27] K. Mahesh, G. Constantinescu, and P. Moin. A numerical method for large-eddy simulation in complex geometries. *Journal of Computational Physics*, 197(1):215–240, 2004.

[28] C. Markides and E. Mastorakos. An experimental study of hydrogen autoignition in a turbulent co-flow of heated air. *Proceedings of the Combustion Institute*, 30(1):883–891, 2005.

[29] C. N. Markides. http://www2.eng.cam.ac.uk/∼cnm24/mixing.htm.

[30] E. Mastorakos. Ignition of turbulent non-premixed flames. *Progress in Energy and Combustion Science*, 35(1):57 – 97, 2009.

[31] E. Mastorakos, T. Baritaud, and T. Poinsot. Numerical simulations of autoignition in turbulent mixing flows. *Combustion and Flame*, 109(12):198 – 223, 1997.

[32] E. Mastorakos, C. Markides, and Y. M. Wright. Hydrogen autoignition in a turbulent duct flow: Experiments and modelling. *Conference on Modelling Fluid Flow*, 2003.

[33] Y. Mizobuchi, S. Tachibana, J. Shinio, S. Ogawa, and T. Takeno. A numerical analysis of the structure of a turbulent hydrogen jet lifted flame. *Proceedings of the Combustion Institute*, 29(2):2009–2015, 2002.

[34] K. Mohseni and T. Colonius. Numerical treatment of polar coordinate singularities. *Journal of Computational Physics*, 157(2):787–795, 2000.

[35] M. A. Mueller, T. Kim, R. A. Yetter, and F. L. Dryer. Flow reactor studies and kinetic modeling of the H_2/O_2 reaction. *International Journal of Chemical Kinetics*, 31:113–125, 1999.

[36] L. Muniz and M. Mungal. Instantaneous flame-stabilization velocities in lifted-jet diffusion flames. *Combustion and Flame*, 111(1):16–31, 1997.

[37] E. Oldenhof, M. Tummers, E. van Veen, and D. Roekaerts. Ignition kernel formation and lift-off behaviour of jet-in-hot-coflow flames. *Combustion and Flame*, 157(6):1167 – 1178, 2010.

[38] N. R. Panchapakesan and J. L. Lumley. Turbulence measurements in axisymmetric jets of air and helium. part 1. air jet. *Journal of Fluid Mechanics*, 246:197–223, 1 1993.

[39] N. Park and K. Mahesh. Numerical and modeling issues in les of compressible turbulent flows on unstructured grids. *AIAA paper*, 2007.

[40] N. Peters. Laminar diffusion flamelet models in non-premixed turbulent combustion. *Progress in energy and combustion science*, 10(3):319–339, 1984.

[41] C. D. Pierce. *Progress-Variable approach for Large-Eddy Simulation of Turbulent Combustion*. PhD thesis, Stanford University, june 2001.

[42] C. D. Pierce and P. Moin. Progress-variable approach for large-eddy simulation of non-premixed turbulent combustion. *Journal of Fluid Mechanics*, 504(1):73–97, 2004.

[43] H. Pitsch, M. Chen, and N. Peters. Unsteady flamelet modeling of turbulent hydrogen-air diffusion flames. In *Symposium (international) on combustion*, volume 27, pages 1057–1064. Elsevier, 1998.

[44] H. Pitsch and N. Peters. A consistent flamelet formulation for non-premixed combustion considering differential diffusion effects. *Combustion and Flame*, 114(1):26–40, 1998.

[45] T. J. Poinsot and S. K. Lele. Boundary conditions for direct simulations of compressible viscous flows. *Journal of Computational Physics*, 101:104–129, 1992.

[46] S. B. Pope. Computationally efficient implementation of combustion chemistry using in situ adaptive tabulation. *Combustion Theory and Modelling*, 1(1):41–63, 1997.

[47] S. B. Pope. *Turbulent flows*. Cambridge university press, 2000.

[48] R. Sankaran, E. Hawkes, J. Chen, T. Lu, and C. Law. Structure of a spatially developing turbulent lean methane air bunsen flame. *Proceedings of the Combustion Institute*, pages 1291–1298, 2007.

[49] G. P. Smith, D. M. Golden, M. Frenklach, N. W. Moriarty, B. Eiteneer, M. Goldenberg, C. T. Bowman, R. K. Hanson, S. Song, W. C. Gardiner, V. V. L. Jr., and Z. Qin. *http://www.me.berkeley.edu/gri_mech/*. 2000.

[50] J. C. Sutherland and C. A. Kennedy. Improved boundary conditions for viscous, reacting, compressible flows. *Journal of Computational Physics*, 191(2):502–524, 2003.

[51] J. A. van Oijen and L. P. H. de Goey. Modelling of premixed laminar flames using flamelet-generated manifolds. *Combustion Science and Technology*, 161(1):113–137, 2000.

[52] L. Vanquickenborne and A. Van Tiggelen. The stabilization mechanism of lifted diffusion flames. *Combustion and Flame*, 10(1):59–69, 1966.

[53] L. Vervisch, R. Hauguel, P. Domingo, and M. Rullaud. Three facets of turbulent combustion modelling: DNS of premixed V-flame, LES of lifted non-premixed flame and RANS of jet-flame. *Journal of Turbulence*, page N4, 2004.

[54] H. Wang. Personal communication, 2012.

[55] H. Yamashita, M. Shimada, and T. Takeno. A numerical study on flame stability at the transition point of jet diffusion flames. In *Symposium (International) on Combustion*, volume 26, pages 27–34. Elsevier, 1996.

[56] M. Yokokawa, K. Itakura, A. Uno, T. Ishihara, and Y. Kaneda. 16.4-Tflops direct numerical simulation of turbulence by a Fourier spectral method on the Earth Simulator. In *Supercomputing, ACM/IEEE 2002 Conference*, pages 50–50. IEEE, 2002.

[57] C. S. Yoo, R. Sankaran, and J. H. Chen. Three-dimensional direct numerical simulation of a turbulent lifted hydrogen jet flame in heated coflow: flame stabilization and structure. *Journal of Fluid Mechanics*, 640:453–481, 2009.

Appendix A

A Tabulation based Combustion Model

A.1 Introduction

Direct numerical simulation of turbulent flames was impractical for all but a few problems a decade ago but this has been changing rapidly ever since with increasing computing power. So, while DNS and LES can now be described as the state-of-the-art methods in numerically studying turbulent flames, these simulations are still very expensive when it comes to practical applications. The cost is two-fold. The first reason is due to the high Reynolds numbers of flows which is an imposing challenge even in the case of non-reacting flows. The range of length scales that need to be captured increases with the Reynolds number as $O(Re^{9/4})$ and the cost of time integration can go up by $O(Re^{3/4})$ due to the Courant number limitation [47]. The second reason and the one that is relevant to this chapter is the cost of computing the transport and chemical reactions of the fuel, oxidizer and products.

Solving the governing equations with an implicit method with a detailed chemical mechanism for methane combustion like GRI-Mech 3.0 with 53 species and 325 reactions implies that the cost of computing transport equations goes up from $O(5^3)$ to $O(4+53)^3$ while the cost of computing the reaction source terms is proportional to the number of reactions. The reactions however introduce their own time scales and resolving all the time scales, in addition to the flow's inertial and acoustic time scales, typically results in a very stiff system. Direct simulations can therefore quickly become infeasible for complex real-world fuels like gasoline and bio-diesel surrogates [19] with thousands of species and reactions. Hence, a wide range of approaches to reduce the cost of combustion are taken, with most of the methods reducing the size of detailed mechanisms into smaller "skeletal" and "reduced" mechanisms, or create species and reaction subspaces:

- Global Reaction Mechanisms with a small selected set of species and reactions
- QSSA (Quasi steady-state assumption) and Partial Equilibrium assumptions
- DRG (Directed Relation Graphs) by Lu & Law [24]
- CSP (Computational Singular Perturbation) by Lam & Goussis [23]
- ILDM (Intrinsic Low Dimensional Manifold) by Maas & Pope [25]

While reduced mechanisms can dramatically cut the number of species and reactions, tabulation based methods eliminate all species and reaction and replace them with one or more transported scalars and a multi-parameter look-up table. Flamelet models [40] fall under this category and highly popular owing to their

low cost. The steady laminar flamelet model has since been extended to include differential diffusion [44], a progress-variable [42], unsteady effects [43, 22] and combined with ideas from ILDM to produce Flamelet-Generated Manifolds [51].

In LES of turbulent reacting flows, the filtered chemical source term needs to be modelled in addition to the accurately computing the unfiltered chemical source terms. Transported PDF (Probability density function) and CMC (Conditional moment closure) models solve the complete set of species as a joint probability and conditional mass fractions respectively and tend to be computationally expensive. LES models that use a combination of presumed PDFs and flamelets to address subgrid-scale mixing and combustion have been used to study a wide range of problems. Examples include the flamelet progress-variable approach of [42] that has been applied to a gas turbine combustor by [26]. ISAT (In situ Adaptive Tabulation) was developed by Pope [46] which tabulates the process of integrating the chemical source terms in a PDF method.

A.1.1 Flamelet based models

Under the laminar diffusion flamelet assumption a turbulent flame is assumed to be composed of thin flamelets whose simplified governing equations in mixture-fraction space are written as follows:

$$\rho\frac{\partial Y_k}{\partial t} = \frac{1}{2}\rho\chi\frac{\partial^2 Y_k}{\partial z^2} + \dot{\omega}_k \tag{A.1}$$

$$\rho\frac{\partial T}{\partial t} = \frac{1}{2}\rho\chi\frac{\partial^2 T}{\partial z^2} + \dot{\omega}_T \tag{A.2}$$

where the scalar dissipation rate χ is given by

$$\chi = 2D \left(\frac{\partial z}{\partial x_i} \right)^2 \tag{A.3}$$

These one-dimensional equations are solved to steady state and the solutions tabulated, parametrized by the scalar dissipation rate at the stoichiometric mixture fraction χ_{st}. The boundary conditions in z are prescribed to be that of inlet conditions of the fuel at one end and the oxidizer on the other. This is the approach used in the traditional steady laminar flamelet model and a single transport equation for the mixture-fraction is solved:

$$\frac{\partial \rho z}{\partial t} + \frac{\partial \rho z u_j}{\partial x_j} = \frac{1}{ReSc_z} \frac{\partial}{\partial x_j} \left(\mu \frac{\partial z}{\partial x_j} \right) \tag{A.4}$$

The low-Mach equations for momentum and energy are solved to obtain the flow field. The flamelet libraries provide closure in the form of tabulated density, temperature and mass fractions as a function of z and χ_{st}.

The steady model, which lacks the ability to capture phenomena like ignition and finite spread rates, tends to mispredict flame standoff distances. Unsteady models have been proposed which include another transport equation for a progress variable, often defined as a sum of product mass-fractions. Thus the composition space represented by the mass fractions Y_k is now approximated by two variables, mixture-fraction z which is a normalized fuel to oxidizer ratio and a progress variable c that indicates reaction progress (from unburnt to burnt). The transport equation for progress variable is written as follows and note that this

equation contains a source term:

$$\frac{\partial \rho c}{\partial t} + \frac{\partial \rho c u_j}{\partial x_j} = \frac{1}{ReSc_c}\frac{\partial}{\partial x_j}\left(\mu \frac{\partial c}{\partial x_j}\right) + \dot{\omega}_c \tag{A.5}$$

Pierce & Moin [42] have shown their flamelet progress-variable model to be able to capture the flame stand-off distance, mean mixture-fraction profiles and product concentrations in a coaxial combustor better than the steady flamelet model.

Recently, motivated by engine technologies like homogeneous charge compression ignition (HCCI) and exhaust gas recirculation (EGR), canonical flames such as the vitiated coflow burners of Cabra *et al.*[6] and Mastorakos *et al.*[32] have been designed and experimentally studied. Here, the central fuel jet, which is cold at room temperature, ignites as it mixes with the coflowing hot oxidizer. The lifted turbulent flame in such a configuration has been shown to be autoignition-stabilized by Yoo *et al.*[57] and it is important that a combustion model to study this flow is inherently unsteady. Ihme & See [22] proposed an unsteady flamelet progress-variable model to specifically capture autoignition and applied it to this configuration with good agreement with the experiments, and predicted the lift-off height much better than the steady flamelet model.

The flamelet approach is quite popular due to its simplicity and computational cost-effectiveness, however, it still has its drawbacks. The flamelet assumption can break down when there are premixed pockets in the flame and studies such as Yoo *et al.*[57] and Ihme & See [22] have autoignition occurring only in the non-premixed regime. Mastorakos [30] notes that flamelets cannot address

flame-spreading along constant mixture-fraction isosurfaces and modelling of fluctuations in scalar dissipation is lacking. The method is also inapplicable when dealing with premixed or stratified flames. Models that address premixed flames such as flame surface density models and the G-equation model cannot be used for non-premixed flames.

We are proposing a new tabulation based model that can be applied to all flames ranging from fully premixed to non-premixed by tabulating source terms directly instead of flamelets and therefore taking into account the finite rate characteristics of real flames.

A.2 Model algorithm

Keeping the model cost-effective requires us to keep the number of variables to represent the species to a bare minimum. We are assuming that solving the mixture fraction and progress variable equations (A.14, A.15) to represent the compositional space is sufficient. The source term $\dot{\omega}_c$ is unknown and a combustion model must provide closure for this term and the corresponding heat source term $\dot{\omega}_T$ in the energy equation:

$$\frac{\partial \rho E}{\partial t} + \frac{\partial}{\partial x_j}\left(\rho E + p\right) u_j = \frac{1}{Re}\frac{\partial \tau_{ij} u_i}{\partial x_j} + \frac{1}{\gamma_r M_r^2 Re Pr}\frac{\partial}{\partial x_j}\left(\mu c_p \frac{\partial T}{\partial x_j}\right) + \dot{\omega}_T \quad \text{(A.6)}$$

Without making the one-dimensional laminar flamelet assumption for the generation of a library, we can instead solve the temporal ordinary differential equation with a varying set of initial conditions and map the solution onto the mixture-fraction and progress-variable space. This amounts to the tabulation of the source

terms, $\dot{\omega}_c$ and $\dot{\omega}_T$, as a function of mixture-fraction, progress-variable and temperature.

$$\frac{\partial \rho Y_k}{\partial t} = \dot{\omega}_k(Y_k, T, t) \Longrightarrow \dot{\omega}_c(z, c, T) \tag{A.7}$$

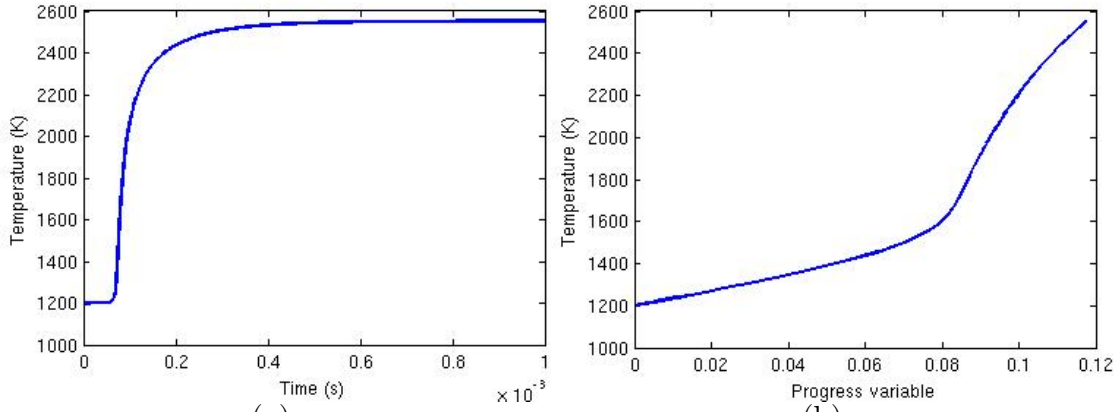

Figure A.1: A temporal solution for a given initial temperature T_0 and mixture-fraction z is shown in (a) Temperature versus time. Mapping time to progress-variable c gives (b) Temperature vs progress-variable, which is then tabulated as $T(T_0, z, c)$.

This approach of tabulating the source term has a distinct advantage when the diffusion flamelet assumption breaks down. The generality allows us to use this tabulation for premixed, non-premixed and stratified flames with no changes to the model or tabulation. In figure A.1 a single temporal solution is shown for a mixture of hydrogen and air with an initial temperature of $1200K$ and a mixture-fraction of 0.4. This solution is mapped from time to progress-variable and stored in a library. Varying initial mixture fraction and temperature leads to a three-dimensional lookup table as shown in figure A.2.

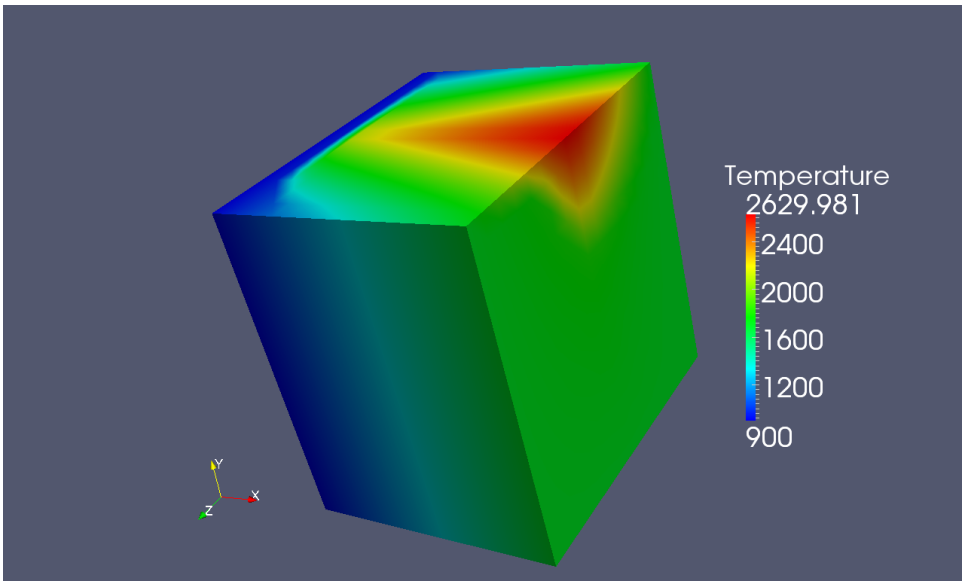

Figure A.2: Visualization of the three dimensional library in temperature. Initial temperature increases in the x-axis, progress-variable in y-axis and mixture-fraction in the z-axis.

The model is expected to capture unsteady phenomena such as : (i) ignition, (ii) extinction, (iii) reignition, as well as (iv) flame spreading (premixed and non-premixed, i.e., along and across mixture-fraction isosurfaces) and we therefore choose our test problems to highlight some of these features.

A priori tests of 0-D (transient) and 1-D combustion problems compared with direct numerical simulation results help in validation of the model. Solving transient problems, like in figure A.3, lets us evaluate the process of building the library and reading from the library. The factors involved in building the library is deciding the resolution requirement in the z, c and T_0 axes and the very definition of c. The progress-variable definition needs to be chosen such that this

quantity increases monotonously. The lack of this property can lead of multi-valued look-ups from the library. Reading from the library is also affected by the quality of interpolation used. With ignition, changes in the species concentrations and temperature are often exponential and a linear interpolant can be highly inaccurate. With a coarse resolution of the library, the lookup process can be cheap but inaccurate and hence a balance needs to be struck that can offer reasonable speed and accuracy.

One-dimensional problems such an unsteady unstrained laminar diffusion flames and premixed flames serve to test the effects of advection and diffusion on the model and can be easily compared with direct simulations, which are computationally cheap in one-dimensional problems. The results of jets in two and three dimensional geometries with detailed chemistry can be performed as an a posteriori analysis, followed by a large eddy simulation comparison with experimental results from laboratory-scale flames.

In addition to the proposed model, we are interested in studying the physics of autoignition in flames and use the knowledge to improve the combustion model. In Asaithambi *et al.*[2], we take a look at autoignition of two-dimensional jets and were able to observe similarities in the stabilization mechanism with the three-dimensional slot jet simulations of Yoo *et al.*[57]. With a large eddy simulation, the experimental results of Cabra *et al.*[6] and Mastorakos *et al.*[32] can serve as the benchmark to model.

A.3 Numerical method

The governing equations for the DNS formulation for density, mixture fraction, progress variable, momentum and energy are as follows:

$$\frac{\partial \rho}{\partial t} + \frac{\partial \rho u_j}{\partial x_j} = 0 \tag{A.8}$$

$$\frac{\partial \rho z}{\partial t} + \frac{\partial \rho z u_j}{\partial x_j} = \frac{1}{ReSc_z}\frac{\partial}{\partial x_j}\left(\mu \frac{\partial z}{\partial x_j}\right) \tag{A.9}$$

$$\frac{\partial \rho c}{\partial t} + \frac{\partial \rho c u_j}{\partial x_j} = \frac{1}{ReSc_c}\frac{\partial}{\partial x_j}\left(\mu \frac{\partial c}{\partial x_j}\right) + \dot{\omega}_c \tag{A.10}$$

$$\frac{\partial g_i}{\partial t} + \frac{\partial g_i u_j}{\partial x_j} = -\frac{\partial p}{\partial x_j} + \frac{\partial \sigma_{ij}}{\partial x_j} \tag{A.11}$$

$$\frac{\partial \rho E}{\partial t} + \frac{\partial}{\partial x_j}\left(\rho E + p\right) u_j = \frac{1}{Re}\frac{\partial \tau_{ij} u_i}{\partial x_j} + \frac{1}{\gamma_r M_r^2 RePr}\frac{\partial}{\partial x_j}\left(\mu c_p \frac{\partial T}{\partial x_j}\right) + \dot{\omega}_T \tag{A.12}$$

A direct numerical simulation with detailed chemistry solves all of the species transport equations whereas with the combustion model, only mixture-fraction and progress-variable need to be solved. The source terms in the progress-variable and energy equation are obtained from the source term library visualized in figure A.2.

The algorithm can be extended to include a large-eddy simulation model, the filtered equations for which can be written as follows:

$$\frac{\partial \bar{\rho}}{\partial t} + \frac{\partial \bar{\rho} \widetilde{u_j}}{\partial x_j} = 0 \tag{A.13}$$

$$\frac{\partial \bar{\rho}\widetilde{z}}{\partial t} + \frac{\partial \bar{\rho}\widetilde{z}\widetilde{u_j}}{\partial x_j} = \frac{\partial}{\partial x_j}\left(\bar{\rho}\widetilde{\alpha}\frac{\partial \widetilde{z}}{\partial x_j} + q_j^z\right) \tag{A.14}$$

$$\frac{\partial \bar{\rho}\widetilde{c}}{\partial t} + \frac{\partial \bar{\rho}\widetilde{c}\widetilde{u_j}}{\partial x_j} = \frac{\partial}{\partial x_j}\left(\bar{\rho}\widetilde{\alpha}\frac{\partial \widetilde{c}}{\partial x_j} + q_j^c\right) + \widetilde{\dot{\omega}_c} \tag{A.15}$$

$$\frac{\partial \bar{g}_i}{\partial t} + \frac{\partial \bar{g}_i\widetilde{u_j}}{\partial x_j} = -\frac{\partial \bar{p}}{\partial x_j} + \frac{\partial}{\partial x_j}\left(\widetilde{\sigma_{ij}} + \tau_{ij}\right) \tag{A.16}$$

$$\frac{\partial \bar{\rho}\widetilde{E}}{\partial t} + \frac{\partial}{\partial x_j}\left(\bar{\rho}\widetilde{E} + \bar{p}\right)\widetilde{u_j} = \frac{\partial \widetilde{\sigma_{ij}}\widetilde{u_i}}{\partial x_j} + \frac{\partial}{\partial x_j}\left(\bar{\kappa}\frac{\partial T}{\partial x_j} + q_j^E\right) + \widetilde{\dot{\omega}_T} \tag{A.17}$$

The subgrid scale stress term τ_{ij} is modelled as

$$\tau_{ij} = 2\mu_t\widetilde{S_{ij}} - \frac{1}{3}\tau_{kk}\delta_{ij} \tag{A.18}$$

where $\mu_t = \bar{\rho}C_s\Delta^2|\widetilde{S}|$ is the turbulent viscosity and the constant C_s is determined dynamically using the Germano identity. The isotropic part of the subgrid stress terms which is related to the subgrid scale kinetic energy, k, as $2\bar{\rho}k = \tau_k k$ is determined from Yoshizhawa's model as:

$$\tau_{kk} = 2\bar{\rho}C_I\Delta^2|\widetilde{S}|^2 \tag{A.19}$$

The subgrid scale flux terms for heat and scalars are modelled using the gradient assumption.

$$q_j^X = \bar{\rho}(\widetilde{u_j}\widetilde{X} - \widetilde{u_j X}) = \frac{\mu_t}{Pr_t^X}\frac{\partial \widetilde{X}}{\partial x_j}, \quad X = \{E, z, c\} \tag{A.20}$$

The turbulent Prandtl number (Schmidt number for scalars) is also determined dynamically and the scalar variance is modelled similarly as $\bar{\rho}X''^2 = \bar{\rho}C_X\Delta^2|\nabla\widetilde{X}|^2$.

The filtered source terms are obtained from integrating eq. A.21 and using the presumed PDF approach to resolve the joint PDF, $\widetilde{P}(z,c,T)$. It is assumed $\widetilde{P}(z,c,T) = \widetilde{P}(z)\widetilde{P}(c)\widetilde{P}(T)$ is reasonable, where $\widetilde{P}(z)$ and $\widetilde{P}(c)$ can be modelled as a beta PDF and $\widetilde{P}(T)$ as a delta function.

$$\widetilde{\dot{\omega}_c} = \int \dot{\omega}_c(z,c,T)\widetilde{P}(z,c,T)dzdcdT \tag{A.21}$$

A finite volume colocated algorithm described in Chapter 2 is used to solve the transport equations. An explicit second order Adams-Bashforth time advancement is performed for the advection and diffusion terms.

A.4 Results & Discussion

A.4.1 Homogeneous reactor

A homogeneous mixture of fuel and oxidizer at an initial temperature of $1200K$ is simulated as a function of time. Figure A.3 shows the comparison between a DNS result with detailed chemistry and the combustion model. Since the tabulation is built from different homogeneous igniting mixtures, this test should match the DNS results well. Any differences in the comparison would stem from the resolution of the tabulation.

A.4.2 Reaction-Diffusion

Results from simulations of a one-dimensional reaction-diffusion system is presented here. The initial conditions for the mixture fraction and temperature, as shown in table A.1, are specifically chosen to test three combustion scenarios that current flamelet based models cannot address with a single library: a premixed

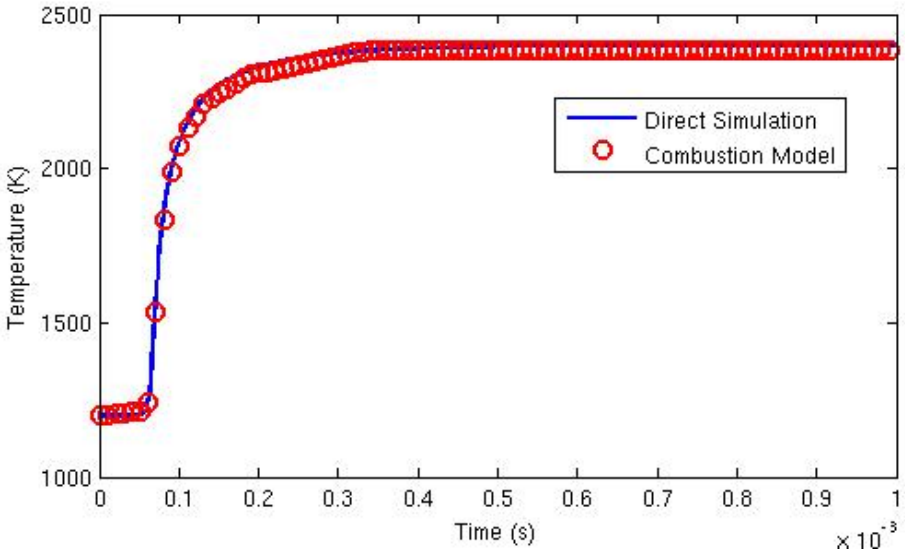

Figure A.3: Comparison of a direct simulation and the combustion model for a homogeneous reactor.

flame, a diffusion flame with ignition at stoichiometric mixture-fraction and finally a diffusion flame with ignition at the most reactive mixture-fraction.

z	T	Combustion mode
0.3	$[1-4]$	Premixed
$[1-0]$	4	Diffusion (ζ_{st})
$[1-0]$	$[1-4]$	Diffusion (ζ_{MR})

Table A.1: Reaction-diffusion test cases.

For the premixed case, the mixture-fraction is constant throughout the domain. A flamelet model based on a non-premixed opposed diffusion flame for tabulation will not capture this mode. In figure A.4, the mixture fraction is held constant and the temperature is a hyperbolic tangent function set to 1 on the left boundary and 4 on the right. A non-dimensional temperature of 1 is equal to 298K. The mixture

consists of hydrogen-air diluted with nitrogen and the composition chosen such that $z = 0.3$. For this initial condition, we observe that the right half autoignites due to the high temperature and a premixed flame-front is formed that propagates towards the colder mixture on the left as seen in the evolution of the progress-variable. The effect of diffusion is strong in this simulation and the flame is in the process of getting extinguished and cannot sustain itself.

In figure A.5, the mixture fraction is varied from 1 on the left boundary to 0 on the right whereas the temperature is set to a constant value of 4. This is an example of an unsteady unstrained diffusion flame. In this case we observe that the autoignition occurs close to the stoichiometric mixture fraction and a diffusion flame spreads outward into rich and lean mixtures. While an unsteady flamelet progress-variable (UFPV) model can be used to simulate this case, it will need a new tabulation if the boundary conditions for the temperature are changed.

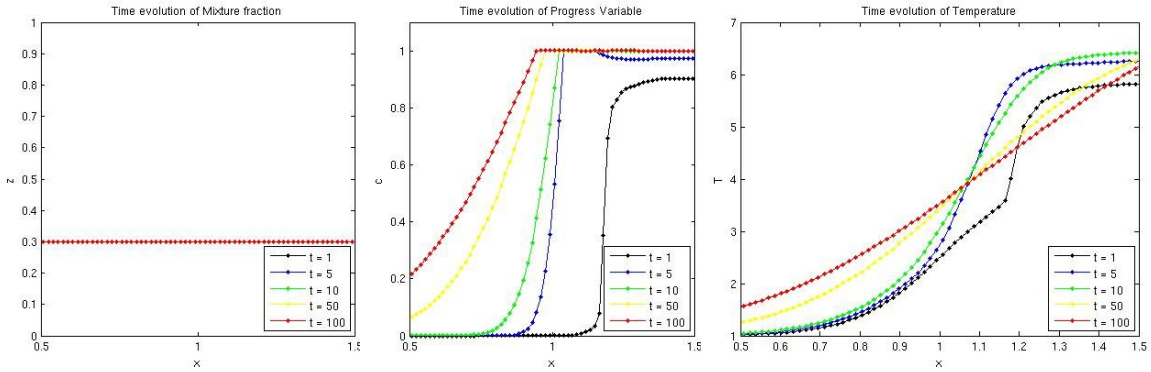

Figure A.4: Evolution of z, c and T for $z = 0.3$ and $T = [1, 4]$

Finally, the third case shown in figure A.6 has a mixture fraction varying from 1 to 0 and temperature from 1 to 4 for the left and right boundaries respectively. This mimics the shear layer interface of a cold fuel jet that autoignites due to the

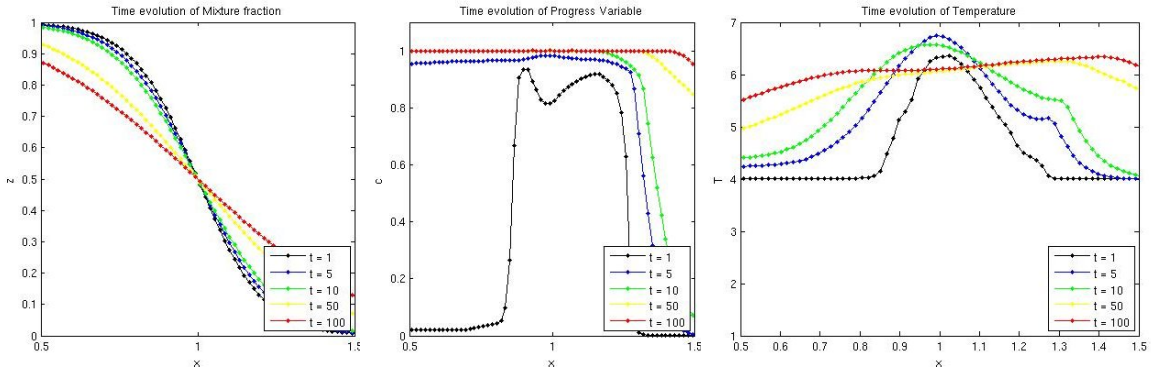

Figure A.5: Evolution of z, c and T for $z = [1, 0]$ and $T = 4$

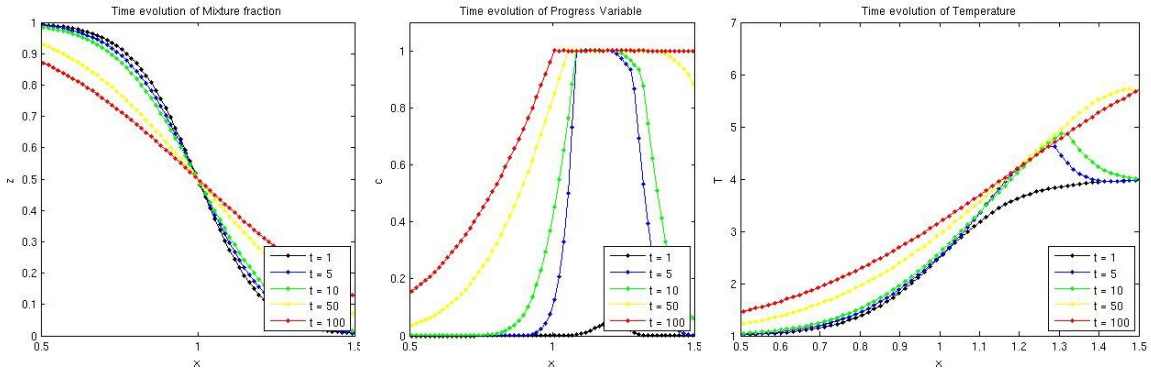

Figure A.6: Evolution of z, c and T for $z = [1, 0]$ and $T = [1, 4]$

hot coflowing oxidizer. Autoignition in this case occurs at a very lean mixture fraction (most reactive mixture fraction) and spreads into rich and lean mixtures.

As mentioned above, the UFPV model requires a new tabulation to simulate this diffusion flame each time the boundary conditions on the temperature or mixture-fraction change. In the case of a turbulent non-premixed flame, if there are any well-mixed pockets of fuel and oxidizer upstream of the flame, the UFPV model will not be representative of the combustion in these premixed pockets. Instead, by tabulating source terms as a function of temperature, mixture-fraction and progress-variable, we are able to simulate all these flames with a unique library

that is generated just once.

A.4.3 Parameters for the Tabulation

The tabulation used for the previous simulations were generated using initial conditions for the homogeneous reactor derived from a frozen mixing line of a jet's fuel and oxidizer stream properties. Along the mixing line, the temperature of the mixture can be parametrized as a function of the mixture fraction. Hence the tabulation contains only two independent parameters, mixture fraction and progress variable. The assumption that the entire flow field's combustion can be represented by two initial parameters can be violated by mixing since temperature is not a conserved scalar under reacting conditions. Further, thermal diffusion and scalar diffusion occur at different rates and the frozen mixing line is not an accurate representation of all initial conditions that need to be represented in the tabulation. Generating a tabulation with independent mixture fraction and temperature fields can vastly improve the results obtained. We will refer to this modification as the three parameter (3p) tabulation and the original as the two parameter (2p) tabulation.

Deflagration and Diffusion flames

A deflagration and diffusion flame and shown in figure A.7 simulated with the 3p tabulation. The initial conditions for the simulation are shown in red, followed by the transients in green, black and the final time instant in blue lines. We can clearly see the deflagration (premixed flame) stabilize from the transient and propagate in space, demonstrating a constant premixed flame speed. The autoigniting diffusion flame shows the ignition at lean hot conditions and thickening in space.

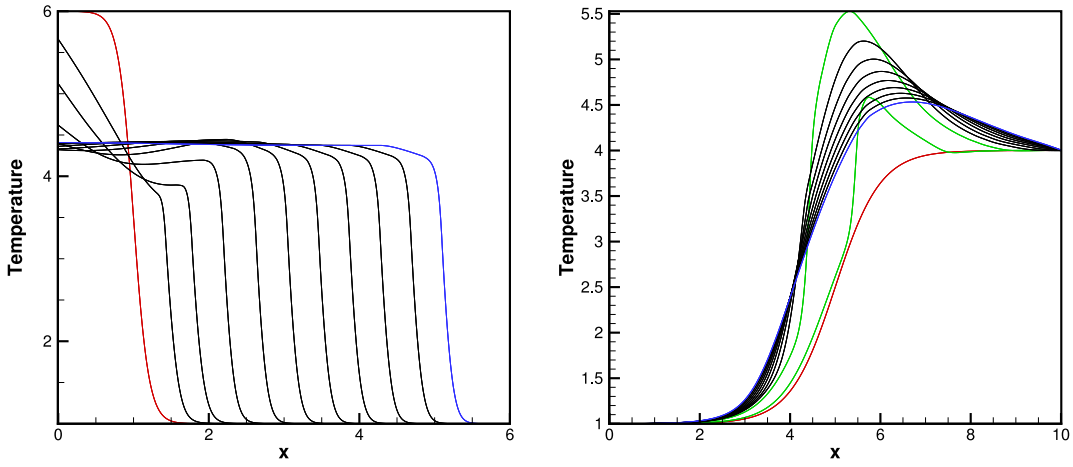

Figure A.7: (a) A deflagration and (b) a diffusion flame simulated using the model

Comparison with DNS for a diffusion flame

We compare the results obtained from the 2p and 3p tabulations with a direct simulation of a diffusion flame and results are shown in figure A.8. The comparison shows that during the ignition phase both tabulations are similar in slightly underestimating the flame temperature. However, post-ignition, the thickening of the diffusion flame is better captured by the three parameter tabulation while the two parameter tabulation has begun extinguishing. The 3p tabulation still underpredicts the flame temperature from the direct simulation but is a vast improvement over the 2p tabulation.

A.5 Summary

A combustion model using a tabulation for source terms along with two scalar equations for mixture-fraction and progress-variable is proposed and tested. The

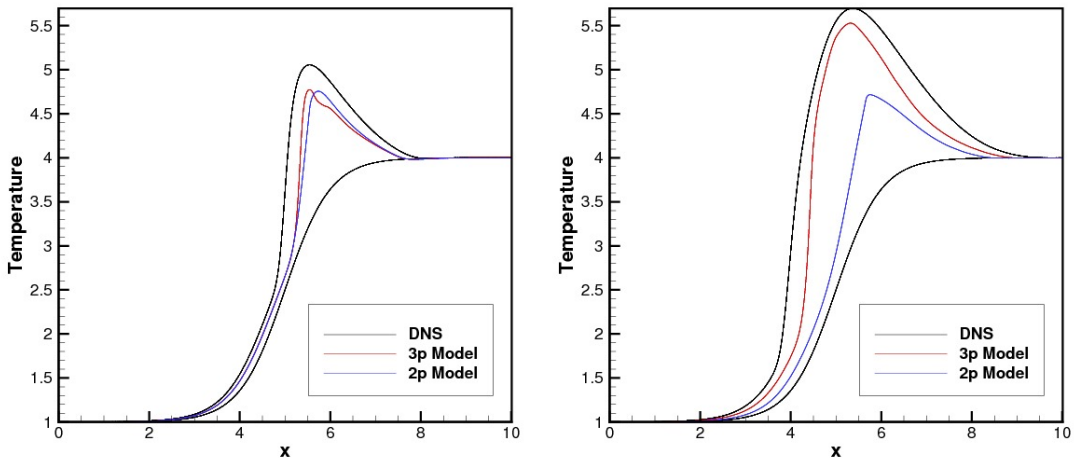

Figure A.8: Comparison of a diffusion flame solution between two tabulations of the model and a direct simulation at two time instants

model is able to capture combustion phenomena such as ignition, extinction, premixed deflagrations and diffusion flames using a single tabulation. This property of the model is compelling for most real applications which experience multiple combustion regimes simultaneously. The simulations performed with the combustion model show reasonable agreement with direct simulations especially with the three parameter model for the tabulation. The temperature discrepancy in the model results shows that there is room for further refinements in the tabulation. Carefully examining the initial conditions used for the tabulation may aid in such an improvement. The proposed combustion model is unique in its ability to represent multiple combustion regimes and is worth further exploration.